EXPERIMENTS ON MIXING AND COMBUSTION WITH LOW HEAT RELEASE IN A TURBULENT SHEAR FLOW

Thesis by

Mark Godfrey Mungal

In Partial Fulfillment

of the Requirements for the Degree of

Doctor of Philosophy

California Institute of Technology

Pasadena, California

1983

(Submitted November 19, 1982)

Dedicated to my parents,

Basdeo and Sonia Mungal.

ACKNOWLEDGEMENTS

This project is by no means a one man show. The design and construction of the facility spanned several years and required the effort of many individuals. B. J. Cantwell and G. L. Brown began the early design and construction of the facility and laid down the initial groundwork. This phase was then continued and completed under the supervision of G. L. Brown. The experimental phase of the work was completed under the supervision of P. E. Dimotakis, and with considerable assistance from J. E. Broadwell. I would like to thank those with whom I have worked during the course of the project: B. J. Cantwell for much initial help, G. L. Brown for superb guidance during the construction phase, H. W. Liepmann for sensible advice, P. E. Dimotakis for much help during the experimental phase and J. E. Broadwell for many enlightening dicussions. Many months of technical assistance were provided by Earl Dahl and are most appreciated. The competent assistance of J. C. Hermanson and C. E. Frieler was essential to the successful running of the experiment and is gratefully acknowledged.

I am also grateful for the assistance of a host of other people: Clifford Moran and D. L. Bond of the Propulsion Systems Section at JPL, Jack E. Trost, Jon R. Auguston, Jeanette A. Betts and Ken T. Yano of the Applied Technology Division of TRW, Peter Saeta for his summer work, Jerry Landry and Kent Potter of the 10 Foot Tunnel, Clarence B. Hemphill for his electrical work, D. B. Lang for his electronics expertise, Betty Wood for her draftsmanship, Harry Hamaguchi for his photographic work, and the construction services of the Central Engineering Services and the Aeronautics Machine Shop. The financial assistance of the California Institute of Technology is gratefully acknowledged. This research was sponsored by AFOSR Contract Nos. F44620-76-C-0046 and F49620-79-C-0159.

I would also like to thank my friends, family and parents for their support, especially my wife Patricia for her patience and our daughter Sonia for many happy moments. Last, but not least, I would like to thank the Good Lord for having given me the strength to complete this work.

ABSTRACT

A new blowdown facility to study mixing and combustion in a turbulent shear layer has been built. The system is capable of 100 m/s for three seconds in a 5 x 20 cm exit area on the high speed side, and 50 m/s in a 10 x 20 cm exit area on the low speed side. Dilute concentrations of hydrogen and fluorine, carried in an inert gas, react when both fluid streams meet at the tip of a splitter plate. The reaction is spontaneous, rapid, and highly exothermic. The resulting temperature field has been studied using a rake of eight fast response thermometers placed across the width of the layer. Runs have been performed for low heat release over a wide range of equivalence (concentration) ratios, at a Reynolds number of 30,800 based on velocity difference and vorticity thickness. The heat release is sufficiently low so that the overall properties of the mixing layer are not significantly changed from the cold case.

The results show the presence of large, hot structures within the flow together with cool, irrotational tongues of freestream fluid that penetrate deep into the layer. Thus, it is possible for the entire width of the layer to be quite hot, owing to the passage of a large structure, or for the layer to be quite cool, owing to the presence of the cool fluid tongues. The mean temperature results from a duty cycle whereby a given point in the flow sees alternating hot and cool fluid which averages into the local mean. The mean temperature profiles do not achieve the adiabatic flame temperature at any location across the layer, with the maximum mean temperature, depending upon the equivalence ratio, varying from 54% to 67% of the adiabatic flame temperature. The location of the maximum mean temperature shifts by about 25% of the visual thickness of the layer for a change of equivalence ratio by a factor of 64. The amount of product

formed in the layer is compared to earlier measurements in water, and, it is found that at a speed ratio of 0.40, there exists 20 to 25% more product in gaseous flows, implying that molecular diffusion, or in nondimensional form the Schmidt number, plays a role in mixing at large Reynolds number. The present results compare favorably with the recent theoretical model of Broadwell and Breidenthal for mixing and chemical reaction in a turbulent shear layer. With this model it is possible to bring the results for gases and liquids into quantitative agreement.

TABLE OF CONTENTS

LIST OF FIGURES

LIST OF SYMBOLS

Symbol	Description
A	reactant
B	reactant
c	concentration of high speed fluid, Equation D.1
c_s	stoichiometric concentration, Equation D.5
c_{10}, $c_{H.S.}$	high speed freestream molar reactant concentration
c_{20}, $c_{L.S.}$	low speed freestream molar reactant concentration
C_p	molar specific heat at constant pressure of carrier gas
D	molecular diffusion coefficient
E	entrainment ratio
f/o	fuel to oxidizer ratio, Equation 3.1.c
G	gain of circuit, Equation 2.3
h_0	$\bar{T}max/Tflm$, Equation 3.17
I	constant current through cold wire probe, Equation 2.3
k	chemical reaction rate constant, Appendix B
L	length of cold wire
Le	Lewis number, κ/D, § 3.1
P	product
P	equivalent product thickness, Equation 3.14
P_1	equivalent product thickness, $c_{H.S.} = constant$, Equation 3.15.a
P_2	equivalent product thickness, $c_{L.S.} = constant$, Equation 3.15.b
p	test section static pressure

p_t	stagnation pressure
ΔQ	heat release per mole of reactant, Equation 1.2
r	velocity ratio, U_2/U_1
R	gas constant of carrier gas, Equation 2.1
R	probe hot resistance, Equation 2.3
R_0	probe cold resistance, Equation 2.3
Re	large structure Reynolds number, $\Delta U\,\delta/\nu$
s	density ratio, ρ_2/ρ_1
Sc	Schmidt number, ν/D
t	time
T	instantaneous temperature rise
$\overline{T}$	mean temperature rise
T_B	Broadwell mixing parameter, $Sc/\mathrm{Re}^{\frac{1}{2}}$, Equation 3.11
T_b	wire temperature at supports, Appendix C
T_g	gas temperature, Appendix C
T_w	wire temperature, Appendix C
$Tflm$	adiabatic flame temperature, § 1.2
$Thmg$	homogeneous temperature of Broadwell-Breidenthal theory, § 3.1
$Tmax$	maximum instantaneous temperature for time trace
$\overline{T}max$	maximum mean temperature for temperature profile
U	velocity component in streamwise direction
ΔU	$U_1 - U_2$
ΔV	probe voltage, Equation 2.3
x	streamwise coordinate, Figure 1
x_0	virtual origin of flow, Figure 1
y	orthogonal coordinate, Figure 1
y^*	position of dividing streamline, Equation 3.4
z	spanwise coordinate

α	temperature coefficient of resistance, Equation 2.3
α	Konrad parameter, E / φ, § 3.7
δ	shear layer vorticity thickness, Equation 3.6
δ_{vis}	shear layer visual thickness, Equations 3.5, 3.8
δ_f	flame thickness, Appendix B
δ_1	shear layer thickness, $\overline{T}$ = 1% of $\overline{T}max$
ε	strain rate, Appendix B
ε_δ	large scale strain rate, Appendix B
ε_λ	small scale strain rate, Appendix B
η	heat transfer parameter, Appendix C
κ	thermal diffusivity coefficient
λ	small scale, § 3.1
λ_0	Kolmogorov scale, § 3.1
ν	kinematic viscosity
φ	equivalence ratio, c_{20} / c_{10}, Equation 3.1.b
τ	characteristic time
τ_δ	time to cascade to Kolmogorov scale, Equation 3.9
τ_λ	time to diffuse across scale λ, Equation 3.10
θ	boundary layer momentum thickness
ξ_φ	normalized equivalence ratio, $\varphi / (1 + \varphi)$, § 3.7
high	highest instantaneous temperature recorded
low	lowest instantaneous temperature recorded
pdf, PDF	probability density function, $p(c)$
H.S.	high speed
L.S.	low speed
[ ]	molar concentration, Appendix D

$( )_s$ stoichiometric conditions

$( )_T$ average in mixed region

$( )_1$ freestream conditions on side 1

$( )_2$ freestream conditions on side 2

$( )_0$ freestream conditions

Chapter 1

Introduction

1.1. Background

Turbulent shear layers have been studied for several decades. The discovery of large scale structures in turbulent shear flows has resulted in considerable experimental and theoretical activity in this area. More recently, mixing has been the quantity that has received most attention because of its importance to several technological areas. This research should be viewed as a continuation of previous work performed here at CALTECH, such as Brown & Roshko [1974], Konrad [1976], Dimotakis & Brown [1976], Breidenthal [1978], and Bernal [1981] and also the similar experiment of Wallace [1981] in Australia. The major difference between this investigation and the earlier work is that the mixing layer is undergoing combustion with simultaneous heat release. It is anticipated that the large structure dynamics which have already been shown to be quite important in the cold cases will continue to be important when combustion takes place (Ganji & Sawyer [1980], Wallace [1981]).

The experimental facility has been designed to be capable (ultimately) of maximum flame temperatures of 1000°K above ambient, but the present work is performed for low heat release with maximum flame temperatures of 165°K above ambient. The present aim is to study mixing and product formation in the limit of low heat release to achieve a more basic understanding of these phenomena, and to provide part of the data base to which the higher heat release cases will be compared. It should also be noted that this research is similar in both concept and design to that of Brown & Wallace (see Wallace[1981]), the major differences being that the present experiment is capable

of higher heat release, higher Reynolds number and faster chemistry.

The turbulent mixing layer is perhaps the simplest turbulent flow. Both the initial vorticity and geometry are two dimensional and the initial vorticity is essentially of one sign. The flow is well documented, and occurs in many practical combustor designs. By adding to both streams, low concentrations of various reactants which release heat spontaneously and rapidly, it is possible to study the amount of product formed due to molecular mixing (see Figure 1). Problems of flameholders and igniters are eliminated, and it now becomes possible to investigate, in an incremental fashion, the effects of heat release upon the flow itself. It is also possible to investigate the effects of equivalence (concentration) ratio in a straightforward manner. The present experiment uses hydrogen and fluorine (together with trace amounts of nitric oxide, for proper ignition) to achieve this end - the reaction is simple, fast, highly exothermic and well documented. Thus the present experiment should be viewed as an attempt to address the more general and difficult problem of turbulent mixing and combustion in a manner in which the fluid mechanics and chemical kinetics remain tractable. In fact, it is thought that if any problem in turbulent combustion holds the hope to analytic or computational success, then surely this must be it!

The aims of the research program were as follows:

1. Design and construction of a facility capable of high Reynolds number and high heat release.
2. Increase understanding of the turbulent mixing process.
3. Systematic investigation of the effects of heat release upon the mixing layer and also the effect of Reynolds number.
4. Comparison with predictions based on Konrad's measurements.
5. Comparison with theoretical models, in particular, with the recent Broadwell-Breidenthal model for mixing and chemical reaction in a

turbulent shear layer.

The Broadwell-Breidenthal [1981] model is an idealization, in which the turbulent mixing layer is decomposed into three types of fluid: (1) unmixed pure reactants, (2) a homogeneous mixture at the entrainment ratio, and (3) in strained laminar diffusion layers (flame sheets) between the free stream fluids. It will be discussed further in Chapter 3.

1.2. Chemical Reaction Method

Breidenthal [1978] has pointed out that the amount of molecular scale mixing in a turbulent shear layer between two streams can be measured in at least two ways: the passive scalar technique consists of introducing a passive scalar contaminant into one stream and measuring the local concentration as a function of time. If the probe sampling volume is small compared to the smallest concentration scales then it is possible to measure the true local concentration and to infer the molecular scale mixing at that point (Toor [1962]). If however the sampling volume is too large, concentration fluctuations will be smoothed out and the inferred amount of mixing or product will be overestimated.

The second technique is to use a method whereby the mixing at the molecular level is displayed macroscopically in some conveniently measurable fashion. Such a process is a second order chemical reaction of the type $A + B \rightarrow P$. Thus if dilute reactant A is added to one stream and dilute reactant B is added to the other and, if they react rapidly and irreversibly to form reaction product P, then the amount of product formed is just equal to the amount of molecular mixing at the reaction equivalence ratio. In contrast to the passive technique, a finite sampling volume does not inherently overestimate the amount of mixing. For a simple, irreversible reaction the total amount of mixed fluid within the sampling volume is just equal to the amount of product there, independent of the size of the sampling volume.

Konrad [1976] used the passive scalar technique together with a concentration probe (see Brown & Rebollo [1972]) for measuring purposes. Breidenthal [1978] was able to approximate the irreversible reaction with a reversible one using Phenolphthalein and sodium hydroxide, i.e.,

$$\text{Phenolphthalein} + 2(OH)^- \rightarrow \text{red product}, \tag{1.1}$$

which was probed by measuring the attenuation of a beam of green light. In the present investigation, the irreversible reaction is approximated to high accuracy by the reaction

$$H_2 + F_2 \rightarrow 2HF, \ \Delta Q = -130 \ \frac{\text{kcal}}{\text{mole}} \tag{1.2}$$

This reaction is sufficiently energetic that 1% F_2 in nitrogen and 1% H_2 in nitrogen will produce an adiabatic flame temperature of 93°K above ambient (for this work, the adiabatic flame temperature is defined as the temperature obtained if both reactants burn to completion, adiabatically, at constant pressure). Thus, dilute concentrations produce significant temperature rises. As shown in Appendix B, the reaction actually consists of two second order chain reactions with chemical times that are fast compared to the fluid mechanical time scales.

It should also be stated that while a long term goal of the present studies is to investigate the effect of heat release on the mixing layer, the present results are entirely at the low heat release end of the spectrum where the heat itself serves to label the molecularly mixed fluid, so that in this work, heat release and product formation are analogous. It is believed that the present results will assist in the understanding of turbulent mixing and also serve as a data base to which the higher heat release cases can be compared.

The simple physical ideas contained in the Broadwell-Breidenthal model, together with their implications, guided the experiments which were performed at a fixed Reynolds number, with low heat release, for a wide range of equivalence ratios. Chapter 2 gives a description of the experimental facility and measuring techniques, while Chapter 3 presents the results of the investigation together with some comparisons to other work.

Chapter 2

Experimental Facility and Instrumentation

A considerable amount of effort was directed at the unique problems encountered in designing a system for use with hydrogen and fluorine. The design was started originally by B. J. Cantwell, and completed under the guidance of G. L. Brown. Running and instrumentation problems were addressed with the help of P. E. Dimotakis and J. E. Broadwell. Since fluorine is a highly reactive element, proper handling at all times is of prime importance. Schmidt [1967] and Bond et al. [1979] provided much information on which the design was based. In addition, important specific advice was provided by the Propulsion Systems Section of the Jet Propulsion Laboratory, California Institute of Technology and by the Applied Technology Division of TRW. It must be mentioned that great care was also required in the safe handling of hydrogen owing to its wide flammability range. Appendix A contains a discussion of some important considerations in handling both gases.

2.1. Flow Apparatus and Exhaust Treatment

The apparatus is a blowdown facility similar to that designed by Wallace [1981] in Australia, but with Reynolds number capability similar to that of the Brown-Roshko [1974] gas facility. The latter can operate at eight atmospheres pressure but the present design operates at one atmosphere pressure and this necessitated a larger test section. The design goals were 100 m/s for 3 seconds on the high speed side in a 5 x 20 cm. (2 x 8 inch) exit area. The low speed exit area is 10 x 20 cm. (4 x 8 inch) with a maximum speed of 50 m/s.

Figure 2 shows the layout of the laboratory. Because of the toxicity and reactivity of fluorine (Appendix A), on the one hand, and the flammability of

hydrogen on the other, safety was a prime concern and some safety features are evident in this figure.

The facility operates in the following way: By using a fixed mixing volume and a partial pressure technique, a given concentration of fluorine in some inert gas (e.g. nitrogen, helium) is loaded into the left reactant vessel (20 cubic feet volume). This charge is contained in a gas tight FEP teflon bag within the vessel. The teflon bag was made by heat sealing sheets of .005 inch teflon on a commercial heat sealer (Accuseal, model B3). The outside of the bag is connected, via a butterfly valve and a check valve, to a very large surge tank (450 cubic feet volume) containing pressurized nitrogen. The surge tank provides the flow that is neccessary to collapse the teflon bag and thus displace the reactant charge during a run, while still maintaining an essentially constant upstream stagnation pressure. A similar technique is used to load a charge of hydrogen in its inert carrier gas into the right reactant vessel. Figure 3 shows the reactant vessels. The lower line (visible at the bottom of the photograph) links both reactant tanks to the surge tank. The flow is started and stopped by means of fast-acting globe valves ($\sim$500 msec) which serve as the main opening valves. Each gas stream is metered by a sonic valve which consists basically of a moveable stainless steel piston that controls the open area of eight 1/8 inch wide slots at which the flow remained choked during the course of a run. Micrometer positioners were used to accurately position the piston and thus control the flow rate through each valve. Each stream then enters a noise suppression section which consists of a length of eight inch diameter stainless steel pipe containing aluminum perforated plate and a one inch thick section of densely packed aluminum screen.

The contraction section is $27\frac{1}{2}$ inches high by $46\frac{1}{2}$ inches long by $9\frac{1}{2}$ inches wide and, for compatibility with fluorine, is made of TFE teflon bonded to

aluminum with a special viton adhesive (Products Research and Chemical, PR-1710, PR-1730. This adhesive was suggested by Clifford Moran of JPL). Curved and straight stainless steel perforated plates were used to expand the flow from circular to rectangular sections at the contraction box entrance. In addition, four screens were used (40 and 80 mesh monel, 50% open area) together with a 6:1 contraction ratio on the high speed side and a 3:1 ratio on the low speed side. The high speed contraction length to inlet height ratio of 2.5 meets the flow non-separation criterion suggested by Chmielewski [1974]. The splitter tip was removable and was made of 303 stainless steel, with an included angle of 3.78 degrees. These features produced good flow quality with a turbulence level measured at 95 m/s to be less than 1/3% rms, and about twice this value at 22 m/s, the speed at which the present runs were conducted. Figure 4 shows a side view of the facility, while Figure 5 shows a sketch of the contractions.

The test section was made almost entirely of 316 stainless steel and pyrex glass (Corning, borosilicate 7740). Both were chosen for thermal, chemical and mechanical toughness. The vertical sidewalls, through which the flow was viewed, consisted of 1 inch thick pyrex sheet together with an inner, replaceable 1/8 inch sheet of pyrex. This inner sheet becomes etched in time by hydrogen fluoride and sodium hydroxide and is replaced periodically, while the outer sheet supports the load when the system is evacuated. The adjustable sidewalls were either 3/16 inch pyrex or nickel plated aluminum. The top and bottom sides of the test section box consisted of 1 inch plexiglass and were buffered from fluorine by a slow nitrogen purge during the run sequence. The overall length of the section is 30 inches. The useable length, in which the flow can be studied, is 20 inches. Figure 6 shows a closeup of the test section with the splitter tip visible on the left.

Once the flow exits the test section, the hot, toxic exhaust gases enters a 20 inch diameter stainless steel duct (visible on the right of Figure 4) and are washed on the fly, by a high pressure spray system (600 psi, 12 gpm). A similar technique has been used by Thayer et al. [1978] on work involving a pulsed HF laser. The water droplets contain 10% sodium hydroxide and enter via a set of 49 stainless steel atomizing nozzles (Spraying Systems Co., type 7N) which were chosen to produce mean diameters of approximately 100 microns. The droplets both cool the flow (by vaporizing) and partially neutralize the hydrogen fluoride and unburnt fluorine. The exhaust gases then travel vertically through another duct and are collected in two, large FEP teflon catch bags (.005 inch thick, heat sealed sheets). Each bag is 14 x 14 foot for a combined total capacity of about 400 cubic feet. Figure 7 shows the vertical duct and teflon catch bags. The collected gases are then backpurged, using an air ejector pump, through a sodium hydroxide scrubber system to remove remaining toxins, and the inert carrier gas and unburned hydrogen are discharged to the atmosphere. Finally, the spent liquid from the sodium hydroxide spray system, which contained sodium fluoride is treated with calcium oxide (soda lime) to precipitate out any calcium fluoride. The remaining liquid is neutralized to a pH of seven and then discharged.

In general it is possible to achieve good repeatability from run to run. The most serious problem stems from the fact that the lab is neither heated nor cooled, and contains a natural ventilation system (for hydrogen safety). Consequently, the lab temperature remains close to the outside ambient temperature with a few hours time delay. As a result the hydrogen and fluorine, which are stored outside the building (in the interest of safety), and the inert gases used for the loading sequence (using the partial pressure technique) can be at different temperatures. If no corrections are made, it is estimated that a 3% difference in absolute concentration is possible on similar runs made on cool

(15°C) or hot (25°C) days, while the concentration ratio is probably unaffected. In any event this error was considered acceptable for the purposes of this work.

2.2. Instrumentation

There were four main types of data recorded during the course of a run. These were: pressure gradient, photographs, velocity and temperature. Each of these will be described below.

2.2.1. *Pressure Gradient.* The static pressure was sensed at two points (x = 3, 12 inch) on the low speed sidewall and applied differentially across a fluorine resistant barocell pressure sensor head (Datametrics, model 573). The signal was recorded on a strip chart during the run. In general, the pressure gradient changes with each different value of heat release, but, it was relatively straightforward after a few early runs to estimate and set the proper wall divergence, required for zero pressure gradient, before a given run. Based on the measured pressure gradient the low speed velocity is estimated to be constant along the length of the test section to within 1.5% for all runs.

2.2.2. *Photography.* During a run, with the room darkened, a weak yellowish orange glow (chemiluminescent overtone emission of excited *HF*) could be seen with the naked eye. This was photographed for some runs (6 second time exposure) to provide information on the virtual origin, visual thickness, etc. Additionally, a simple shadowgraph system was employed which consisted of a spark source (4 μsec duration) placed 88 inches from the centerline of the test section. The image was recorded on a sheet of 8 x 10 inch film held against the sidewall glass. The shadowgraph could show no information in the constant density (nitrogen-nitrogen)case but revealed the usual large scale structure in the variable density (helium-nitrogen) case.

2.2.3. *Velocity.* (Most of the work in this section was performed by J.C. Hermanson) The mean velocity was measured by a rake of 15 pitot probes located across the layer. The probes were made from a length of .065 inch diameter stainless steel tubing and were spaced 0.30 inch apart. The total pressures were balanced against the test section static pressure in a miniature, critically damped manometer bank containing a fluorocarbon oil as the sensing liquid (Hooker Chemical, FS-5). The settling time was approximately 3 seconds. The manometer bank consisted of 17 glass tubes (3 mm. ID) connected at their base to a common reservoir. The two outer tubes were connected to the test section static port (located at the x = 17 inch station on the low speed sidewall) while the 15 inner tubes were connected to the pitot rake. Thus, any difference in height of the sensing liquid between the outer and inner tubes represents the mean dynamic head. The bank was photographed during a run by a motor driven camera. Several frames were subsequently digitized on the HP9874 digitizer, averaged, and converted to a velocity profile. This system is compatible with fluorine and hydrogen, is relatively inexpensive and requires neither traversing mechanisms nor scanivalves.

The average velocity in the streamwise direction was obtained from the pitot tubes and manometer bank using the measured local average temperature and the relation

$$U = \left[2R\overline{T}(p_t - p)/p\right]^{\frac{1}{2}} \tag{2.1}$$

where

p = test section static pressure

p_t = stagnation pressure

$\overline{T}$ = local mean temperature

R = gas constant of carrier gas

A non-linear least squares curve fit using a functional representation of the type

$$U(y) = b_5 \tanh(b_1 + b_2 y + b_3 y^2 + b_4 y^3) + b_6 \qquad (2.2)$$

was applied to the data to produce the mean velocity profile.

2.2.4. *Temperature.* The temperature was measured by a rake of eight cold wires operated in the constant current mode, i.e. as resistance thermometers. The spacing between probes was 0.38 inch. A temperature rake has been used previously by Fiedler [1974] and Rajagopalan & Antonia [1981] to investigate a mixing layer in which one stream was slightly heated with respect to the other. Figure 8 shows a sketch of a typical wire (these wires were designed and built by C. E. Frieler). It consists of a length of 2.5μ diameter platinum / 10% rhodium wire that is welded to a pair of .014 inch diameter inconel prongs which are contained within a dual bore ceramic tube (Al_2O_3) and 316 stainless steel outer protective sheath. It was decided to use platinum/rhodium instead of platinum because of its greater strength (factor of 2 in Young's modulus), while accepting the penalty of reduced sensitivity (factor of 2 in temperature coefficient of resistance). The wires were welded to the prongs, rather than soldered, in order to reduce possible thermoelectric effects at the junctions. Each wire has an overall length of approximately 1.5mm, for an aspect ratio of 600 and a typical resistance of 50 ohms. The simple circuit of Figure 9 provided 0.4mA constant current through each wire and was used to measure changes in wire resistance due to heating by the flow. It is estimated that under natural convection (a worst case) the electrical heating causes a temperature rise of less than 0.2°K, which is negligible compared to the temperatures of interest in the flow, and hence the probe sensitivity is velocity independent. This is not to be confused with the response time of the probe, which by King's Law remains velocity dependent as discussed in Appendix C. If we neglect the slight overheat and the slight

non-linearities in the temperature coefficient of resistance it can be shown from Figure 9 that the voltage change, ΔV, for a given temperature rise, ΔT, is given by

$$\Delta V/\Delta T = I\alpha R_0(1+G) \tag{2.3}$$

where

I = current through wire

α = temperature coefficient of resistance

R_0 = probe cold resistance

G = gain of circuit

and it is assumed that, in the operating range of the experiments, the wire resistance, R, is a linear function of temperature, $R = R_0(1 + \alpha \Delta T)$ (see Sandborn [1972]). Thus the voltage increases linearly with temperature rise.

The signal from each wire was amplified by a variable gain stage and filtered by a third-order low-pass Butterworth filter with the knee (3 db down point) set at 8 kHz. This arrangement produced satisfactory signals with an rms noise of the order of the overheat of the wire (approx. 0.2°K). It should also be mentioned that there was no observable difference in behavior when the wires were tested with a higher overheat current of 0.8 mA, thus confirming the velocity independence of each probe. Figure 10 shows the temperature rake. The velocity rake is swung away and is visible to the right of the figure. Normally both rakes are separated by 1.5 inches in the spanwise (z) direction, so that the measurements of temperature and velocity occur at slightly different locations.

Finally, a traversing mechanism was constructed which was capable of moving, via a stepper motor and linear ball screw, a probe in steps of .0025 inch at a maximum step rate of 1 kHz. Such a technique has been used by Wallace [1981]

to measure the mean temperature and mean velocity profiles in a chemically reacting mixing layer containing nitric oxide and ozone as reactants. However, this traversing system was not used in favor of the static, multi-point measurements described above.

2.3. Data Acquisition

All data acquisition was accomplished using the portable HYDRA-1 system that was designed and assembled at GALCIT by P. E. Dimotakis and D. B. Lang. It is based on a Digital Equipment Corporation LSI 11/23 CPU with 256 kB of memory together with a Data Translation DT2782 12 bit, 8 channel A/D converter which is capable of a maximum data rate of 125 kHz. The system is also equipped with an Andromeda DAC-11 D/A converter, line printer, and HP9872 plotter.

The cold wires were sampled at 10 kHz each for a total data rate of 80 kHz. A total of 98304 points, or 12288 per probe, were recorded during a run and stored in extended memory. The data were transferred, at the end of a run, to either hard or floppy disc for further processing. The latter consisted of first removing the offset voltage for each probe and then applying to each of the eight probes, a single calibration constant (see Appendix C) which converted the recorded voltages into temperature rise in degrees Kelvin.

The computer was also used to control the running sequence. Once the apparatus had been brought to the firing point manually, control was passed to the computer which started the run by first activating the motor driven camera (for the pitot probe manometer bank), opening the low speed and high speed valves in that order, then waiting a preset time interval for the flow to reach steady state, before recording the temperature measurements. The system was then shut down in reverse order after a preset run time had elapsed. At this

point control returned to manual operation. This arrangement of both manual and computerized operation has worked satisfactorily for the present set of runs. The system is also capable of being expanded up to the point where the entire running sequence can be executed by computer.

Chapter 3

Results and Discussion

Two basic flows were investigated in the limit of low heat release: the constant density (nitrogen-nitrogen) layer and the variable density (helium-nitrogen) layer. Low heat release is considered to be the regime in which the overall properties of the shear layer are not significantly changed from the cold case. Wallace [1981] has identified low heat release flows to be those for which the maximum mean temperature rise is less than 100°K above ambient, which corresponds to an average density decrease of about 15% within the transverse extent of the layer. In the work reported here most of the effort was directed at the constant density layer at a Reynolds number of 30,800 based on the velocity difference, ΔU, and vorticity thickness, δ. (The Reynolds number based on ΔU and downstream distance, x, is 400,000.) The equivalence ratio, φ, was varied by a factor of 64, and is defined here as the ratio of the low speed freestream molar concentration, c_{LS}, to the high speed freestream molar concentration, c_{HS}, divided by the low speed to high speed molar stoichiometric ratio, i.e.,

$$\varphi \equiv \frac{(c_{LS}/c_{HS})}{(c_{LS}/c_{HS})_s} \tag{3.1.a}$$

$$= \frac{c_{LS}}{c_{HS}} \tag{3.1.b}$$

since the hydrogen-fluorine molar stoichiometric ratio is unity. Physically, the equivalence ratio, as defined in Equation (3.1.a), is the volume of high speed fluid required to react completely with unit volume of low speed fluid. This

definition is more useful here than the conventional definition of the equivalence ratio (e.g. in diffusion flame theory), where it is defined as the fuel to oxidizer ratio divided by the fuel to oxidizer stoichiometric ratio, i.e.,

$$\varphi = \frac{(f/o)}{(f/o)_s} \tag{3.1.c}$$

where f, o are normally taken to be mass fractions. If f, o are taken to be molar fractions, then Equation (3.1.c) becomes similar to Equation (3.1.a). As will be seen, for the purposes of this work there is no need to distinguish which species is fuel and which is oxidizer: the more important concern is the ratio of low speed to high speed concentrations, and this importance is reflected in the definition of φ. Several runs were also performed to demonstrate that chemical kinetic rates and ignition had little influence on the results. Finally, a few runs were performed for the variable density helium-nitrogen layer.

It is useful to define the speed ratio, r,

$$r \equiv \frac{U_2}{U_1} \tag{3.2}$$

and the density ratio, s,

$$s \equiv \frac{\rho_2}{\rho_1} \tag{3.3}$$

All measurements were taken at the x = 18 inch station. The runs performed were:

a. constant density case (nitrogen, nitrogen)

U_1 = 22 m/s, U_2 = 8.8 m/s, r = 0.40, s = 1.0

φ = 1/8, 1/4, 1/2, 1, 2, 4, 8

φ = 1, demonstrate insensitivity to chemical kinetic rates

φ = 1, demonstrate true ignition by insensitivity to nitric oxide

b. variable density case (helium, nitrogen)

U_1 = 23 m/s, U_2 = 8.8 m/s, r = 0.38, s = 7.0

φ = 1/2, 1, 2

In each case the measurements consisted of the set described in the previous chapter. Sample time traces of the measured temperature are shown below for each run together with the mean temperature profile (in this work all temperatures, unless explicitly stated, refer to temperature *rises* above ambient and are measured in degrees Kelvin). The results are compared to earlier measurements and also to the recent Broadwell-Breidenthal model. All temperature profiles have been corrected to the position of the dividing streamline for an equivalence ratio of unity. The position of the dividing streamline, y^*, is found by combining the continuity and momentum equations to derive the following equation,

$$\int_{y^*}^{\infty} \frac{\overline{\rho U}}{\rho_1 U_1}\left(\frac{\overline{U}}{U_1}-1\right)dy = \int_{-\infty}^{y^*} \frac{\overline{\rho U}}{\rho_1 U_1}\left(\frac{U_2}{U_1}-\frac{\overline{U}}{U_1}\right)dy \qquad (3.4)$$

where $(\,)_1$ and $(\,)_2$ denote free stream conditions on sides 1, 2 respectively. In addition, it should be noted that the 1% thickness of the layer, δ_1, which is taken to be the points at which mean temperature rise is 1% of the maximum mean temperature rise, was obtained from the mean temperature profiles, and for r = 0.4, found to be in very good agreement with the Brown-Roshko [1974] formula for the constant-density visual thickness, namely:

$$\frac{\delta_{vis}}{(x-x_0)} = 0.38\left[\frac{1-r}{1+r}\right] \tag{3.5}$$

where x_0 is the virtual origin. In fact, this suggested changes in $(x-x_0)$ from 17.5 to 18.5 inches for various runs and hence a mean value of 18.0 inches was used throughout. The speed ratio, r, varied from 0.39 to 0.41 during the course of the runs and a mean value of 0.40 was used for all constant density runs.

In some plots the vorticity thickness, δ, is used for normalization, where

$$\delta = \frac{\Delta U}{\left.\frac{\partial U}{\partial y}\right|_{max}} \quad . \tag{3.6}$$

For the present low heat release cases the formula from Brown-Roshko [1974] was used, namely

$$\frac{\delta}{(x-x_0)} = .18\left[\frac{1-r}{1+r}\right] \tag{3.7}$$

Use of these formulas seems reasonable for two reasons. First, in the low heat release case there exist only small differences in the velocity profile between the hot and cold cases (see later), and second, the present measurements together with those of Wallace [1981] suggest that for the maximum mean temperature rise less than 100°K, these formulas are a good approximation.

Finally one other quantity must be reported for the present set of runs. The high speed boundary layer momentum thickness, θ_1, was computed using Thwaites' method for the contraction sketched in Figure 5. The resulting Reynolds number, $U_1\theta_1/\nu$, is estimated to be 240. Thus, at the measuring station $x/\theta_1 \approx 2800$.

For the helium-nitrogen runs, no statements can be made about the position of the dividing streamline from the pitot tube data, so direct comparison was made with Konrad. Additionally it was observed that the growth rate (δ_1 - 1% thickness) of the present variable density layer appears to reduced by about 25-30% when compared to the visual growth rates of Brown-Roshko [1974] for the helium-nitrogen layer, namely,

$$\frac{\delta_{vis}}{(x-x_0)} = 0.51 \left[\frac{1-r}{1+r}\right] \tag{3.8}$$

There are four possible reasons for this: first, the present layer is horizontal with helium on top and nitrogen below, so that gravitational effects could influence the growth rate. This appears unlikely since the Froude number suggests that the gravitational forces are negligible when compared to the inertial forces. Second, the effect of the heat release may possibly contribute to the apparent thinning of the layer, but was not observed by Wallace for the low heat release, variable density case. A third possibility (suggested by A. Roshko) is that the 1% thickness, δ_1, for the variable density case, simply underestimates the visual thickness as measured by Brown-Roshko. The fourth possibility is that the layer may have suffered from being too close to the sidewall. This is not a problem in the constant density case but is more likely to occur in the variable density case owing to the larger entrainment ratio. It is presently thought that this fourth possibility may be the cause of the discrepancy. In any event, the results for this case are presented below and are interpreted in terms of the Broadwell-Breidenthal theory.

3.1. Broadwell-Breidenthal Theory

This section contains a brief description of the recent Broadwell-Breidenthal [1981] model for mixing and chemical reaction in a turbulent shear layer. It is discused at this point since some of the results to be presented are interpreted in terms of the model. In this description the term *entrainment* refers to the process by which irrotational fluid is brought into the layer while the term *mixing* refers to mixing at the molecular level.

This simple model visualizes the mixing process as a sequence of events beginning with the entrainment of pure, irrotational fluid into the layer. The entrained lump of fluid is subsequently broken down into smaller and smaller scales, with rapid increase in the interfacial area, until the smallest scale, the Kolmogorov microscale, λ_0, is reached. This entrainment process occurs in a time, τ_δ,

$$\tau_\delta \approx \frac{\delta}{\Delta U} \tag{3.9}$$

where δ is the width of the layer and ΔU is the velocity difference across the layer. Once this occurs, molecular diffusion quickly annihilates any concentration gradients that may exist and homogenizes the mixed fluid. This is so because the time, τ_λ, to diffuse across the (small) scale λ, is given by

$$\tau_\lambda \approx \frac{\lambda^2}{D} \tag{3.10.a}$$

$$\approx \tau_\delta \, Sc \, \mathrm{Re}^{-\frac{1}{2}} \ll \tau_\delta, \quad \text{for} \quad \mathrm{Re} \gg 1 \tag{3.10.b}$$

where D is the species diffusion coefficient, $Sc = \nu/D$ is the Schmidt number and $\mathrm{Re} = \Delta U \delta/\nu$ is the local Reynolds number.

This leads to an idealization in the model, in which the turbulent mixing layer is decomposed into three types of fluid: (1) unmixed pure reactants, (2) a homogeneous mixture at the entrainment ratio, and (3) in strained laminar diffusion layers (flame sheets) between the free stream fluids. For a combusting flow with fast chemistry, there are known temperatures associated with each of these three fluid types. The pure unmixed fluid is at ambient temperature, since no reaction has yet occurred. The homogeneous mixture attains a homogeneous (uniform) temperature determined by the free stream reactant concentrations and the entrainment ratio, while the flame sheets have a temperature distribution determined by diffusion flame theory. In the model, the mean temperature results from a combination of these three different temperatures.

(The Lewis number, $Le = \kappa / D$, where κ is the thermal diffusivity and D the mass diffusion coefficient represents the ratio at which heat and mass diffuse. For equal molecular diffusivities of all species and unity Lewis number, the maximum temperature achieved in the flame sheet will be the adiabatic flame temperature (§ 1.2), while, for unequal diffusivities and non-unity Lewis number the flame sheet achieves a maximum temperature which is different from the adiabatic flame temperature (Liñan [1974]). For the purposes of this work this distinction has been ignored.)

The model cannot predict *a priori* the relative amount of product that resides in the homogeneous and flame sheet regions. It does, however, predict that for liquids (e.g. water, $Sc = 600$) the product in the flame sheet is negligible and that therefore the total amount of product will be independent of Reynolds number for equivalence ratios larger than the entrainment ratio. The same description of the homogeneous region applies to gases ($Sc = 0.7$) but the flame sheet contribution is not negligible and the amount of product there is a function of Reynolds number and equivalence ratio. Thus for similar Reynolds

numbers, the amount of product generated in a gas is larger than that generated in a liquid by the amount contained in the flame sheets.

Breidenthal [1978] has noted that there are two limiting cases for the mixing process, according to the early version of this model, as first proposed by Broadwell (see Witte et al. [1974]). In the first case, if diffusion is slow enough then diffusion across the microscale will be the bottleneck in the sequence of events which culminates in molecular mixing. In this case the mixing is then small scale diffusion limited. In the second case, if diffusion is rapid enough, entrainment becomes the slow step in the mixing process. The mixing is then entrainment limited. Since τ_δ represents the entrainment time, and τ_λ represents the time to diffuse across the microscale, then the ratio of these two time scales determines whether the mixing is small scale diffusion limited or large scale entrainment limited. The ratio is

$$T_B \equiv \frac{\tau_\lambda}{\tau_\delta} \approx \frac{Sc}{\mathrm{Re}^{\frac{1}{2}}} \tag{3.11}$$

Thus for $T_B >> 1$, the mixing is limited by the small scale diffusion, while for $T_B << 1$ the mixing is large scale entrainment limited. For the present high Reynolds number, the flow is therefore entrainment limited, and, is not to be confused with the (laminar) flame sheets themselves within the flow, in which the reactions are diffusion limited because of fast chemistry (see Burke & Schumann [1928]).

3.2. Constant Density Results

The results described in this section are for the constant density nitrogen-nitrogen layer. Results for the variable density helium-nitrogen layer are discussed in § 3.8.

3.2.1. *Temperature.* The runs described in this section were performed using fluorine (1 or 2%) on the high speed side and hydrogen (1, 2, 4, 8%) on the low speed side. It was thus possible to achieve equivalence ratios, φ, of 1/2, 1, 2, 4, 8 by suitable choices of concentrations.

Figures 11a,b show the temperature within the layer as recorded by the eight cold wires as a function of time, for an equivalence ratio of unity (1% F_2 on H.S. side, 1% H_2 on L.S. side). Each such plot displays 512 points per probe for a total of 4096 points with the high speed stream on top and the low speed stream on the bottom. The horizontal axis corresponds to 51.2 msec since each probe was being sampled at 10 kHz. Note that (real) time increases from left to right so that the leading edge of a hot region occurs to the ***left*** of the trailing edge of the same region, i.e. the flow can be viewed as being from right to left. The vertical scaling is such that the distance between horizontal axes is equal to the highest temperature recorded by any probe during this time. This quantity is labelled *Tmax* at the top, right of the plot. Thus for this figure *Tmax* = 79°K while the adiabatic flame temperature, labelled *Tflm*, is 93°K. The actual physical distance between the outermost probes is 2.66 inch, and at the mean convection speed of 15.4 m/s, the horizontal axis would correspond to roughly 27 inches. Thus the horizontal axis is greatly compressed relative to the vertical axis. In addition, the top of the plot shows the run number, the block number and the equivalence ratio, φ. A complete run consists of 24 such records (blocks) and corresponds to a real time interval of 1.2 seconds. Two consecutive records are shown for each run. It should be noted that all such temperature vs time traces are shown for raw, uncompensated data.

Three important features are apparent from this plot: First, there are large, hot structures that extend across the width of the layer. Second, the structures are separated by tongues of cool fluid that extend deep into the layer from

either side. Third, there exists little temperature gradient within the structures from one edge of the layer to the other, i.e. the structures appear to be well mixed at about the same temperature. The first two observations are consistent with the photographs of Brown & Roshko [1974], Konrad [1976], Dimotakis & Brown [1976], Breidenthal [1978], and Wallace [1981]. The third observation is consistent with the measurements of Konrad who demonstrated that the mean concentration in the mixed fluid is roughly constant across the layer. Thus, in this sense, the results are not new. What is new here is the fact that the present measurements can now be used to attach quantitative values to the extent of molecular mixing within the layer in general and the large structure in particular.

On averaging the results for the entire run, one obtains the mean temperature profile which is shown, normalized by the adiabatic flame temperature, *Tflm*, in Figure 11c. Also listed on the right of the figure are the maximum mean temperature, $\overline{T}max$, the homogeneous temperature (as discussed in the Broadwell-Breidenthal theory), *Thmg*, the area under the curve, *Tarea*, and the 1% thickness of the layer, δ_1, which is taken to be the points at which the mean temperature rise is 1% of maximum. The smooth curve is an exponential fit of the type

$$\overline{T}(y) = \exp\left(c_0 + c_1 y + c_2 y^2 + c_3 y^3 + c_4 y^4\right) \qquad (3.12)$$

where $\overline{T}$ is the local mean temperature rise, with the point $y = 0$ corresponding to the position of the dividing streamline.

This fit is considered to be reasonable as it allows for a gaussian profile with added degrees of freedom. Note that the fit determines the value of the maximum mean temperature, $\overline{T}max$. On identical runs, a small shift of the temperature rake would sometimes place a particular probe at the point where the

maximum occurred, and the agreement between measured and implied maxima was generally excellent. Thus the curve fit is considered completely satisfactory for the present set of results.

An important observation is that the adiabatic flame temperature is not achieved, on average, at any location. In fact, $\overline{Tmax}/Tflm = 0.66$ for $\varphi = 1$. This result is in direct contrast to conventional gradient diffusion - eddy diffusivity predictions requiring stoichiometric conditions at some point in the layer, with the resulting adiabatic flame temperature. A similar result has been reported earlier by Wallace [1981]. With the large structure point of view, it is seen that the mean temperature profile results from a duty cycle i.e. a given probe spends varying lengths of time, dependent upon its position within the layer, in alternate regions of hot and cool fluid which over long time averages into the local mean. This results in a low mean temperature towards the outer edges of the layer and a higher mean temperature within.

The figure also shows in the upper curve, the maximum instantaneous temperature (*highs*) recorded by each probe, while the lower curve shows the minimum instantaneous temperature (*lows*) recorded by each of the eight probes. Both the *highs* and the *lows* have been normalized by $Tflm$ in this plot. It is apparent that the layer can be quite hot across its entire width as shown by the upper curve, or quite cool as is shown by the lower curve. As discussed in Appendix C, the instantaneous values can be in error by as much as 10-15% owing to conduction error from the tips. Thus the *highs* must be higher, while the *lows* must certainly be lower. The *highs* are associated with the passage of the large, hot structures, while the *lows* result from the cool irrotational tongues that enter the layer from either side (see for example the photographs of Brown & Roshko [1974] or Konrad [1976]). In fact, it might be argued that the *lows* should probably all be zero and this can be used as a way to estimate

the conduction error of the cold wire probes (see later).

It is thought that, at some time, each probe should encounter a flame element that is burning at the adiabatic flame temperature (neglecting Lewis number effects), but, as discussed in Appendix B, the flame thickness is so small as to be well beyond the resolution capabilities of the probes. Thus the *highs* as discussed here refer more to a local maximum within a small region whose size is dictated by the physical dimensions and response of the probe. The reason for the asymmetry in the *lows*, despite the symmetrical mean profile, is thought to be due to the fact that the conduction error is reduced on the high speed side by increased convection, or stated another way, the parameter, ηL, in Appendix C, is larger on the high speed side than on the low speed side. These statements, of course, concern only excursions from the mean. The estimates of the mean temperature, as discussed in Appendix C, do not suffer from these deficiencies.

It should be noted from the temperature-time traces, Figures 11a,b, that the response time of the wires can be estimated simply by looking at the exponential curves apparent in the traces as the wire emerges from the sharp interface separating a hot region from a cool one and vice versa. In Appendix C it is shown that the wire is essentially a first order system with characteristic time, τ, where τ is a function of velocity. By examining the decay or rise curves it is estimated that the response time ranges from 300 μsec on the high speed side to 500 μsec on the low speed side. It should be noted that this time response is a consequence of the small mass of the wires and is achieved without compensation of any sort.

Figures 12a,b show consecutive time traces for a run of $\varphi = 2$ (1% F_2 on H.S. side, 2% H_2 on L.S. side). The adiabatic flame temperature for this flow is 124°K. The results are similar to the case $\varphi = 1$, but we now begin to observe that the highest temperature has shifted slightly towards the lean reactant side. There

is still clear evidence of the large, hot structures and the cool tongues of fluid that enter the layer from either side. The mean temperature profile for this run is shown in Figure 12c. Note that the profile has shifted towards the lean reactant, but, as will be discussed later, the shift has little, if anything, to do with gradient diffusion. The *high* and *low* curves show that the layer can be quite hot, or quite cool across its width as discussed earlier.

For $\varphi = 4$ (1% F_2 on H.S. side, 4% H_2 on L.S. side, adiabatic flame temperature 149°K) the time traces are shown in Figure 13a,b and Figure 13c is the mean temperature profile. The main features discussed above are still present and the maximum mean temperature continues to shift toward the lean reactant. It does appear from the time traces and the *highs* that the rich side of the layer is cooler than the lean side - some of this is thought to be fluid mechanical while the remainder is thought to be due to the conduction error of the probe (this point will be discussed later).

Finally, Figures 14a,b,c show the time traces and mean profile for the case $\varphi = 8$ (1% F_2 on H.S. side, 8% H_2 on L.S. side, adiabatic flame temperature 165°K). This was the highest equivalence ratio investigated in the present work. We observe from the time traces that the rich side of the layer is relatively cool compared to the lean side (despite conduction error) i.e. there exists some gradient within the core of the structure itself in the normal, y, direction, and, as will be discussed later, in the streamwise, x, direction as well. The mean profile shows increased skewness towards the lean reactant, but as before, the adiabatic flame temperature is never achieved on average, at any location across the layer. The reason for this will become clearer later when the results are interpreted in terms of the Broadwell-Breidenthal model.

All of the runs described above were repeated, but with the fluorine (1 or 2%) now carried on the low speed side and hydrogen (1, 2, 4, 8%) carried on the high

speed side. This produced equivalence ratios of 1/8, 1/4, 1/2, 1, 2. The time traces and mean temperature profiles are shown in Figures 15 to 18. Figure 15c is essentially a repeat of Figure 11c but with the reactants interchanged. The repeatability is good, and will be discussed further later (§ 3.5). All major features described previously are apparent in these runs, namely, large hot structures, cool fluid tongues, well mixed cores, and, hot or cool temperatures across the entire width of the layer. The highest temperatures are still biased towards the lean reactant, which is now the low speed side (lowest trace on all time traces). The maximum mean temperature normalized by the adiabatic flame temperature is observed to decrease as φ decreases below unity.

All mean temperature profiles, normalized by the adiabatic flame temperature, are summarized in Figure 19, where the results for φ = 1/8, 1/4, 1/2, 1, 2, 4, 8 are shown. This plot represents a change in φ by a factor of 64. It is clear that the shifts in the profiles are mild, with the maximum mean temperature shifting by about 25% of the visual width of the layer, for this range of φ, in agreement with the earlier results of Wallace [1981]. As mentioned earlier, these shifts are thought to be associated with the slight gradient in concentration of the mixed fluid that exists from one edge of the layer to the other, a point that will be discussed later. The maximum mean temperature normalized by the flame temperature varies from .54 to .67 for a range of φ of 1/8 to 8, but is not monotonic with φ. In fact, the maximum occurs somewhere between φ = 1 and φ = 2. The same results, plotted in temperature rise in °K are shown in Figure 20. The maximum mean temperature rises were deliberately kept below 100°K in order to operate in the low heat release regime. Finally, Figure 21a shows the temperature profiles that result if the high speed concentration remains fixed at 1% and the low speed concentration is varied from 1/8% to 8%, while Figure 21b shows the temperature profiles that result if the low speed concentration remains fixed at 1% and the high speed

concentration is varied from 1/8% to 8%.

A most interesting result is that for any pair of runs of equivalence ratio φ_0 and $1/\varphi_0$, the mean temperature profiles are different (Figures 19, 20). One might expect that for such a pair of runs, which use the same compositions (and hence have the same adiabatic flame temperature) but carried on different sides of the layer, that one might obtain similar mean temperature profiles. This is clearly not the case as shown in Figures 19, 20. Here we see that, with the exception of $\varphi = 1$, which repeats to within the experimental error, the results for $\varphi = 1/2, 2$, $\varphi = 1/4, 4$, and $\varphi = 1/8, 8$ are different even though the pairs of runs involve the same chemical compositions and have the identical adiabatic flame temperature. This phenomenon will be discussed later.

3.2.2. *Velocity.* Figure 22 shows some typical velocity profiles for both cold and hot cases. The technique used to measure the velocity profile has been discussed in Chapter 2. The plot shows the comparison for three runs: (1) cold, Run 32, (2) hot, $\varphi = 1$, Run 34 and (3) hot, $\varphi = 1/8$, Run 37. It can be seen that there are only slight differences among the three cases, suggesting that for these low heat release runs, the combustion is not significantly altering the velocity profile.

3.2.3. *Photography.* Figure 23 shows two time-exposed photographs (6 second exposure) of the light emitted during a run. The faint yellow-orange glow results from overtone radiative emission of the excited, HF^*, molecules. An important consideration is the fact that HF^* is preferentially collisionally deactivated by HF molecules, so that while the production rate of HF^* is constant with x, there is more collisional deactivation as one proceeds downstream and hence the light intensity decreases with x. The flow is from left to right with the high speed fluid on top. The top photograph shows the result for $\varphi = 1$ (Run 34)

with 1% H_2 on the H.S. side and 1% F_2 on the L.S. side. The light intensity is symmetric as might be expected from the symmetric mean profile (Figure 15c). In the initial portion of the photograph where the image is well defined, the linear growth rate is readily apparent. The bottom photograph shows the result for $\varphi = 1/8$ (Run 37) with 8% H_2 on the H.S. side and 1% F_2 on the L.S. side. The emitted light is now no longer symmetric but is biased towards the lean reactant, similar to the mean temperature profile (Figure 18c). This lack of symmetry is thought to be associated with the slight gradient in mean mixed concentration that occurs across the layer.

3.3. Comparisons

That the measured temperatures for runs of equivalence ratio φ_0 and $1/\varphi_0$ are different, is explained by the Broadwell-Breidenthal theory in a quite straightforward manner. Figure 24 shows a sketch of a typical case for $\varphi = 1/4, 4$. Use is made of the fact that the entrainment ratio for this particular speed ratio (see Konrad [1976]) is 1.30. Since the entrainment ratio, E, is defined as the ratio of the volume of high speed fluid to the volume of low speed fluid that enters the layer, the layer contains 30% more fluid from the high speed side than from the low speed side. The sketch shows two typical runs using identical free stream compositions but carried on different sides of the layer. In case 1 the reactants are 1% F_2 on the low speed side and 4% H_2 on the high speed side for an equivalence ratio, $\varphi = 1/4$. In case 2 the same reactants are now interchanged with 4% H_2 on the low speed side and 1% F_2 on the high speed side for an equivalence ratio, $\varphi = 4$. Since the compositions are identical, the adiabatic flame temperature is the same for both cases. Thus, in case 1, the lean reactant comes from the low speed side and is 1 part fluorine which burns out in the large structure to dictate the homogeneous temperature. In case 2, the lean reactant now comes from the high speed side and is now 1.3 parts

fluorine, and it burns out to determine the *higher* homogeneous temperature. In both cases however, the flame sheet contribution remains the same since the amount of product (or contribution to the mean temperature profile) is unaffected by changing the sides on which the chemicals reside. Thus, case 2 will be hotter than case 1 implying a different temperature profile for the same adiabatic flame temperature.

This result can also be derived directly from the earlier measurements of Konrad [1976]. As shown in Appendix D, one can generate the mean temperature at each point across the layer for which the concentration probability density function, $p(c)$, is known, where c is the concentration of high speed fluid. Thus, for the cases $\varphi = 4, 1/4$ the function $T(c)$ will be as shown in Figure 25. If we now compute the integral

$$\overline{T} = \int_0^1 T(c)p(c)dc \tag{3.13}$$

on each of the Konrad *pdf's*, then the results are different owing to the fact that these *pdf's* have a peak at $E/(1+E)$ where E is the entrainment ratio. In fact, the integrals would only be the same if the *pdf's* were completely symmetric about $c = 0.5$ (it is fair to say that while the Konrad *pdf's* have been published since 1976, it is only with the advent of the simple Broadwell-Breidenthal model that this implication of the Konrad results was recognized). This computation has been performed for the cases $\varphi = 8, 1, 1/8$ and compared to the experimentally measured result. The comparisons, Figures 26a,b,c, show that the concentration probe used by Konrad overpredicted the amount of product by about 40-60%, depending upon φ. As mentioned in Chapter 1, Konrad used the passive scalar technique which generally yields an upper bound to the amount of molecular mixing. It had been thought for some time that there may have been an error due to the relatively large sampling volume of Konrad's concentration

probe when compared to the Kolmogorov scale. The present results confirm this suspicion. It is also interesting to note in this regard that the maximum mean temperature implied by Konrad is in good agreement with the experimentally obtained value, for large φ, while the agreement is poor towards the outer edges of the layer.

It is also useful to compare the present results with those of Wallace [1981]. There are several differences between the Wallace experiment and the present experiment: The chemicals used were nitric oxide and ozone with a heat release of 47.5 kcal/mole (vs 130 kcal/mole for hydrogen - fluorine), the mean temperature was recorded by traversing a fine thermocouple across the layer (vs the present static arrangement of eight cold wires) and most runs were performed for a speed ratio of 0.20. Fortunately, a constant density (nitrogen-nitrogen) run was performed at a speed ratio of 0.38 using 3% nitric oxide on the high speed side and 3% ozone on the low speed side for an equivalence ratio of unity. The Reynolds number for this run is not reported but thought to be about 8,000 to 10,000 based on velocity difference and vorticity thickness. This run can be compared to a present 1% hydrogen, 1% fluorine run since the heat released is about the same. Under these conditions, the chemical times for the nitric oxide - ozone reaction is about two orders of magnitude slower than the hydrogen - fluorine reaction. The comparison is shown in Figure 27. Apart from the differences in locating the dividing streamline the agreement is quite good with the amount of product (area under the curves) differing by about 10%. This provides an independent check on the present results.

Finally it is useful to interpret the present results in the context of the observation made by Konrad [1976] that the mean mixed concentration across the layer is nearly constant, and, the recent topological picture of the mixing layer proposed by Bernal [1981]. Figure 28 shows the average concentration of the

high speed fluid in the mixed regions, $\left[c(N_2)\right]_T$, for a constant density mixing layer as measured by Konrad using a concentration probe. The interesting feature is that this curve is nearly flat for most of the width of the layer. The Bernal picture of the vortex structure in the mixing layer is shown in Figure 29. This sketch shows the primary vortex together with the secondary streamwise vortices which also reside in the layer.

The time traces for $\varphi = 8, 1/8$ which are reproduced in Figure 30, show some gradient in the streamwise direction, as shown by the shaded areas, and it is useful to interpret this in terms of the Bernal picture. The Broadwell-Breidenthal model suggests that the primary vortex is homogenized at a single value, but, if we accept the two time scales of the problem, τ_δ and τ_λ (Equations 3.9 and 3.10), then the effect of the secondary vortices is to add and mix pure freestream fluid from the outside of the primary vortex towards the inside - this in effect causes a slight gradient in the mixed fluid whereby a given edge of the primary vortex will be biased toward the side of the layer to which it is closest, and this feature is observed in the mean mixed concentration measurement of Konrad (Figure 28). If this is correct, and if the secondary vortices actually wrap around the primary vortex as suggested by Bernal, then a similar gradient in concentration must exist in the normal (y) and streamwise (x) directions from one tongue of cool fluid to the next.

Thus, for the case $\varphi = 8$, the primary vortex will be low speed fluid rich and the leading edge of the structure (early time in the timetrace) is expected to be hotter than the trailing edge. The reverse is true for the case $\varphi = 1/8$, namely, the primary vortex will now be high speed fluid rich and the trailing edge will be hotter than the leading edge in this case. The shaded areas of Figure 30 confirm that this does indeed occur and lends support to these ideas. Similar gradients are visible in Figures 13, 17 and Figures 14, 18.

This change in the mean mixed concentration as we proceed from one edge of the layer to the other is thus thought to be responsible for the shifts in the temperature profiles with changes in equivalence ratio. The high equivalence ratio cases merely accentuates the slight gradient in the mean mixed concentration, and, coupled with the mixing intermittency for this flow (as measured by Konrad [1976]), produces a shifted temperature profile. Bernal's topological picture is thus considered to be a reasonable physical model to explain why the mean mixed concentrations, and hence temperature profiles, shift with varying equivalence ratio. As mentioned earlier these shifts are therefore viewed as having little or nothing to do with gradient diffusion and eddy diffusivity ideas.

It should also be noted that this interpretation can be applied to the results of Fiedler [1974, 1975] and Rajagopalan & Antonia [1981] who used a temperature rake to study a shear layer in which the high speed side was slightly heated, and to the measurements of Batt [1977] where the turbulent mixing of both passive and chemically reacting species in a shear layer was investigated. Fiedler finds gradients in the mean mixed concentration in both the normal and streamwise directions that are consistent with the present observations, with similar results reported by Rajagopalan & Antonia. Batt interprets his results differently but these gradients are noticeable in his published timetraces.

3.4. Compensated Highs

The mean temperature profiles together with the *highs* and *lows*, for all equivalence ratios are replotted in Figures 31a,b. In addition the *compensated highs* for the six innermost probes are shown in each plot (uppermost curve). As described in Appendix C, if one assumes that the *lows* result from the irrotational unmixed fluid, then it is possible to make an estimate of the conduction error for each probe and apply this to the *highs* to produced the *compensated highs* shown in each plot. The results show that for most cases the highest

temperature is roughly constant (to within 10%) across the width of the layer. The most instructive cases are for $\varphi = 8, 1/8$. Here it is clear that the *compensated highs* on the rich reactant side are significantly lower than those of the lean side. This fact can be used to infer, via the function $T(c)$ in Appendix D, a slight gradient in mixed concentration in the lateral (y) direction.

Thus, the implication of the *compensated highs* together with the evidence presented in Figure 30, is that the primary structure, while predominantly at a single concentration, actually varies slightly in mixed concentration in both the normal and streamwise directions.

3.5. Chemistry and Ignition

As discussed in Appendix B, the hydrogen-fluorine reaction is truly spontaneous for only a certain range of concentrations of either species. Hence it is not immediately obvious whether some of the results described above are attributable to chemical kinetic rate effects.

Figure 32 shows the results of four runs that were performed to demonstrate that chemistry and ignition did not influence the results. The discussion in Appendix B summarizes data that show that the addition of a small amount of nitric oxide to the hydrogen carrying stream can be used to ensure good ignition. Thus for all runs the product $[F_2][NO]$ was kept at $[.03\%]^2$, and it is worth remembering that the nitric oxide was always carried on the hydrogen side, which for some runs was the low speed side ($\varphi \geq 1$), while for others it was the high speed side ($\varphi \leq 1$). The four runs are:

1. 1.0% F_2 on H.S. side, 1.0% H_2 and 0.03% NO on L.S. side, Run 29.
2. 1.5% F_2 on H.S. side, 1.5% H_2 and 0.02% NO on L.S. side, Run 31.
3. 1.0% H_2 and 0.03% NO on H.S. side, 1.0% F_2 on L.S. side, Run 34.
4. 1.0% H_2 and 0.045% NO on H.S. side, 1.0% F_2 on L.S. side, Run 42, i.e. increase

nitric oxide concentration by 50%.

Cases 1, 2 test the chemical kinetic rates. Cases 1, 3 test the effects of interchanging the sides on which hydrogen and fluorine are carried, while cases 3, 4 test the sensitivity to *NO*.

The fact that the mean temperature profiles repeat each other to within a few percent, despite significant changes in chemical compositions and, of course, chemical rates, support the claims that first, chemical kinetic rate effects are not important, second, that there was sufficient nitric oxide to effect proper ignition and, third, that the amount of nitric oxide is not an important parameter in these results. There may be a threshold level at which the nitric oxide concentration is optimized, but for all runs it was thought that the value stated above was satisfactory. This is confirmed if the present results are compared, in Figure 27, to those of Wallace [1981] who used nitric oxide and ozone as his reactants, for which the ignition was truly spontaneous. The fact that the temperature profiles agree quantitatively suggest that there is no ignition problem.

3.6. The Inverse PDF

The problem of inverting the temperature measurements to obtain the probability density function is discussed in Appendix D. It has been discussed previously by Brown and Wallace in Wallace [1981]. Simply stated, it is desired to infer the *pdf* from either the mean temperature profiles or the histogram of the temperature. Konrad's *pdf* for the constant density case is shown in Figure 33.

The results of inversion using the mean temperature profiles and a delta function representation for the *pdf* is shown in Figure 34 (Direct Method, Appendix D). The delta functions that occur at $c = 0, 1$, and represent unmixed fluid, cannot be determined by this technique and are not shown. Several of the

features that are apparent in Konrad's *pdf* are also apparent with some modifications. There appears to be a dominant concentration from one edge of the layer to the next, but this value changes only slightly (by about 10%) across the layer. There is also a definite range of concentrations about this dominant value, and, there is also some evidence of U-shaped *pdf's* between the mixed fluid and the freestream fluid at the outer edges of the layer. The mean mixed concentration, $(c(H.S.))_T$, is inferred from these *pdf's*, and is simply the average value of the *pdf* minus the end delta functions (unmixed fluid). The comparison with Konrad is shown in Figure 35. The agreement is reasonable considering the very different techniques used to obtain both curves. It can be speculated that the mean mixed concentration might approach the value 0.5 towards the outer edges of the layer, as would be expected if the fluid existed predominantly as flame sheets between the high speed and low speed fluid.

The Franklin 3 solution (Appendix D) was also used to obtain a delta function representation for the *pdf* shown in Figure 36. The agreement with Figure 34 is apparent, and the basic features mentioned earlier occur also in the Franklin solution. The U-shaped regions, which are predicted by the Direct Method are not apparent in the Franklin solution and it remains unclear why such a discrepancy exists.

3.7. Comparison with Broadwell-Breidenthal Theory

The main elements of the Broadwell-Breidenthal model have been discussed earlier (§ 3.1). For comparison with the model it was necessary to convert the measured temperature profiles into some measure of product formed. The definition used here is similar to that of Konrad [1976] and Breidenthal [1978]. For a reaction A + B → P, then the product thickness, P, is defined as

$$P = \int_{-\infty}^{+\infty} \frac{c_p(y)}{c_0} dy \qquad (3.14.a)$$

i.e. the integral of the concentration of product across the layer is normalized by a selected freestream concentration, c_0. For the present case, since product is analogous to temperature rise, we make use of the measured mean temperature profile, $T(y)$, the molar heat capacity of the carrier gas, C_p, and the heat release per mole of reactant, ΔQ, to obtain

$$P = \int_{-\infty}^{+\infty} \frac{C_p\, T(y)}{c_0 \Delta Q} dy \qquad (3.14.b)$$

i.e. the temperature rise obtained by burning out the reactant, c_0, is used to normalize the integrated rise across the layer. For later plots the product thickness was made dimensionless with the vorticity thickness, δ, defined earlier, Equation (3.6).

An important distinction (which was initially overlooked) is the choice of the concentration c_0. If this is taken to be the high speed concentration c_{10} then we compute a product thickness, P_1, while if we choose the low speed concentration c_{20}, we compute a *different* product thickness, P_2. Stated explicitly, the definitions are:

$$P_1 = \int_{-\infty}^{+\infty} \frac{C_p\, T(y)}{c_{10} \Delta Q} dy \qquad (3.15.a)$$

$$P_2 = \int_{-\infty}^{+\infty} \frac{C_p\, T(y)}{c_{20} \Delta Q} dy \qquad (3.15.b)$$

It is found (see later) that for $\varphi >> 1$ the quantity P_1/δ approaches a limiting value of 0.57 while for $\varphi << 1$ the quantity P_2/δ approaches a limiting value of

0.51. In general, at the limiting values, $P_1 > P_2$ owing to the fact that the layer entrains more fluid from the high speed side than from the low speed side, with these limits corresponding physically to the amount of product formed in the layer as the lean reactant (high speed or low speed) is burned to completion.

These two limits can also be related to the *pdf* for this flow. As discussed in Appendix D, the mean temperature profile can be computed from

$$\overline{T} = \int_0^1 T(c)p(c)dc \qquad (3.16.a)$$

For $\varphi \to \infty$, $T(c) \to c$, while for $\varphi \to 0$, $T(c) \to (1-c)$ (see Figure 25). Thus the P_1, P_2 limits are related to

$$P_1 \sim \int_0^1 c\, p(c)dc \qquad (3.16.b)$$

$$P_2 \sim \int_0^1 (1-c)p(c)dc \qquad (3.16.c)$$

integrated across the layer, and as discussed earlier (§ 3.3) the results are different owing to the fact that *pdf* is asymmetric, resulting in the P_1 limit being larger than the P_2 limit.

Two product thicknesses also exist for a liquid as well as a gas. At present, however, only the quantity P_2/δ has been measured for a liquid (Breidenthal [1978]) and found to be 0.38 and so the Broadwell-Breidenthal model will be compared (later) to this case. It is known that the Breidenthal value provides a lower bound for a liquid owing to the reversibility of the Phenolphthalein reaction (Equation 1.1), but it believed that the error is small.

In general, to make a comparison with the model it was necessary to use the measured value of P_1/δ at $\varphi = \varphi_0 >> 1$ as an input to the model and then select some value for the homogeneous to flame sheet ratio at this equivalence ratio. Thus it is possible to extrapolate from $\varphi = \varphi_0$ to predict the value of P_1/δ for any other value of φ. Similarly, one can input the value of P_2/δ at $\varphi = \varphi_0 << 1$ and extrapolate to any other value of φ.

The product thickness P_1/δ has been plotted versus equivalence ratio φ in Figure 37. This corresponds to the amount of product contained in the curves of Figure 21a. The dotted line is a smooth fit to the experimentally measured values. The result of Wallace [1981] for $r = 0.38$ at $\varphi = 1$ is also shown. The corresponding liquid result has not been measured, but from the Broadwell-Breidenthal model one would expect 20% of the product to be in the flamesheet (see later) and so the model predictions using an 80% homogeneous, 20% flamesheet decomposition are also shown (solid line). The agreement has been forced at $\varphi = 8$ where $P_1/\delta = 0.57$. Recall that the model predicts that the liquid result is obtainable from the gas result by suppressing the flame sheet contribution, so this choice would predict a liquid result of $P_1/\delta = 0.46$ for $\varphi >> 1$.

The sharp corner, or kink in the theoretical curve occurs at $\varphi = E$ and results from the assumption that the fluid is homogenized at a single entrainment value $E = 1.3$. In fact, as the Konrad *pdf's*, and the present *pdf's* suggest there is actually a range of concentrations present, not a single value, and the effect of this would be to round off the sharp corner (for example a range of concentrations from $c = 0.25$ to $c = 0.75$ would correspond to a range of equivalence ratios from $\varphi = 1/3$ to $\varphi = 3$).

One might ask the question just how sensitive are the results to the ratio of homogeneous to flame sheet fluid? This is addressed in Figure 39 which shows some different comparisons of theory with experiment. First, we reverse the

ratio to 20% homogeneous, 80% flame sheet to obtain the curve labelled 20:80. The agreement is clearly not as good with the experimental results and in fact lies consistently below it. In addition the implied liquid product thickness is obtained by suppressing 80% of the gas result to obtain a liquid value of 0.11 which is well below the Breidenthal value. If we assume 100% flame sheet contribution, we obtain the curve labelled 0:100, which not only implies a liquid value of 0 but would imply the identical result for runs of similar compositions but carried on different sides. Finally an assumed 100% homogeneous contribution would give the curve labelled 100:0, which implies no difference in product for liquids and gases, and a 30% difference for runs of similar compositions but carried on different sides of the layer.

In order to remove some of the dependence on φ, the results shown in Figure 37 have been replotted in Figure 39. The horizontal axis is $\xi_\varphi = \varphi/(1+\varphi)$ while the vertical axis is $(P_1/\delta)/\xi_\varphi$. In these coordinates the ordinate lies between 0.55 and 0.75 for the range of φ investigated. This curve approaches the P_1 limit for $\xi_\varphi \to 1$ and the P_2 limit for $\xi_\varphi \to 0$.

The product thickness P_2/δ has been plotted versus inverse equivalence ratio, φ^{-1}, in Figure 40. This corresponds to the amount of product contained in the curves of Figure 21b. Since the model predicts that the liquid result is achievable from the gas result by suppressing the flame sheet contribution, it is reasonable to try a fit which consists of a 75% homogeneous, 25% flamesheet decomposition at $\varphi = 1/8$, where $P_2/\delta = 0.51$. The dotted line is a smooth fit to the experimentally measured values while the solid line is the prediction of the model with agreement forced at $\varphi = 1/8$ with a 75:25 homogeneous to flamesheet decomposition. The result of Wallace [1981] for $r = 0.38$ at $\varphi = 1$ (Figure 27) is also shown. With this choice of homogeneous to flame sheet, if we now suppress the flame sheet contribution at low φ, the quantity P_2/δ becomes

0.38 which is the same value measured by Breidenthal [1978] in water, for $\varphi << 1$. The comparison with Breidenthal and Konrad is shown in Figure 41 for a Reynolds number of 30,800. The overprediction of Konrad was demonstrated directly in Figure 26.

The 25% flame sheet choice at the P_2 limit explains why the 20% flame sheet choice was made at the P_1 limit (Figure 37). Since for $\varphi << 1$ the flame sheet contribution is 25%, then the Broadwell-Breidenthal model predicts a 20% flame sheet contribution for $\varphi >> 1$, and this value has been used at the P_1 limit.

It is interesting to note in Figure 37 that past $\varphi = 6$ the quantity P_1/δ is close to its asymptotic limit. This is in agreement with Wallace [1981], and means physically that the lean reactant has been burned out. Konrad has demonstrated that for the parameter $\alpha = E/\varphi$ approximately 0.1 then there would be little additional product formed and the present results (Figure 40) agrees somewhat with this prediction.

The result that gases and liquids produce different amounts of product is unexpected in the traditional turbulence point of view, since the mass diffusion coefficient, or the Schmidt number in nondimensional form, plays no role. The most obvious question is whether there is independent evidence to support this claim. The result was certainly suspected from the earlier work of Konrad [1976] and Breidenthal [1978] but it was not clear if the difference actually existed. There seems to be no additional direct evidence but the conclusion seems reasonable in light of the result of Wallace [1981]. In Figure 27 it was shown that the present results and the Wallace result for $\varphi = 1$ are in good agreement. If we accept the fact that P/δ increases as φ increases (a result also demonstrated by Wallace) then it can be inferred that the present conclusions are reasonable owing to the agreement between both sets of results at $\varphi = 1$. Thus, agreement at $\varphi = 1$ between the present runs and Wallace is

thought to be significant.

An alternate argument is to assume that for the limiting values of φ ($\varphi \rightarrow 0, \infty$) the mean temperature profile can be approximated by a triangle of height $h_0.Tflm$, where $0 < h_0 < 1$, and base equal to the visual width of the layer, δ_{vis} (see for example Figures 14c, 18c), then using Equation (3.11) it can be shown that

$$\frac{P}{\delta} = \frac{h_0}{2}\frac{\delta_{vis}}{\delta} \tag{3.17.a}$$

$$\approx h_0, \qquad \text{since} \quad \delta_{vis} \approx 2\delta \tag{3.17.b}$$

Note that the speed ratio, r, does not enter explicitly except through h_0 which represents the fraction of the adiabatic flame temperature that is achieved for high (or low) φ. Thus from Equation (3.17.b) $P_1/\delta \approx 0.63$ (see Figure 14c) compared to the actual measured value of 0.57 while $P_2/\delta \approx 0.54$ (see Figure 18c) compared to the actual measured value of 0.51. By this simple argument, the result for gas and liquid would be the same if, for $\varphi << 1$, the maximum mean temperature is approximately 40% of the adiabatic flame temperature. This is not observed in the present experiment, in fact the maximum mean temperature is more likely to be 50% of the adiabatic flame temperature for $\varphi << 1$. This simple calculation has been performed for Wallace [1981] at a speed ratio of 0.20 with the result $P_1/\delta \approx 0.44$. Unfortunately, the corresponding liquid result at this speed ratio is not known.

3.8. Helium Nitrogen Results

As mentioned earlier, a few runs were made for the inhomogeneous layer at a speed ratio of 0.38 consisting of hydrogen-helium on the high speed side and fluorine-nitrogen on the low speed side at equivalence ratios of 1/2, 1, 2. The time traces and mean temperature profiles are shown in Figures 42 to 44. The

adiabatic flame temperature is computed using the same technique as for the nitrogen-nitrogen case (§1.2) despite the fact that helium and nitrogen have different diffusion coefficients, in fact, the actual peak temperature in a diffusion flame have not been calculated for these runs. Note that in all time traces the maximum temperatures occur on the nitrogen side despite the fact that helium has a lower specific heat. The dramatic change in the mean profile shape when compared to the nitrogen-nitrogen layer is readily apparent, and interestingly, the expected 20% rise in temperature (owing to the lower specific heat of helium) did not occur. Wallace [1981] measured a decrease in the mean temperature for the inhomogeneous case compared to the homogeneous case but the present results do not show such a pronounced decrease. In addition, Wallace measured inflection points in the temperature profile while the present results contain no evidence of such. This discrepancy must be due to the different measuring techniques: Wallace - traversing a single thermocouple, versus, the present rake of eight cold wires. As mentioned earlier, it must be cautioned that the growth rate of the present (inhomogeneous) layer is 25-30% less than the cold case (Brown-Roshko [1974]) and this is presently thought to be a wall effect, owing to the much larger entrainment ratio (E = 3.5, see Konrad [1976]).

Figure 45 shows the mean profiles for the three cases φ = 1/2, 1, 2. It can be seen that increasing the concentration of hydrogen on the high speed side to 2% (φ = 1/2) produces little change from the 1%:1% (φ = 1) case, but that increasing the fluorine concentration on the low speed side to 2% (φ = 2) produces a quite dramatic increase in the mean temperature profile. The reasons for this are thought to be concerned with the fact that while the adiabatic flame temperature changes somewhat, the temperature of the homogeneous regions increases by a factor of 2 and this of course is thought to be the major contributor to the amount of product in the mixing layer. This statement is presumed

correct for the constant density case and is thought to be also true for the variable density case, by the Broadwell-Breidenthal model.

A comparison with the Konrad predictions as inferred from his measured *pdf's* are shown in Figure 46. The agreement is not very good, and further work is needed before firm conclusions can be made.

Chapter 4

Conclusions

A new facility has been built aimed at investigating a turbulent, combusting mixing layer at high Reynolds number. The facility uses dilute concentrations of hydrogen and fluorine, carried in inert gas, which react rapidly, spontaneously and with high exothermicity.

Experiments have been performed at a fixed Reynolds number, with low heat release, for a wide range of equivalence (concentration) ratios. The temperature field has been recorded by a set of eight fast response thermometers placed across the width of the layer. The results show that the combustion is dominated by the large scale structures that reside in the flow. Thus, it is possible for the entire width of the layer to be quite hot, owing to the passage of a large structure, or for the layer to be quite cool, owing to the presence of the cool irrotational tongues that penetrate deep into the layer. The mean temperature profile results from a duty cycle whereby a given point in the flow sees alternating hot and cool fluid which averages into the local mean. The mean temperature profile does not achieve the adiabatic flame temperature at any location, with the maximum mean temperature reaching about 54% to 67% of the adiabatic flame temperature, depending upon equivalence ratio. The shifts in the temperature profiles due to changing equivalence ratio are seen to be slight, with the maximum mean temperature shifting by about 25% of the visual thickness of the layer for a change of equivalence ratio by a factor of 64. It is suggested that the recent topological view of the mixing layer proposed by Bernal can be used to interpret these shifts. These results are in agreement with the earlier results of Wallace. The mean temperature profiles are compared to the

predictions of the Konrad *pdf's* and it is found that the concentration probe used by Konrad overpredicted the amount of product formed in the layer by about 60%.

A most interesting result is that the amount of product in the gaseous layer is found to be 20% to 25% more than in a liquid, as measured by Breidenthal. Thus the molecular diffusion coefficient, or in nondimensional form the Schmidt number, must play a role in mixing at high Reynolds number. The amount of product has been compared to the recent Broadwell-Breidenthal model with good agreement obtained for a 75% homogeneous, 25% flame sheet decomposition. With this choice, the results for a gas and a liquid can be addressed by a single theory.

Finally some runs were performed for a variable density, helium-nitrogen layer but the growth rate was found to be 25-30% less than the cold case. Further work is needed to clarify this difference.

Appendix A

Notes on Handling Fluorine and Hydrogen

A.1. Fluorine

Fluorine is the most reactive element known to man and also one of the most powerful oxidizing agents. It is highly toxic and potentially lethal with a threshold limit value of 1.0 p.p.m (Matheson Gas Data Book [1980]). Fortunately, there is a well developed technology for its use and much of it is discussed in Schmidt [1967] and Bond et al. [1979]. The problems of handling hydrogen and fluorine were addressed with the help of B. J. Cantwell and G. L. Brown.

The fluorine used in the present experiments is purchased from Air Products and Chemicals, bottled with diluent, and is 99% pure. The main contaminants are oxygen (< 0.3%), sulfur hexafluoride (< 0.1%), carbon tetrafluoride (< 800 p.p.m.), carbon dioxide (< 500 p.p.m.) and hydrogen fluoride (< 0.2%). The hydrogen fluoride is removed by a hydrogen fluoride trap (Matheson Gas Co.).

With respect to the present design the following features were incorporated:

A.1.1. *Materials.* The design uses principally monel, stainless steel (316 and 304L), aluminum, brass, and teflon. All lines are made of stainless steel and use only bellows sealed valves (NUPRO B & U series with metal tips, cleaned for oxygen service). Remote extension handles and metal barricades are used in the fluorine bottle area and at several points in the gas control panel. The metering valve sonic orifice is machined from monel 400 as this is considered to be a most critical area. The main opening valve (316 stainless steel Masoneilan 3 inch globe valve) has a metal seat as the flow goes sonic at the instant of opening. No soft materials, other than the upstream teflon bag, and the protective

teflon coating of the reactant vessels are used in the high pressure areas of the system. Noise suppression devices consist of aluminum perforated plate and many layers of aluminum mesh screen.

The contraction box consists of TFE teflon bonded to aluminum jig plate using viton adhesive. Soft materials are acceptable in this area as this part of the system operates at atmospheric pressure, with low fluorine concentration (less than 10% by volume). The perforated plates used for turbulence management are of 304 stainless steel while the screens are of monel. Brass is used in some areas of the velocity and temperature rakes. Nickel plated aluminum and pyrex glass are used in the test section. All O-rings are made of viton or teflon and are lubricated with small amounts of Krytox (Du-Pont) grease. To date, the materials have all performed well, and great care has been taken to ensure that surfaces are absolutely clean and protective fluoride films are never exposed to atmospheric moisture and contamination.

A.1.2. *Passivation and Cleanliness.* A most important aspect of successful fluorine use is proper cleaning and passivation. Stainless steel parts are first nitric acid pickled, while some more critical parts are electropolished (such as the mixing vessel and some areas of the test section). All surfaces are then cleaned with M-17 degreaser (available from J. B. Moore Corp.), acetone, and 95% alcohol (ethanol). Inspection under U.V. light is used for critical components. Since we do not have access to a clean room, some more difficult parts (such as the main opening valve) are cleaned by commercial companies (e.g. Garwood Laboratories, Inc.) who specialize in this sort of work.

All surfaces are passivated with fluorine before routine use. The procedure is similar to that of Schmidt and consists essentially of building up a protective fluoride film on a clean surface by gradual exposure to increasing concentrations of fluorine over a fixed period of time. Once the fluoride film has been

formed great care is necessary to prevent its removal by exposure to moisture. Moisture contamination can occur in two ways: either by accidentally communicating with moist atmospheric air, or by moisture which is carried in the inert gases used during the run. To minimize these possibilities, all lines are normally overpressured during shutdown and all inert gases are cleaned by use of a molecular sieve (Robbins Aviation, 13X) to remove contaminants and moisture. It should also be mentioned that all lines are first evacuated and then purged with dry inert gas before fluorine is admitted. This procedure effectively eliminates contaminants and greatly minimizes the chances of accidents.

A.1.3. *Disposal.* At the end of a run, any lines containing fluorine were vented through a specially constructed charcoal burn barrel to convert the fluorine primarily to inert carbon tetrafluoride gas (Schmidt [1967]). Other methods of fluorine disposal consist of a high pressure sodium hydroxide spray system that is used mainly to cool the hot exhaust gases (Thayer et al. [1978]), and a water showerhead that is installed at the fluorine bottle area in the event that a major fluorine leak occurs.

A.2. Hydrogen

Hydrogen is the lightest gas known. Its ability to find small leaks together with its high flammability and low ignition energy are the main difficulties encountered in its safe use. The flammability limits are 4% - 76% in air. Minute leaks can therefore present major problems when combined with an ignition source. Most of the hydrogen lines are constructed in standard fashion using copper lines and brass valves. The only exception to this occurs at the hydrogen bottle itself where stainless steel lines are used. To avoid extensive use of explosion proof components, a natural ventilation system is installed in the laboratory, together with a hydrogen detector (Sierra Monitor Corp.) placed at a strategic location. The many air changes per hour prevent the buildup of explosive

mixtures should a leak occur. An overhead explosion proof ventilator serves to backup the natural ventilation system. Runs using high concentrations of hydrogen are normally performed with the ceiling lights off. Periodic pressure checks are performed on all lines to minimize the chances of leaks occurring during a run.

A.3. Run Procedures

Finally, some notes on the running procedures: In the interest of safety all runs are conducted from written procedures and performed with at least two operators present. A run consists of a lengthy sequence of events:

1. Test section cleaning
2. Probe calibration
3. System preparation - gases and liquids ready
4. System pumpdown to scavenge oxygen and subsequent purge
5. Fluorine loading
6. Hydrogen loading
7. Wait period for upstream mixing of charges
8. Run sequence with data recording
9. Disposal of exhaust gases
10. Unloading of unused fluorine and hydrogen
11. Processing of spent sodium hydroxide
12. System cleanup and maintainance

The entire run and cleanup sequence usually lasted the major part of a day, during which time about six bottles of nitrogen (1500 standard cubic feet) were expended.

Appendix B

Chemistry and Ignition

B.1. Chemical Reactions

The chemical reaction utilized in this experiment is

$$H_2 + F_2 \rightarrow 2HF, \ \Delta Q = -130 \ \frac{\text{kcal}}{\text{mole}} \tag{B.1}$$

The actual reaction consists of a pair of second order chain reactions of differing rates and heat release. These are

$$H_2 + F \xrightarrow{k_1} HF + H, \ \Delta Q = -32 \ \frac{\text{kcal}}{\text{mole}}, k_1 = 2.6 \times 10^{12} \ T^{0.5} \exp\left(\frac{-610}{RT}\right) \tag{B.2.a}$$

$$H + F_2 \xrightarrow{k_2} HF + F, \ \Delta Q = -98 \ \frac{\text{kcal}}{\text{mole}}, k_2 = 3 \times 10^{9} \ T^{1.5} \exp\left(\frac{-1680}{RT}\right) \tag{B.2.b}$$

where k is given in cc/mole-sec, T in °K and R is the universal gas constant in cal/mole-°K. These are the so called cold and hot reactions respectively. The cold reaction which carries 25% of the total heat release is faster than the hot reaction by about an order of magnitude at 300°K ($k_1 \approx 1.6 \times 10^{13}$, $k_2 \approx 9.5 \times 10^{12}$). These values are consistent with the rate constants quoted by Cohen & Bott [1982].

There are also chain termination reactions involving three body collisions of the type

$$F + F + M \xrightarrow{k_3} F_2 + M,$$

$$H + F + M \xrightarrow{k_4} HF + M \tag{B.3}$$

$$H + H + M \xrightarrow{k_5} H_2 + M$$

where $k_3 \approx 3.6 \times 10^{14} \frac{cc}{mole\text{-}sec}$ at 300° K, with similar rates for the k_4, k_5 reactions. However, if we consider a simple rate equation of the type

$$\frac{\partial[F]}{\partial t} = -k_1[F][H_2] - k_3[F]^2[M] \tag{B.4}$$

to compare the k_3 rate to the k_1 rate, then for nitrogen at standard temperature and pressure, and assuming that $[F_2]$ is 1% of $[N_2]$ and that $[F]$ is 1% of $[F_2]$, then we find that the second term is about three orders of magnitude smaller than the first, so that at atmospheric pressure and the concentrations used in the present experiments, termination reactions are unimportant.

Finally, there are energy transfer reactions of the type

$$HF^* + M \xrightarrow{k_6} HF + M \tag{B.5}$$

which deactivate the excited HF^* and result in thermal energy. For $M = N_2, HF, H_2$ or F_2, then $k_6 \sim 10^9, 10^{12}, 10^{10}$ respectively at 300°K. Comparison of the k_6 rate with either the k_1 or k_2 rates suggest that deactivation rates are one to two orders of magnitude faster than the pumping rates thus ensuring that the chemical energy of the reaction is converted to thermal energy.

As it turned out, it was quickly determined that for the k_1, k_2 reactions to proceed satisfactorily the presence of F *atoms* (not molecules) is a crucial requirement. As Figure B.1 of the explosion limits of fluorine-hydrogen mixtures

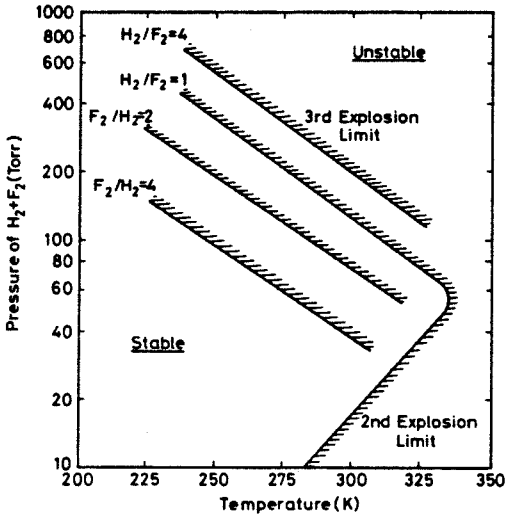

The Second and Third Explosion Limits for $F_2-H_2-O_2$ Mixtures, $[O_2]$ = 0.2%. Chen et al. [1975], © 1975 IEEE.

Figure B.1

show (Chen et al. [1975] and Gmelin Handbuch [1980]), at 1% fluorine and 1% hydrogen (total partial pressure of 15.2 torr) and room temperature (300°K) the reaction is close to the unstable region, but as we proceed to higher partial pressures the reaction moves into the stable region. Thus, it becomes crucial that there be some means to ensure the presence of F atoms. There are three possible means to achieve this:

1. optical pumping using UV light
2. addition of small amounts of chlorine to the fluorine stream
3. addition of small amounts of nitric oxide to the hydrogen stream

The first option in not realizable with the present design because of the optical power required and the fact that all of the test section materials, pyrex and plexiglass do not transmit UV light. The second option was not explored because of the complicated chemistry that would result. The third option, which was actually used, consisted of adding a small amount of NO to the hydrogen reactant vessel at the loading time, which ensured that the nitric oxide was

uniformly mixed with the hydrogen charge before a run. The nitric oxide chemistry proceeds as follows:

$$NO + F_2 \xrightarrow{k_7} NOF + F, \ \Delta Q = -18 \ \frac{\text{kcal}}{\text{mole}}, k_7 \approx 6 \times 10^{10} \frac{\text{cc}}{\text{mole}-\text{sec}} \qquad \text{(B.6)}$$

while the reverse rate is considered to be negligible (see Rapp and Johnston, [1960]). There is however an additional reaction which limits the nitric oxide concentration, namely,

$$F + NO \xrightarrow{k_8} NOF, \ \Delta Q = -57 \ \frac{\text{kcal}}{\text{mole}}, k_8 \approx 1 \times 10^{14} \frac{\text{cc}}{\text{mole}-\text{sec}} \qquad \text{(B.7)}$$

(see Cool, Stephens and Shirley, [1970]) i.e. the addition of too much NO would itself begin to deplete the available F atoms. It was determined that by keeping $[NO][F_2] = [0.03\%]^2$ that the reactions proceed satisfactorily for $[F_2] = 1$ or 2% molar. Finally, the addition of 50% more NO showed no significant changes, as was discussed in Chapter 3.

B.2. Time Scales and Flame Thickness

The following numbers are typical of the runs performed in this work.

$$U_1 = 22.0 \text{ m/s}$$

$$U_2 = 8.8 \text{ m/s}$$

$$x - x_0 = 45.7 \text{ cm} \quad (18.0 \text{ inch})$$

$$\delta = 3.5 \text{ cm} \quad \text{(vorticity thickness)}$$

$$\delta_{vis} = 7.4 \text{ cm} \quad \text{(visual thickness)}$$

$$\text{Re} = \Delta U \ \delta / \nu_{N_2} = 30{,}800$$

$$\text{Re}_x = \Delta U \ x / \nu_{N_2} = 400{,}000$$

The large scale mixing time, τ_δ, is given by

$$\tau_\delta \approx \frac{\delta}{\Delta U} = 2.7\ msec$$

and the small scale mixing time, τ_λ, which is the time to diffuse across the Kolmogorov scale, λ_0, is given by

$$\tau_\lambda \approx \frac{\lambda_0^2}{D}$$

$$\approx \tau_{mix}\, Sc\, \mathrm{Re}^{-\frac{1}{2}} = 10.6\ \mu sec$$

where D is the mass diffusion coefficient, and $Sc = \nu / D$ is the Schmidt number.

The chemical time is formed from Equation (B.2) and is given by

$$\tau_{chem} \approx 1/k[F_2]$$

$$\approx 2.4\ \mu sec$$

for 1% F_2 at 300°K and the slower rate k_2.

The Damkohler number is the ratio of the mixing to the chemical time thus,

$$\tau_\delta / \tau_{chem} \approx 1{,}125 \text{ for the large scales}$$

and

$$\tau_\lambda / \tau_{chem} \approx 4.4 \quad \text{for the small scales}$$

Note that these are computed for 1% fluorine, with the slower rate k_2, and improve with increasing concentration. In any event the chemistry is rapid compared to the relevant mixing times.

For a diffusion flame which is being strained at a constant rate ε, the flame thickness, δ_f, for large time ($t > 1/\varepsilon$) is given by (see Marble & Broadwell

[1977]),

$$\delta_f \approx \sqrt{\frac{D}{2\varepsilon}}$$

The strain rate can be written as

$$\varepsilon_\delta \approx \frac{\Delta U}{\delta} \quad \text{for the large scales}$$

$$\varepsilon_\lambda \approx \varepsilon_\delta \, \mathrm{Re}^{\frac{1}{2}} \quad \text{for the small scales}$$

Hence the flame thickness is given by

$$\delta_f \approx \delta \sqrt{\frac{1}{2\,Sc\,\mathrm{Re}}} = 170\,\mu \quad \text{for the large scales}$$

$$\delta_f \approx \delta \sqrt{\frac{1}{2\,Sc\,\mathrm{Re}^{3/2}}} = 13\,\mu \quad \text{for the small scales}$$

In the Broadwell-Breidenthal model, most of the flame sheet is taken to occur at the small scale so the second expression is probably more representative. The flame elements are considered to be laminar, strained flames with fast chemistry which result in a Burke-Schumann [1928] type thin flame geometry for which the rate of formation of product is diffusion limited.

The probe used in the present study has a resolution which is determined by its geometry and response time (Appendix C) and is approximately (1.5 mm x 2.5 μ x 0.5 cm). It is clear that the flame sheet, owing to its very small thickness, is beyond the resolution of the probe.

Appendix C

Temperature Measurement Using a Cold Wire

The problem of the response of a wire to a flow whose temperature is changing has been addressed in some detail by Scadron and Warshawsky [1952]. While most of their work is directed towards the response of bare wire thermocouples, much of the analysis applies directly to cold wires and the following discussion is condensed from their work. In addition, the text by Sandborn [1972] provides many useful insights into cold wire thermometry. Two cases will be discussed below: the elementary case neglecting conduction and radiation, and, the general case. In both cases the self heating of the wire due to ohmic resistance heating is ignored.

C.1. Elementary Case Neglecting Conduction and Radiation

The balance between the rate of accumulation of heat in an elemental length of wire and rate of convective heat transfer is expressed by a simple differential equation

$$\rho_w c_w V \frac{dT_w}{dt} = hA(T_g - T_w) \tag{C.1}$$

or

$$\tau \frac{dT_w}{dt} + T_w = T_g \tag{C.2}$$

where:

A = surface area

c_w = specific heat of wire

h = convective heat transfer coefficient

T_g = gas temperature

T_w = wire temperature

t = time

V = volume of wire element

ρ_w = wire density

τ = time constant of wire

Thus in response to a sudden "step change" in gas temperature from an initial value T_{g1} (at which time T_w will be taken equal to T_{g1}) to a new constant value T_{g2}, the wire response will be given by

$$T_w = T_{g2} + (T_{g1} - T_{g2})\, e^{-t/\tau} \qquad (C.3)$$

Several of these exponential rises or decays are readily apparent in the time traces discussed in Chapter 3.

C.2. General Case

In the presence of conductive and radiative heat transfer equation (C.1) must be replaced by a partial differential equation involving x, distance along the wire as a second independent variable. For an element of the wire, the rate of storage of heat is equal to the rates of heat transfer into the wire element due to conduction along its length, convection from the gas, and radiation, which is emitted from the wire, received from the gas and also received from the duct by transmission through the gas. This yields a differential equation

$$\tau \frac{\partial T_w}{\partial t} = \frac{1}{\eta^2} \frac{\partial^2 T_w}{\partial x^2} + T_f - T_w \qquad \text{(C.4)}$$

where τ, η and T_f are defined by:

$$\tau_1 = \frac{D^2 \rho_w c_w}{4 Nu\ k_g}$$

$$\beta_1 = \frac{\sigma D T_g^4}{Nu\ k_g}$$

$$\eta_1^2 = \frac{4 Nu\ k_g}{D^2 k_w}$$

$$\tau = \frac{\tau_1}{(1 + 4\beta_1 \varepsilon_w / T_g)}$$

$$\beta = \frac{\beta_1 \varepsilon_w}{(1 + 4\beta_1 \varepsilon_w / T_g)}$$

$$\eta^2 = \eta_1^2 (1 + 4\beta_1 \varepsilon_w / T_g)$$

$$T_f = T_g + \beta \left[(1 - \alpha_{gd}) \left(\frac{T_d}{T_g}\right)^4 - (1 - \varepsilon_g)\right]$$

where

D = wire diameter

k_g = thermal conductivity of gas

k_w = thermal conductivity of wire

Nu = Nusselt number

T_d = equivalent duct temperature

α_{gd} = effective absorptivity of gas for black body radiation at temperature T_d

ε_g = effective emissivity of gas

ε_w = emissivity of wire

σ = Stefan–Boltzmann constant

and if the thermal diffusivity of the wire, κ, is defined

$$\kappa = \frac{k_w}{\rho_w c_w}$$

then

$$\eta^2 = \frac{1}{\kappa\tau}$$

Since Nusselt number varies approximately as the square root of the Reynolds number then the response time, τ, will vary inversely with the square root of velocity, or stated another way, the wires show better frequency response on the high speed side of the layer than on the low speed side. The theoretical response time for the present wires is 130 μsec at 20 m/s, while the experimentally observed value is 330 μsec. The reduced response results from the fact that the wires are aged and "dirty" and this can degrade the response by a factor of 2 to 3 (see Paranthoen, Lecordier & Petit [1982]). No attempts were made to wash the wires before a run. In addition, the above formulas show that radiation corrections are negligible for the temperature rises achieved in the present experiments.

Two problems are of interest:

1. Steady-State Temperature Distribution in Single Wire Stretched Between Supports

The steady state problem is, from equation (C.4),

$$\frac{1}{\eta^2}\frac{d^2T_w}{dx^2} + T_f - T_w = 0$$

subject to the boundary conditions

$$T_w = T_b, \text{ at } x = 0, L$$

The solution is

$$T_w = T_f + (T_b - T_f)\Psi \tag{C.5}$$

where

$$\Psi = \frac{\sinh(\eta x) + \sinh(\eta L - \eta x)}{\sinh(\eta L)} \tag{C.6}$$

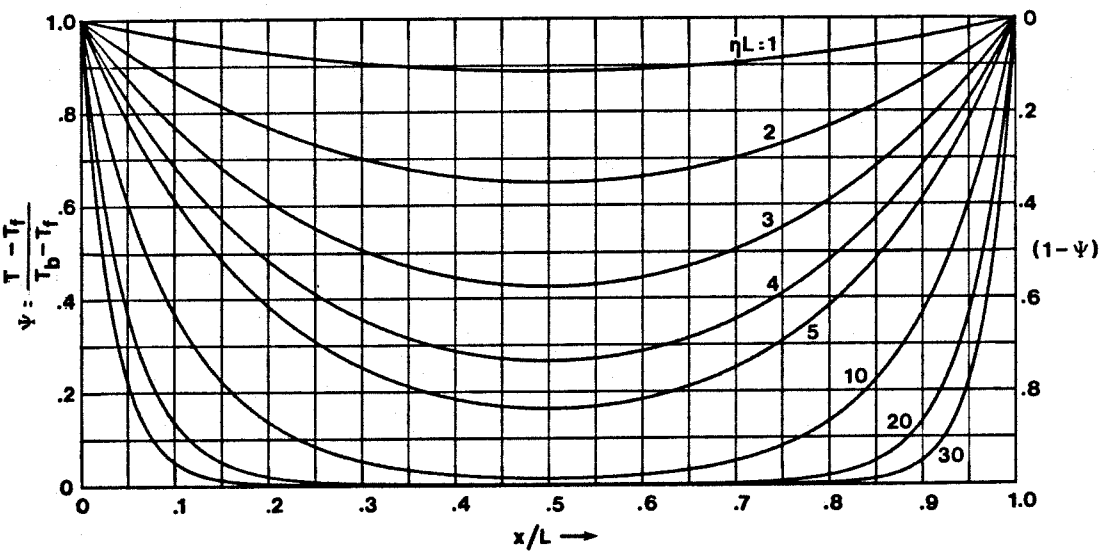

Temperature Distribution Along Simple Wire in Steady State

Figure C.1

A plot of Ψ is shown in Figure C.1. There is serious conduction error for the quantity ηL less than about 10. For the (clean) wires used in the present

experiment ηL is estimated to be about 20 when evaluated at the mean conditions, and this corresponds to approximately 10% error due to conduction.

2. Transient and Steady State Response of Single Wire to a Step Change in Gas Temperature, Wire Initially at Gas Temperature.

If the wire is initially at a temperature $[T_{f1} + (T_b - T_{f1})\Psi]$ corresponding to an actual gas temperature T_{g1} related to T_{f1} by an equation of the form (C.5), and a step change in gas temperature occurs to a value of T_{g2} yielding a corresponding effective gas temperature T_{f2} and by (C.5) an ultimate wire temperature $[T_{f2} + (T_b - T_{f2})\Psi]$, then the solution is

$$T_w = T_{f2} + (T_b - T_{f2})\Psi + (T_{f1} - T_{f2})\Phi \tag{C.7}$$

where the second term represents the steady state response, Equation (C.6), and the third term represents the transient response and is given by

$$\Phi = \frac{2}{\pi} e^{\frac{-t}{\tau}} \sum_{n=1}^{\infty} \frac{1-\cos(n\pi)}{n} \frac{1}{1+\left(\frac{n\pi}{\eta L}\right)^2} \sin\left(\frac{n\pi x}{L}\right) e^{-\frac{t}{\tau}\left(\frac{n\pi}{\eta L}\right)^2} \tag{C.8}$$

This shows that the initial time response depends upon τ and is independent of the conduction error. However, the overall time response is changed, and the present wires have effective time constants that that are within 3% of the zero conduction case (from calculations by C. E. Frieler).

In summary, in the presence of conduction error the wire will asymptote to a value that is different from the fluid value but the *initial* slope is governed by the time constant τ and this remains the same as in the zero conduction case. The wires do however have an effective time constant that is within 3% of the zero conduction case.

C.3. Calibration Procedures

The cold wire probes were calibrated before a run using a simple but quite important procedure. Two 1/2 inch diameter jets at different temperatures were directed at each probe for 4 seconds and the probe voltage recorded. Each jet contained a small thermocouple embedded in its centerline, at close to its exit plane, to provide an accurate measure of the jet temperature. This was repeated four times for the hot and cool jet and the difference in voltages provided the calibration constant that was needed to convert volts to temperature rise. The important feature of this technique is the fact that both the wire and the prong tips came to the temperature of the jet, since it is estimated that the tips equilibrate in about a second.

During a run the combusting flow performs exactly the same function as the hot jet, namely, the tips equilibrate to the mean temperature and the wire makes excursions about this value as dictated by the fluid mechanics, but, subject to the boundary condition that the ends of the wire are tied to the local mean. Hence the mean temperature does not suffer from conduction error. It is also useful to note that there is no trend in the time averaged data from one block of data to the next, thus implying that the tips had truly equilibrated.

It is also possible, using Equation (C.5) to make some estimate of the conduction error if the assumption is made that each probe must see cool, irrotational fluid that penetrates deep into the layer from either side, at some time during the run. (This is believed to be the *lows* discussed in Chapter 3). Using this estimate of Ψ, any wire temperature, T_w, can be corrected to a fluid temperature, T_f, using Equation (C.5). This correction to the *highs*, to produce the *compensated highs*, has been discussed in Chapter 3.

Appendix D

The Inverse PDF Problem

There is interest in extracting the probability density function from the present data mainly for two reasons: first, it would afford a direct comparison with Konrad's *pdf*, and second, some current work in combustion theory requires the *pdf* for a given flow (see Bilger in Libby & Williams [1980]). An indirect comparison with Konrad's *pdf*, using the inferred temperature profile, has been performed in Chapter 3.

The computation of the *pdf* from the mean temperature profiles has been discussed previously by Wallace [1981]. An alternate approach is to use the histogram of the temperature data, which is obtained from the measured time traces, to obtain the *pdf*. The solution to this problem was formulated by Professor J. N. Franklin of the Applied Mathematics Department, California Institute of Technology, and will be described below. We begin by first describing the double valuedness of the basic problem.

D.1. The Double Valuedness Problem

(This discussion proceeds along lines similar to Wallace [1981]) First consider a turbulent mixing layer with the high speed side labelled A, 1 and the low speed side labelled B, 2 (for example see Figure 1). Consider an infinitesimal sampling volume where we measure (by any possible means) the local instantaneous concentration, c,

$$c \equiv \frac{n_1}{(n_1+n_2)} \tag{D.1}$$

where

$$n_1 = \#\text{ of moles of 1 in sampling volume}$$

$$n_2 = \#\text{ of moles of 2 in sampling volume}$$

In addition, suppose that n_1 contains n_a moles of dilute reactant A and that similarly n_2 contains n_b moles of dilute reactant B. We define

$$c_{10} \equiv \frac{n_a}{n_1} \tag{D.2a}$$

$$c_{20} \equiv \frac{n_b}{n_2} \tag{D.2b}$$

to be the freestream concentrations of the H.S. and L.S. sides respectively and the equivalence ratio, φ,

$$\varphi \equiv \frac{c_{20}}{c_{10}} \tag{D.3}$$

Then, in measuring a concentration, c, implies that n_a moles of A and n_b moles of B are present in the sampling volume. For no reaction they simply coexist, but for a fast reaction (such as burning) the lean reactant will be consumed. Thus for an irreversible reaction of the type

$$A + B \rightarrow P$$

then the concentration of product, c_p, is given by

$$c_p = \begin{cases} \dfrac{n_a}{n_1+n_2} & \text{for } n_a < n_b \\ \dfrac{n_b}{n_1+n_2} & \text{for } n_b < n_a \end{cases} \tag{D.4a}$$

or

$$c_p = \begin{cases} \dfrac{n_a}{n_1}\cdot\dfrac{n_1}{n_1+n_2} = c_{10}\,c & \text{for } n_a < n_b \\ \dfrac{n_b}{n_2}\cdot\dfrac{n_2}{n_1+n_2} = c_{20}(1-c) & \text{for } n_b < n_a \end{cases} \qquad \text{(D.4b)}$$

the special case $n_a = n_b$ implies stoichiometric conditions i.e.

$$c_{10}.c_s = c_{20}.(1-c_s)$$

$$c_s = \frac{c_{20}}{c_{10}+c_{20}} = \frac{\varphi}{1+\varphi} \qquad \text{(D.5)}$$

A sketch of c_p is shown in Figure D.1

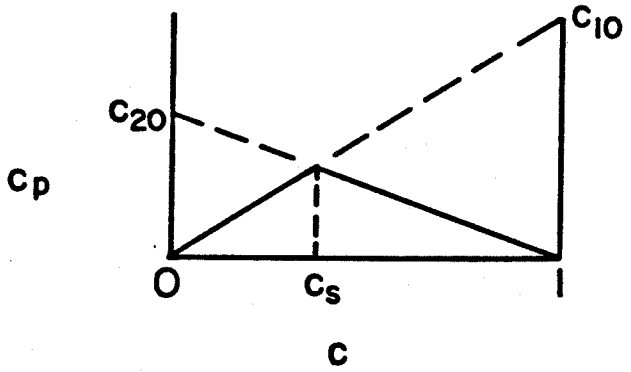

Figure D.1

By using the heat released by the reaction, ΔQ, and the molar specific heat at constant pressure of the inert carrier gas, C_p, we see that c_p varies directly with temperature to obtain

$$T(c) = \begin{cases} c_{10}.c\,.\Delta Q/C_p & \text{for } c \le \dfrac{\varphi}{1+\varphi} \\ c_{20}.(1-c).\Delta Q/C_p & \text{for } c \ge \dfrac{\varphi}{1+\varphi} \end{cases}$$

(D.6)

This is plotted in Figure D.2.

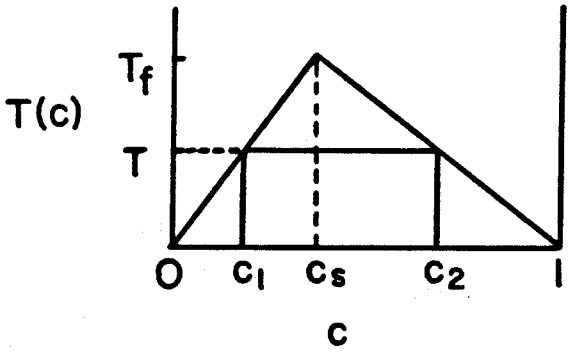

Figure D.2

In the general case where the two incident streams have different specific heats C_{p1} and C_{p2}, the specific heat of the mixture becomes a function of the concentration, and it is necessary to substitute in Equation (D.6) for C_p the expression

$$C_p(c) = C_{p2} + c(C_{p1} - C_{p2}) \tag{D.7}$$

The shape of the curve $T(c)$ leads to a double valuedness i.e. there are two possible values of c namely c_1 and c_2 (Figure D.2) that lead to the same value of T (this corresponds to a given reactant being either lean or rich). The only exception to this occurs at c_s when stoichiometry is achieved and the temperature becomes the adiabatic flame temperature, T_f.

Knowing $T(c)$ it is possible to use the probability density function $p(c)$ for the turbulent mixing layer as measured by Konrad (Figure 33) to compute the mean temperature across the layer, $\overline{T}$, since,

$$\overline{T} = \int_0^1 T(c)p(c)dc \tag{D.8}$$

This calculation was performed for each of the seven *pdf's* measured across the layer by Konrad, using a simple FORTRAN program. The result is discussed in Chapter 3. Thus the direct problem, namely, given $p(c)$ to compute $\overline{T}$ is readily solvable. The inverse problem i.e. extracting $p(c)$ from the mean temperature profiles, $\overline{T}(y)$, or from the histograms of T/T_f is a more difficult task.

D.2. Methods for Computing the PDF

D.2.1. *Direct Method.* A simple approach to finding the *pdf* consists of using Equation (D.8). One must perform several runs of differing $T(c)$, (i.e. by changing φ) and assume a delta function representation for $p(c)$ to which Equation (D.8) can be applied to solve for the magnitudes of the delta functions. This approach has been used by Wallace [1981] and in this work, with the results shown in Chapter 3. This technique has the advantage that the mean temperatures are used and these are not dependent upon the response of the particular probe that is used. The disadvantage is that the technique requires many runs at various φ for a reasonable representation of $p(c)$.

D.2.2. *Matrix Method.* A second approach is to make use of the function $T(c)$. From Figure D.3 we note that the probability that T lies in the interval $(T_1, T_1+\Delta T)$ is equal to the sum of the probability that c lies in the interval $(c_1, c_1+\Delta c_1)$ plus the probability that c lies in the interval $(c_2, c_2+\Delta c_2)$, or,

$$p(T_1)\Delta T = p(c_1)\Delta c_1 + p(c_2)\Delta c_2$$

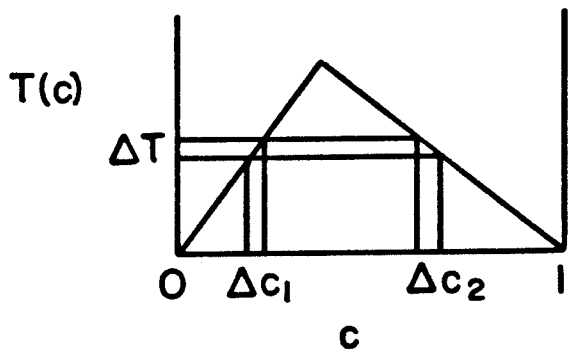

Figure D.3

$$p(T_1) = p(c_1)\left|\frac{\Delta c_1}{\Delta T}\right| + p(c_2)\left|\frac{\Delta c_2}{\Delta T}\right|$$

or

$$p(T_1) = p(c_1)\left|\frac{\partial c}{\partial T}\right|_{left} + p(c_2)\left|\frac{\partial c}{\partial T}\right|_{right} \tag{D.9}$$

(This is none other than the definition of the probability density function of a transformed variable for the special case that the transformation is not one to one, see Gutman, Wilks and Hunter [1971].)

Thus using two different runs, one can use the following technique (suggested by P.E. Dimotakis) to create a histogram representation of $p(c)$. If we write

$$\begin{bmatrix} 1 & . & 1 \\ - & - & - \\ & S_1 & \\ - & - & - \\ & S_2 & \end{bmatrix} \begin{bmatrix} P(0) \\ - \\ p(c) \\ - \\ p(1) \end{bmatrix} = \begin{bmatrix} 1 \\ - \\ p(0) \\ p(T) \\ p(1) \end{bmatrix} \tag{D.10}$$

where S_1 and S_2 are the (sparse) matrices constructed from $\left|\frac{\partial c}{\partial T}\right|_{left\ or\ right}$ for

runs 1 and 2. The first of these simultaneous equations requires that the probability is properly normalized. Matrix inversion then yields $p(T)$.

D.2.3. *Franklin Methods.* The final approach uses the Franklin solutions which are described below. This technique utilizes the cumulative distribution function to compute analytically the probability density function. In the following discussion the variables x, y are equivalent to c, T that have been used to this point.

D.2.3.1 *Franklin 1.* The cumulative distribution function is defined

$$F(x) = P\{X \leq x\} = \int_0^x p(\xi) d\xi \tag{D.11}$$

suppose that y has a cumulative distribution function G, then from Figure D.4,

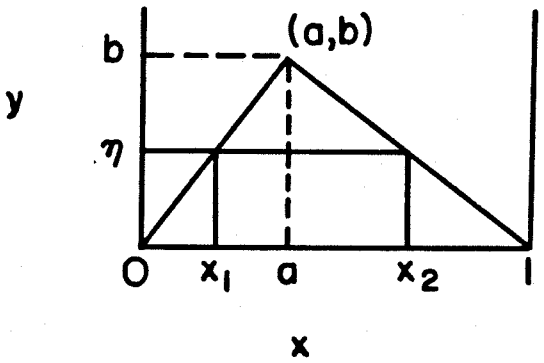

Figure D.4

$$G(\eta) = P\{Y \leq \eta\}$$

$$= P\{X \leq x_1\} + P\{X \geq x_2\}$$

$$= P(X \leq \frac{a\eta}{b}) + P(X \geq 1 - \frac{(1-a)\eta}{b})$$

or

$$G(y) = F(\frac{ay}{b}) + 1 - F(1 - \frac{(1-a)}{b}y) \tag{D.12}$$

without loss of generality, consider the cases $a = 1/3$ and $a = 2/3$ (these would correspond to runs of 1:2 ($L.S.:H.S.$) and 2:1 respectively) with cumulative distribution functions $G(y)$ and $H(y)$, then

$$G(y) = F(\frac{y}{3}) + 1 - F(1 - \frac{2y}{3}), \quad 0 \leq y \leq 1 \tag{D.13.a}$$

$$H(y) = F(\frac{2y}{3}) + 1 - F(1 - \frac{y}{3}), \quad 0 \leq y \leq 1 \tag{D.13.b}$$

then

$$H(2y) = F(\frac{4y}{3}) + 1 - F(1 - \frac{2y}{3}), \quad 0 \leq y \leq 1/2$$

subtracting

$$G(y) - H(2y) = F(\frac{y}{3}) - F(\frac{4y}{3}), \quad 0 \leq y \leq 1/2$$

rewriting

$$F(\frac{4y}{3}) = H(2y) - G(y) + F(\frac{y}{3}), \qquad 0 \le y \le 1/2$$

$$F(y) = H(\frac{3y}{2}) - G(\frac{3y}{4}) + F(\frac{y}{4}), \quad 0 \le y \le 2/3$$

or

$$F(y) = K(y) + F(\frac{y}{4}), \qquad 0 \le y \le 2/3$$

where

$$K(y) = H(\frac{3y}{2}) - G(\frac{3y}{4})$$

This provides a recursion relationship to compute $F(y)$

$$F(y) = K(y) + K(\frac{y}{4}) + \cdots + K(\frac{y}{4^n}) + F(\frac{y}{4^{n+1}})$$

where the last term is $O(\frac{1}{4^n})$, implying rapid convergence. Thus,

$$F(y) = \sum_{n=0}^{\infty} \left[H(\frac{3y}{2\,4^n}) - G(\frac{3y}{4^{n+1}}) \right], \quad 0 \le y \le 2/3$$

and using Equation (D.13.b)

$$F(y) = 1 + F(2(1-y)) - H(3(1-y)), \quad 2/3 \le y \le 1$$

The probability density function $f(y)$ is now obtained by differentiating the expressions for $F(y)$, i.e.,

$$f(y) = \sum_0^{\infty} \left[\frac{3}{2} \frac{1}{4^n} h\left(\frac{3y}{2\,4^n}\right) - \frac{3}{4^{n+1}} g\left(\frac{3y}{4^{n+1}}\right) \right], \quad 0 \le y \le 2/3 \quad \text{(D.14.a)}$$

$$f(y) = -2f(2(1-y)) + 3h(3(1-y)), \qquad 2/3 \le y \le 1 \quad \text{(D.14.b)}$$

Thus, knowing the histograms g and h, for two different runs, one can compute the probability density function, f.

D.2.3.2 *Franklin 2.* The second Franklin solution is derived from Equation (D.12)

$$G(\eta,\alpha) = F(\alpha\eta) + 1 - F(1-\eta+\eta\alpha)$$

then

$$\frac{\partial G}{\partial \eta} = \alpha f(\alpha\eta) + (1-\alpha) f(1-\eta+\eta\alpha)$$

$$\frac{\partial G}{\partial \alpha} = \eta f(\alpha\eta) - \eta f(1-\eta+\eta\alpha)$$

solving for $f(\alpha\eta)$ and $f(1-\eta+\eta\alpha)$ by Cramer's Rule, yields

$$f(\alpha\eta) = \frac{\partial G}{\partial \eta} + \frac{1-\alpha}{\eta} \frac{\partial G}{\partial \alpha}, \quad \alpha\eta = x, \text{ fixed} \qquad \text{(D.15)}$$

Thus, if one has sufficient information to construct the partial derivatives that exist on the right hand side, one can compute the function f.

D.2.3.3 *Franklin 3.* A special case of the Franklin 2 solution occurs for $\eta = 1$, then Equation (D.15) becomes

$$f(a) = G_\eta(1,a)$$

$$= \frac{G(1,a)-G(1-\varepsilon,a)}{\varepsilon}$$

this can be related to a simple physical observation (see Figure D.5), namely,

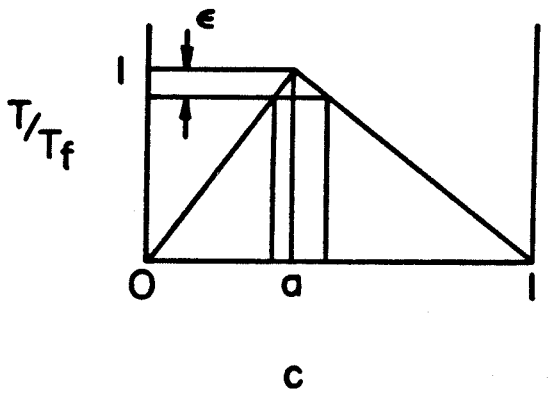

Figure D.5

$$P(y > 1-\varepsilon) = 1 - G(1-\varepsilon)$$

$$\approx \varepsilon f(a)$$

i.e. if the function G is stored in histogram form, then $f(a)$ can be obtained simply from the uppermost bins. The advantage of this approach is that the results are always positive since the histogram is non-negative.

Attempts to use the Franklin 1,2 solutions yielded negative solutions, owing to inaccuracies in the histogram data which are caused by inadequate frequency response, conduction error and poor resolution (Appendix C). The simplest version of this solution, Franklin 3, was used to give an estimate of the *pdf*. This result is discussed in Chapter 3.

References

BATT, R.G. 1977 Turbulent Mixing of Passive and Chemically Reacting Species in a Low-Speed Shear Layer. *J. Fluid Mech.*, **82**, 53-95.

BERNAL, L.P. 1981 The Coherent Structure of Turbulent Mixing Layers: I. Similarity of the Primary Vortex Structure. II. Secondary Streamwise Vortex Structure. Ph.D. Thesis, Caltech.

BOND, D.L., GUENTHER, M.E., STIMPSON, L.D., TOTH, L.R., & YOUNG, D.L. 1979 Experience with Fluorine and Its Safe Use as a Propellant. JPL Publication 79-64.

BREIDENTHAL, R.E. 1978 A Chemically Reacting, Turbulent Shear Layer. Ph.D. Thesis, Caltech; and 1981 Structure in Turbulent Mixing Layers and Wakes using a Chemical Reaction. *J.Fluid Mech.*, **109**, 1-24.

BROADWELL, J.E. & BREIDENTHAL, R.E. 1981 A Simple Model of Mixing and Chemical Reaction in a Turbulent Shear Layer. GALCIT Report FM81-10; and 1982 *J. Fluid Mech.*, **125**.

BROWN, G.L. & REBOLLO, M.R. 1972 A Small, Fast Response Probe to Measure Composition of a Binary Gas Mixture. *AIAA J.* **10(5)**, 649-652.

BROWN, G.L. & ROSHKO, A. 1974 On Density Effects and Large Structure in Turbulent Mixing Layers. *J. Fluid Mech.* **64(4)**, 775-816.

BURKE, S.P. & SCHUMANN, T.E.W. 1928 Diffusion Flames, *Ind. Eng. Chem.*, **20**, 998-1006.

CHEN, H., DAUGHETRY, J.D. & FYFE, W. 1975 $TA5 - H_2/F_2$. Flame Propagation and Repetitively Pulsed Hydrogen Fluoride (HF) Chain - Reaction Laser. *IEEE J. Quantum Electronics*, **QE-11, 8**, 648-653.

CHMIELEWSKI, G.E. 1974 Boundary Layer Considerations in the Design of Aerodynamic Contractions, *J. Aircraft.* **11**, 435-438.

COHEN, N. & BOTT, J.F. 1982 Review of Rate Data for Reactions of Interest in HF and DF Lasers. The Aerospace Corporation, Report SD-TR-82-86.

COOL, T.A., STEPHENS, R.R. & SHIRLEY, J.A. 1970 HCl, HF, and DF Partially Inverted cw Chemical Lasers. *J. Appl. Phys.* **41(10)**, 4038-4050.

DIMOTAKIS, P.E. & BROWN, G.L. 1976 The Mixing Layer at High Reynolds Number: Large Structure Dynamics and Entrainment. *J. Fluid Mech.* **78(3)**, 535-560.

FIEDLER, H.F. 1974 Transport of Heat Across a Plane Turbulent Mixing Layer. *Advances in Geophysics*, **18A**, Academic Press, 93-109.

FIEDLER, H.F. 1975 On Turbulent Structure and Mixing Mechanisms in Free Turbulent Shear Flows. In *Turbulent Mixing in Nonreactive and Reactive Flows, A Project SQUID Workshop*. Plenum Press, 381-410.

GANJI, A.T. & SAWYER, R.F. 1980 Turbulence, Combustion, Pollutant, and Stability Characterization of a Premixed, Step Combustor. *NASA CR 3230.*

Gmelin Handbuch der Anorganischen Chemie 1980 F Fluorine, Supplement Vol. 2, System-Nummer 5, Springer-Verlag, 108.

GUTMAN, I., WILKS, S.S. & HUNTER, J.S. 1971 Introductory Engineering Statistics, Second Edition, John Wiley & Sons, Inc., 128.

KONRAD, J.H. 1976 An Experimental Investigation of Mixing in Two-Dimensional Turbulent Shear Flows with Application to Diffusion-Limited Chemical Reactions. Ph.D. Thesis, Caltech, and *Project SQUID Technical Report* CIT-8-PU.

LIBBY, P.A. & WILLIAMS, F.A. 1980 Turbulent Reacting Flows, *Topics in Applied Physics*, **44**, Springer-Verlag, 76.

LIÑAN, A. 1981 Lewis Number Effects on the Structure and Extinction of Diffusion Flames due to Strain. In *The Role of Coherent Structures in Modelling Turbulence and Mixing, Proceedings, Madrid 1980.* Lecture Notes in Physics, **136**, Springer-Verlag, 333-339.

MARBLE, F.E. & BROADWELL, J.E. 1977 The Coherent Flame Model for Turbulent Chemical Reactions. *Project SQUID Technical Report* TRW-9-PU.

Matheson Gas Data Book 1980 6th edition, Matheson Gas Co., 330.

PARANTHOEN, P., LECORDIER, J.C. & PETIT, C. 1982 Influence of Dust Contamination on Frequency Response of Wire Resistance Thermometers. *DISA Information*, **27**, 36-37.

RAJAGOPALAN, S. & ANTONIA, R.A. 1981 Properties of the Large Structure in a Slightly Heated Turbulent Mixing Layer of a Plane Jet, *J. Fluid Mech.*, **105**, 261-281.

RAPP, D. & JOHNSTON, H.S. 1960 Nitric Oxide-Fluorine Dilute Diffusion Flame, *J. Chem. Phys*, **33(3)**, 695-699.

SANDBORN, V.A. 1972 Resistance Temperature Transducers, Metrology Press, 428.

SCADRON, M.D. & WARSHAWSKY, I. 1952 Experimental Determination of Time Constants and Nusselt Numbers for Bare-Wire Thermocouples in High-Velocity Air Streams and Analytic Approximation of Conduction and Radiation Errors, *NACA TN 2599.*

SCHMIDT, H.W. 1967 Fluorine and Fluorine-Oxygen Mixtures in Rocket Systems. *NASA SP 3037.*

THAYER, W.J. III, BUONADONNA, V.R., SHERMAN, W.D. & McCLURE, J.D. 1978 Pulsed Chemical Laser Flow Technology, Boeing Aerospace Co. Report No. D180-24039-1.

TOOR, H.L 1962 Mass Transfer in Dilute Turbulent and Nonturbulent Systems with Rapid Irreversible Reactions and Equal Diffusivities, *AIChE J.* **8(1)**, 70-78.

WALLACE, A.K. 1981 Experimental Investigation of the Effects of Chemical Heat Release in the Reacting Turbulent Plane Shear Layer, Ph.D. Thesis, The University of Adelaide.

WINANT, C.D. & BROWAND, F.R. 1974 Vortex Pairing: the Mechanism of Turbulent Mixing Layer Growth at Moderate Reynolds Number, *J. Fluid Mech.*, **20**, 417-432.

WITTE, A.B., BROADWELL, J.E., SHACKLEFORD, W.L., CUMMINGS, J.C., TROST, J.E., WHITMAN, A.S., MARBLE, F.E., CRAWFORD, D.R., JACOBS, T.A. 1974 Aerodynamic Reactive Flow Studies of the H_2F_2 Laser-II, Air Force Weapons Lab, Kirtland Air Force Base, New Mexico, AFWL-TE-74-78, 33.

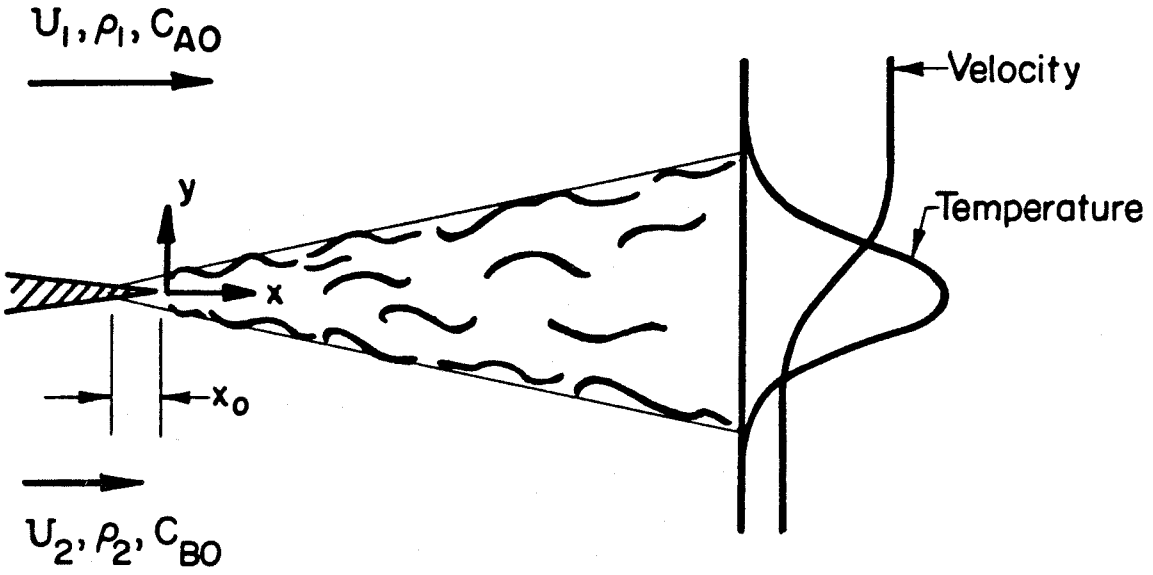

A = High Speed Reactant (H_2 or F_2)

B = Low Speed Reactant (F_2 or H_2)

$H_2 + F_2 \longrightarrow 2HF$

FIGURE 1 Turbulent Shear Layer Geometry

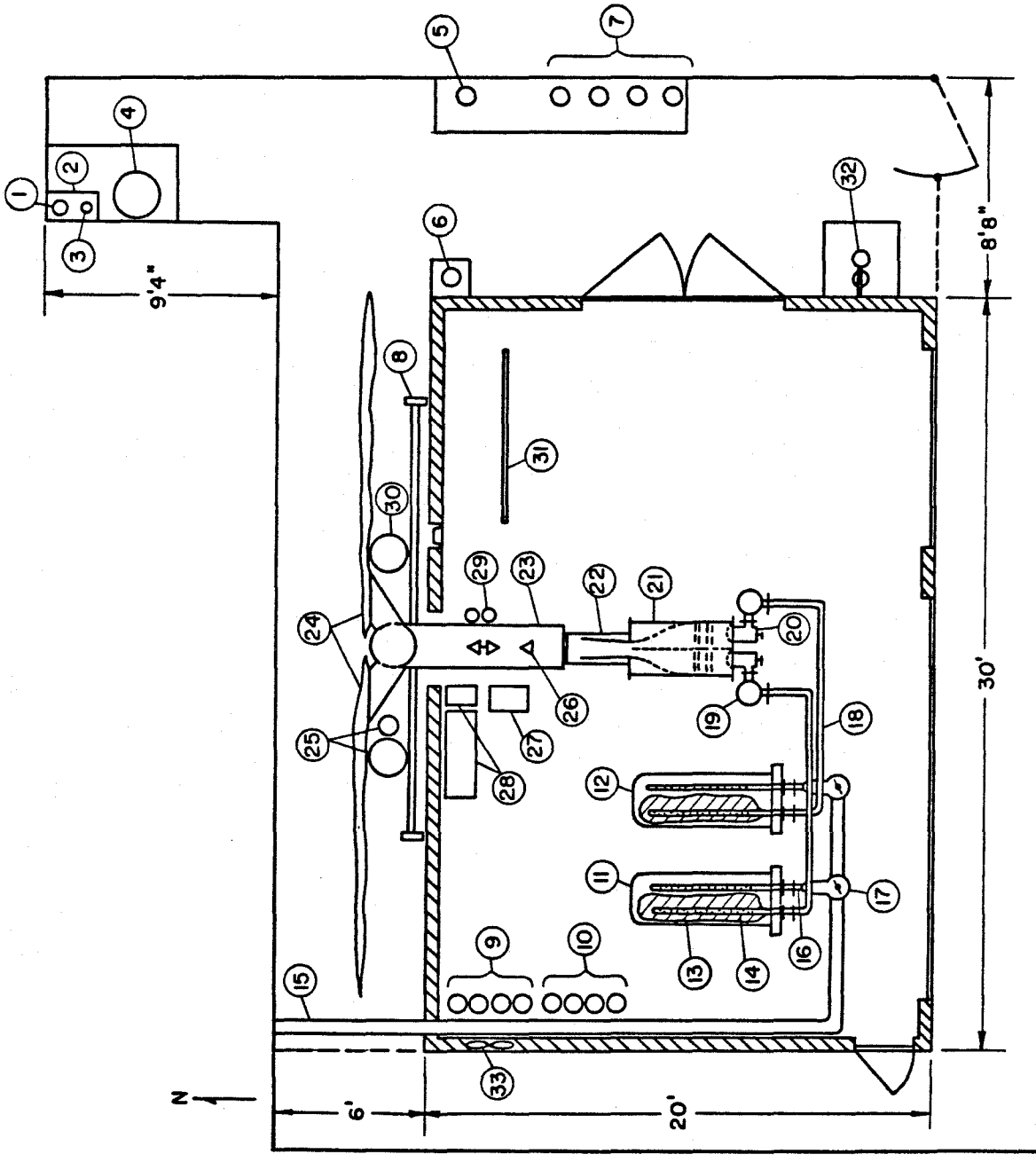

FIGURE 2a Layout of GALCIT Reacting Shear Flow Lab

1. Fluorine Cylinder
2. 1/8 Inch Steel Barrier
3. Hydrogen Fluoride Absorber
4. Charcoal Burn Barrel
5. Hydrogen Cylinder
6. Nitric Oxide Cylinder
7. Nitrogen Tank Farm (Surge Tank)
8. Fluorine Mixing Vessel (Not Shown - Hydrogen Mixing Vessel)
9. Inert Gas Tank Farm (Hydrogen Side)
10. Inert Gas Tank Farm (Fluorine Side)
11. Fluorine Reactant Tank
12. Hydrogen Reactant Tank
13. Upstream Teflon Bag
14. Perforated Tube
15. 6 Inch High Pressure Line to Surge Tank
16. 3 Inch Check Valve
17. 6 Inch Butterfly Valve
18. 3 Inch 304L Stainless Steel Inlet Line
19. 3 Inch Main Opening Valve
20. Sonic Metering Valve
21. Contraction Box
22. Test Section
23. Downstream Washing Duct
24. Teflon Exhaust Catch Bags
25. Sodium Hydroxide Supply Tanks
26. Sodium Hydroxide Showerheads
27. Sodium Hydroxide High Pressure Pump
28. Vacuum Pumps
29. Exhaust Gas Scrubber
30. Exhaust Liquid Catch Tank
31. Control Panel
32. Safety Shower
33. 18 Inch Diameter Explosion Proof Ventilator (Not shown - Natural Ventilation System)

FIGURE 2b Item List for GALCIT Reacting Shear Flow Lab

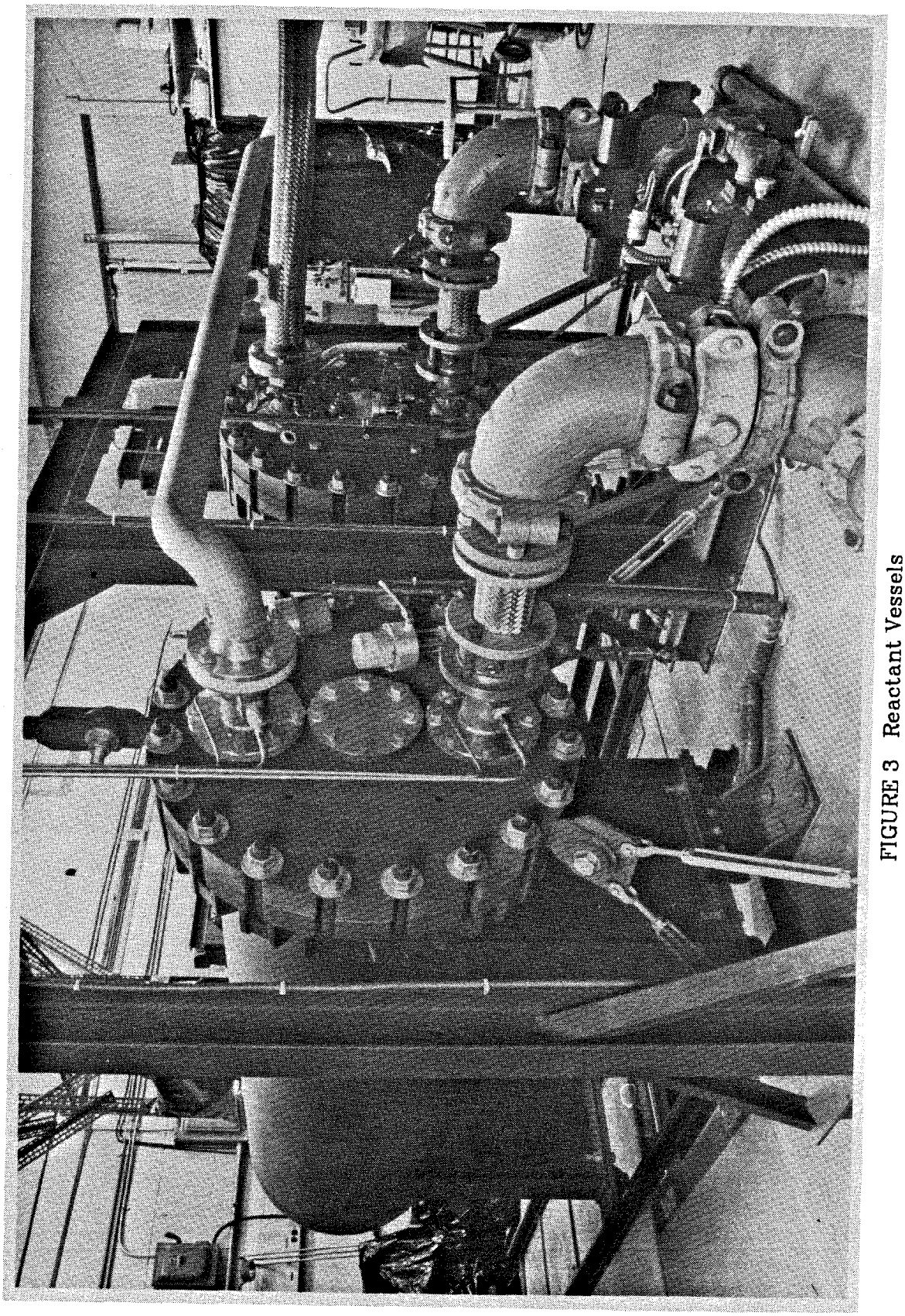

FIGURE 3 Reactant Vessels

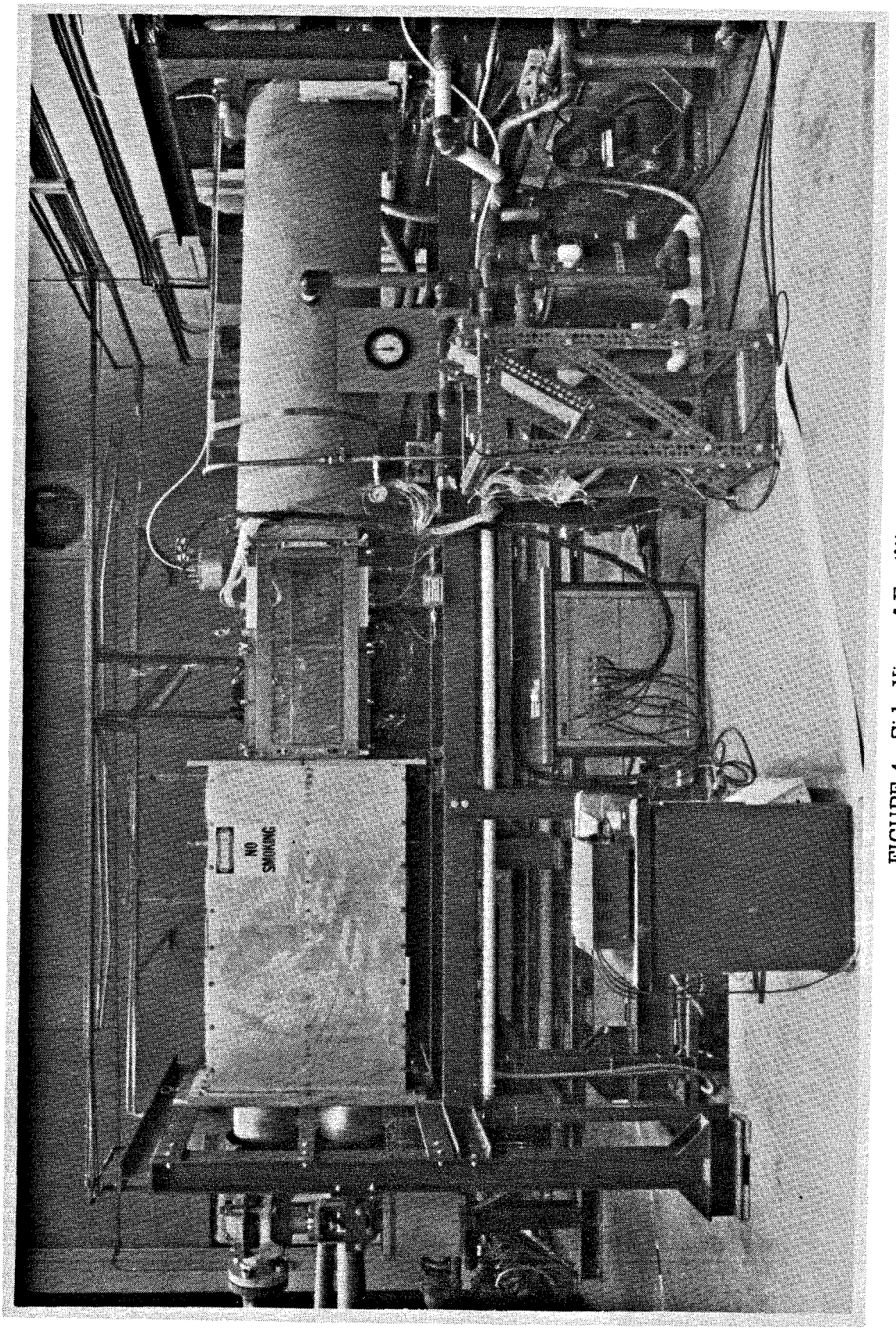

FIGURE 4 Side View of Facility

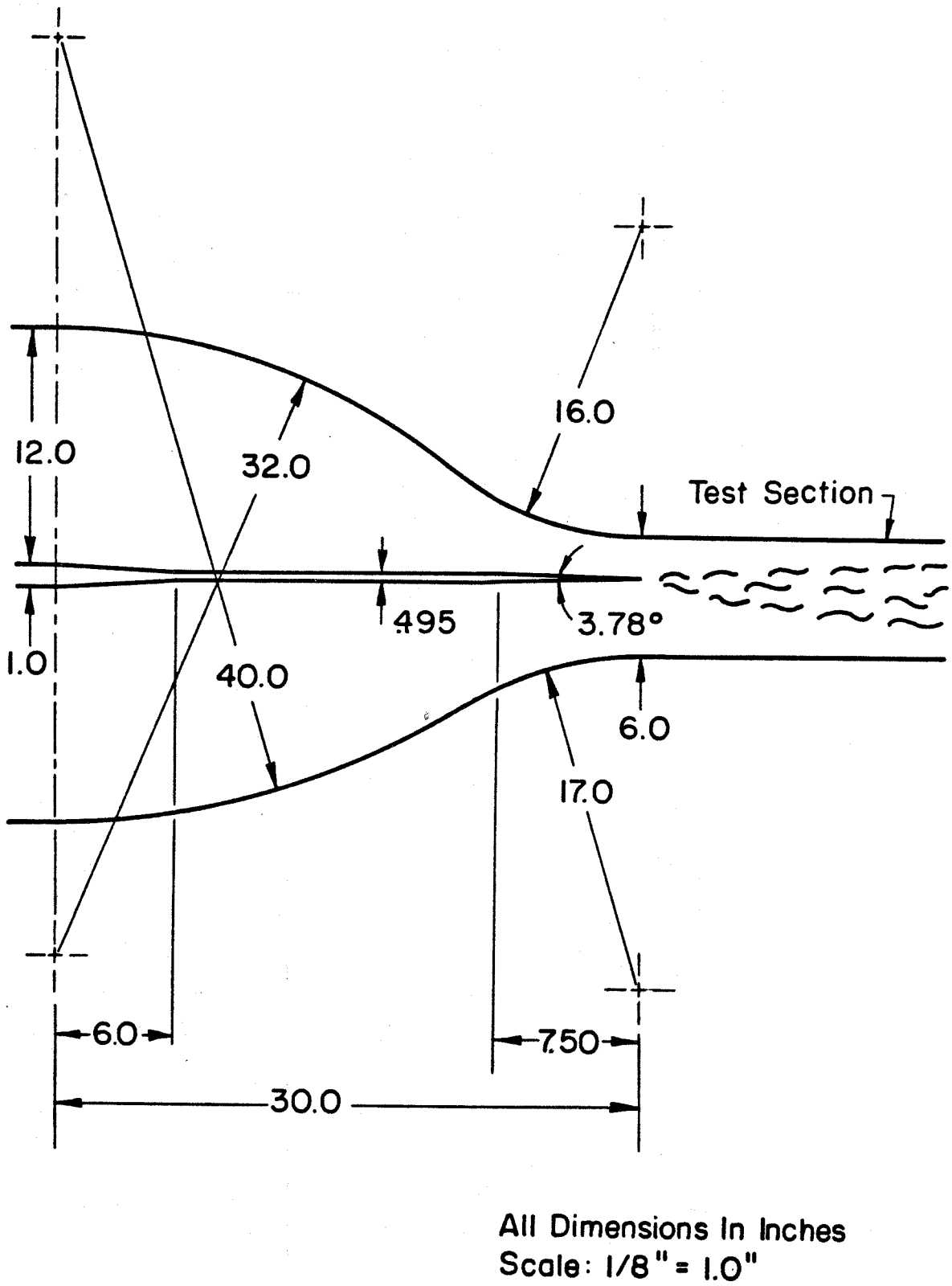

FIGURE 5 Contraction Dimensions

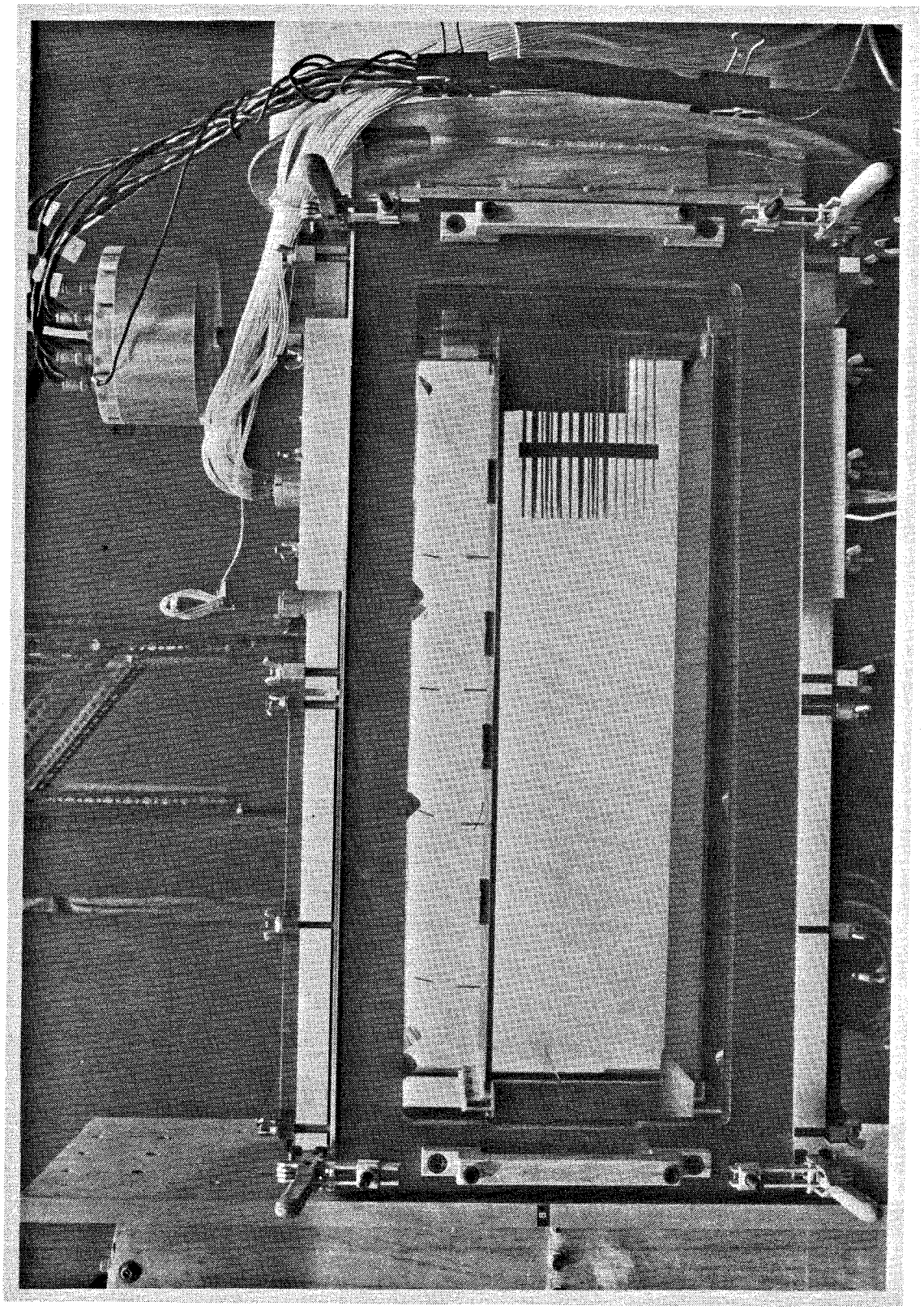

FIGURE 6 Closeup of Test Section

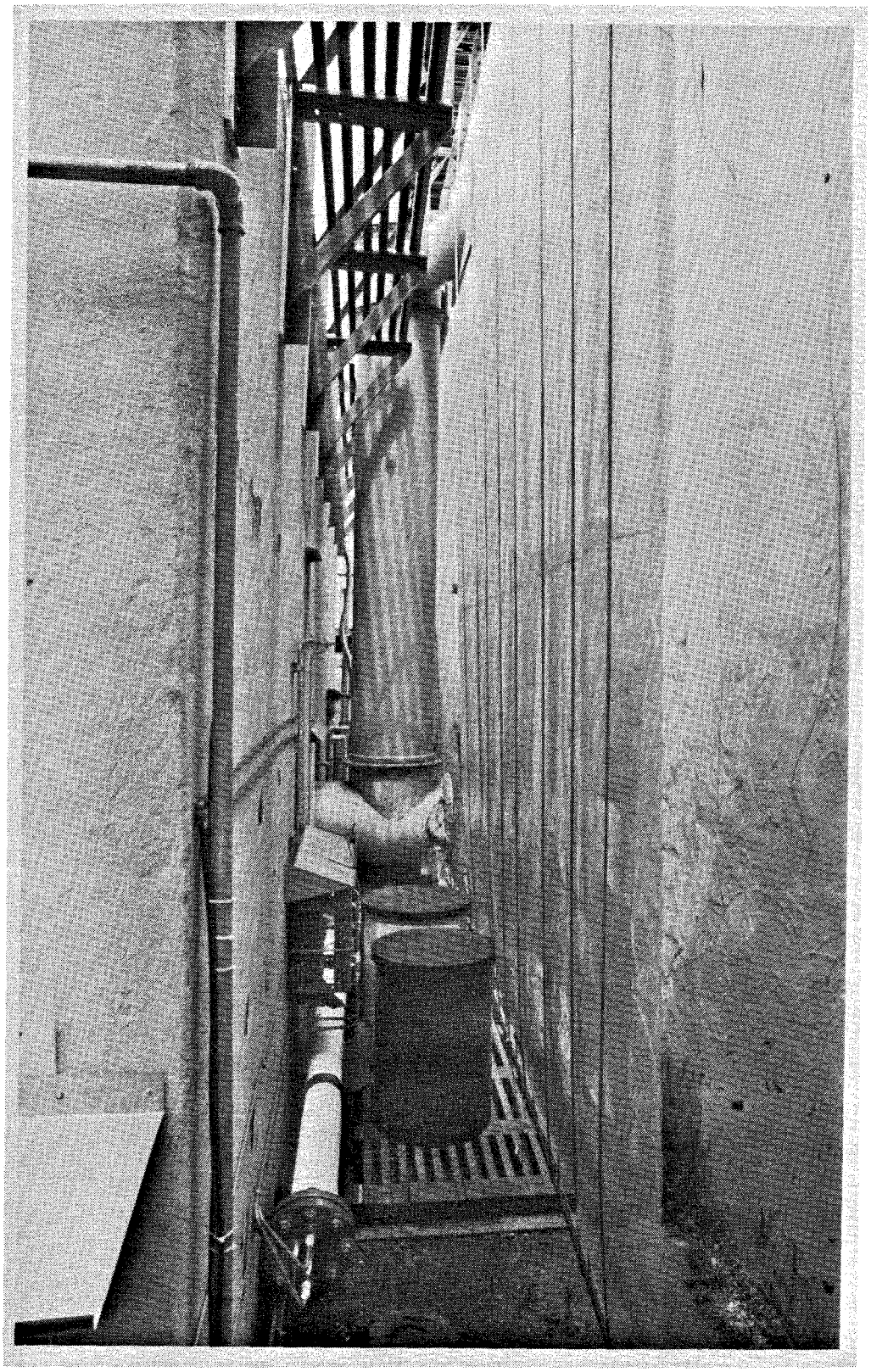

FIGURE 7 Vertical Duct and Exhaust Catch Bags

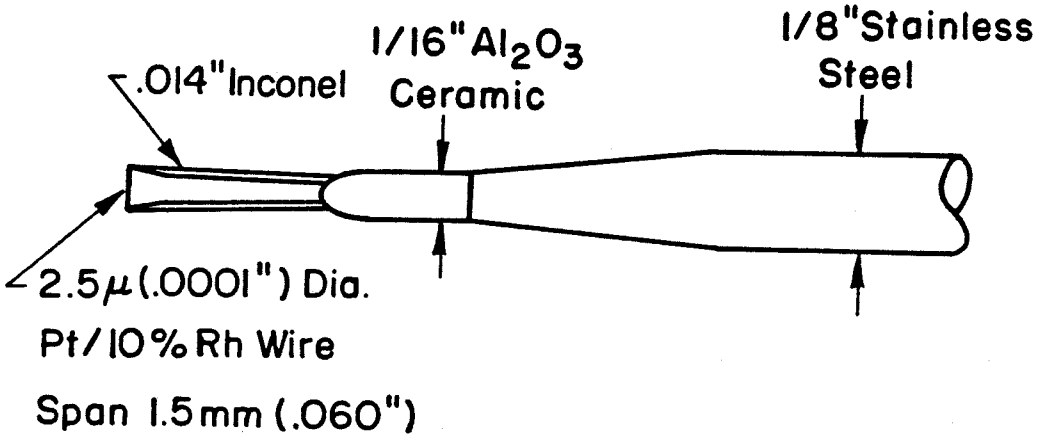

FIGURE 8 Cold Wire Probe

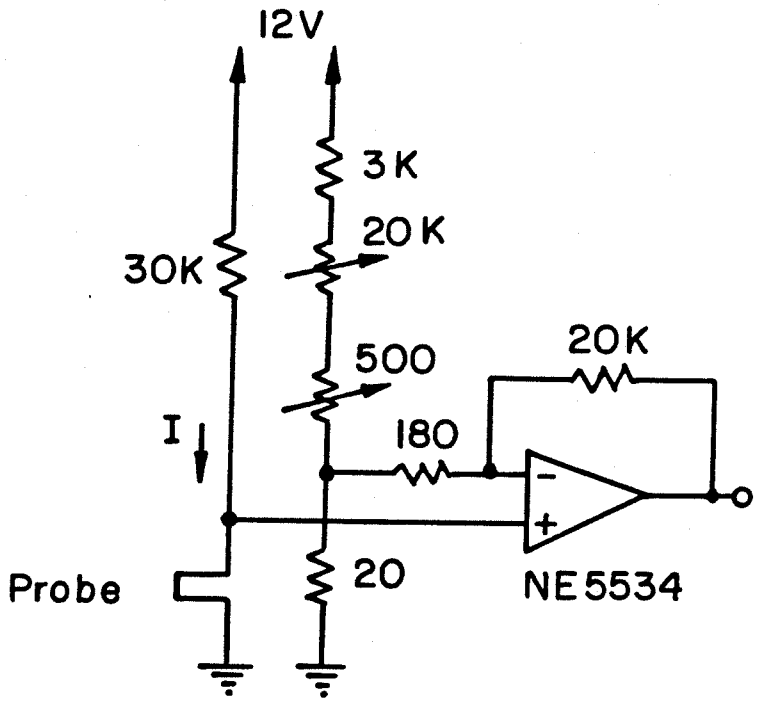

FIGURE 9 Circuit for Cold Wire Probe

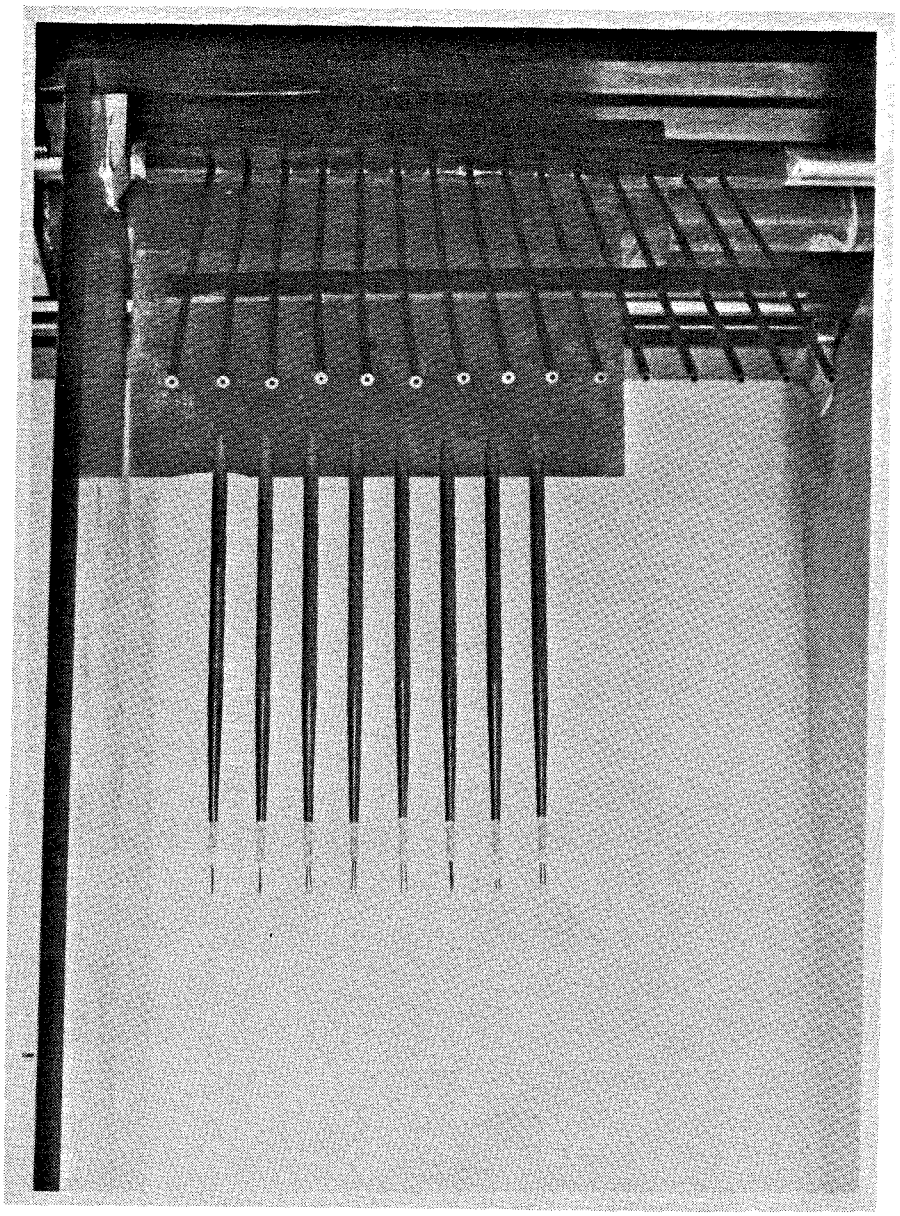

FIGURE 10 Temperature and Velocity Rakes

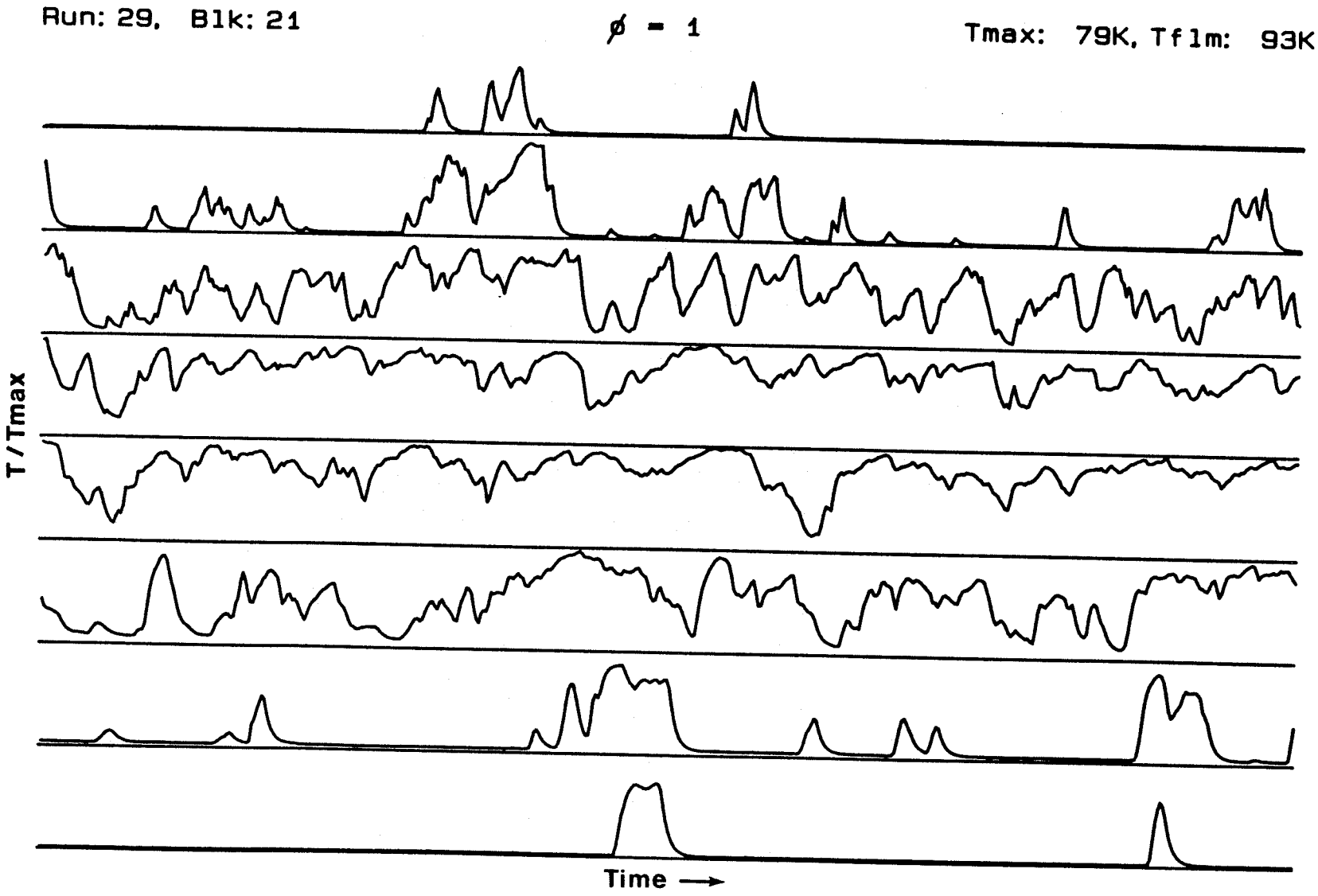

FIGURE 11a Temperature vs Time Trace, $\varphi = 1$, $r = 0.40$, $s = 1$, Run = 29. Flow from right to left, high speed on top. Time axis = 51.2 msec.

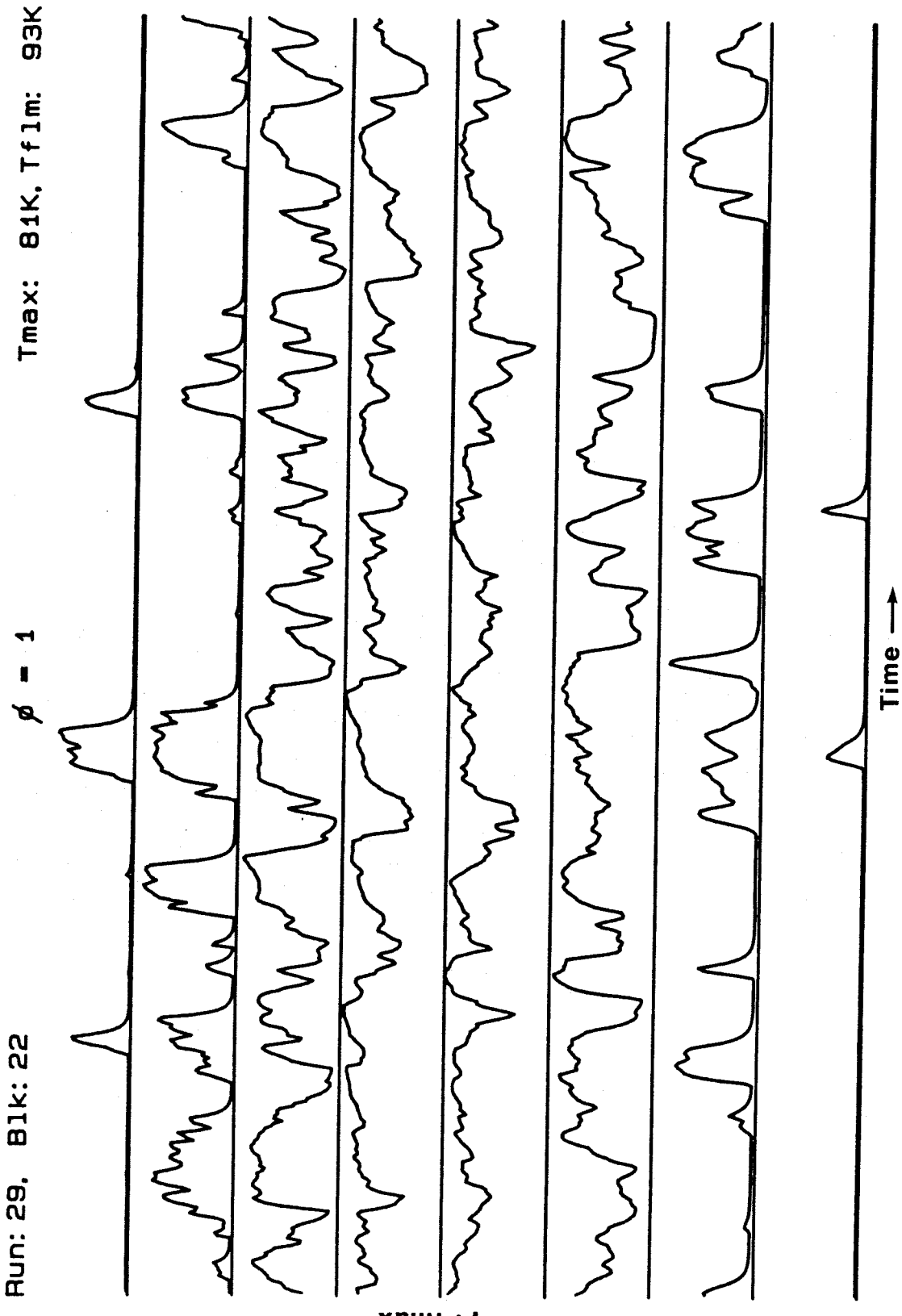

FIGURE 11b Temperature vs Time Trace, $\phi = 1$, $r = 0.40$, $s = 1$, Run = 29.
Flow from right to left, high speed on top. Time axis = 51.2 msec.

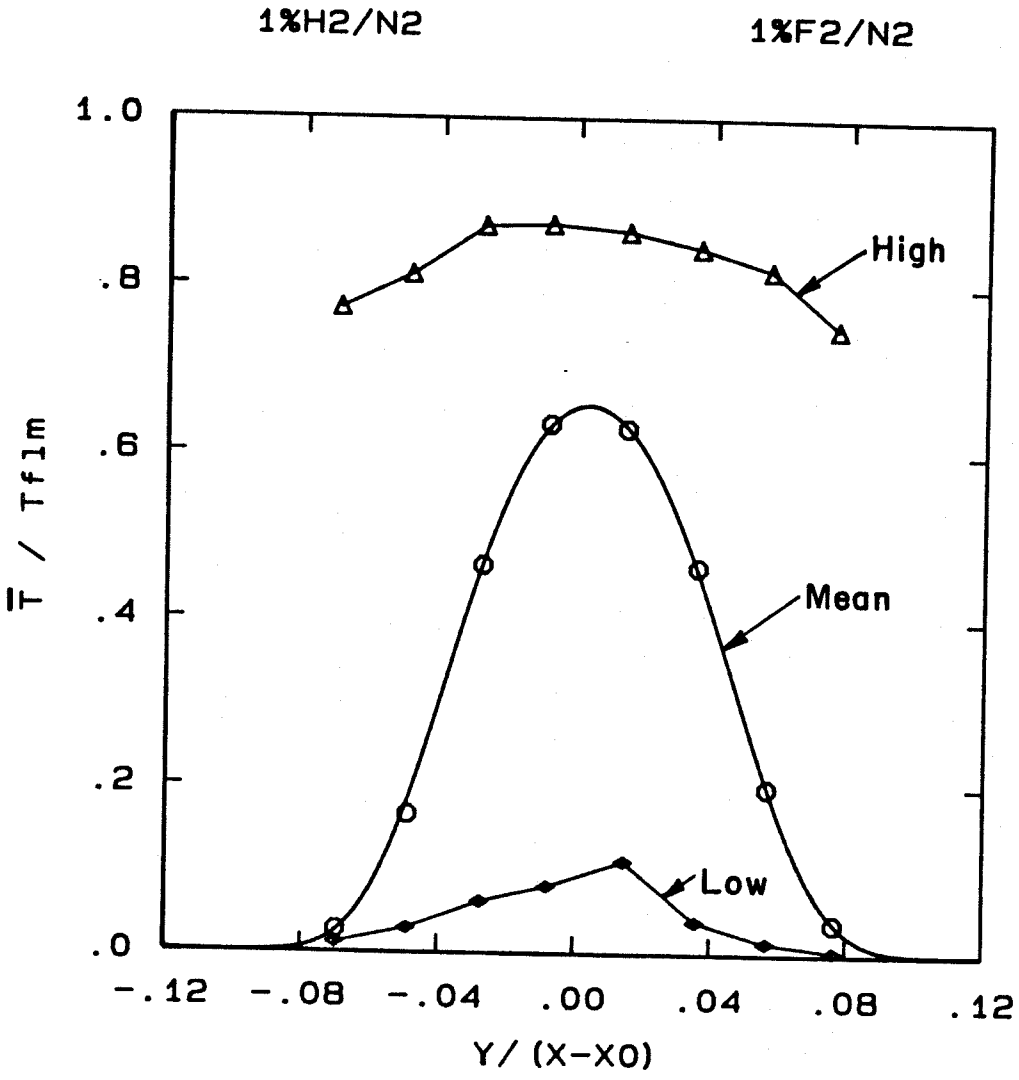

ϕ : 1

Run: 29

Tflm : 93.0

Thmg : 81.0

$\overline{T}$max/Tflm: 0.657

$\overline{T}$max/Thmg: 0.754

Area*10 : 0.556

$\delta_1/(X-XO)$: 0.168

FIGURE 11c Mean Temperature Profile, $\varphi = 1, r = 0.40, s = 1$, Run = 29

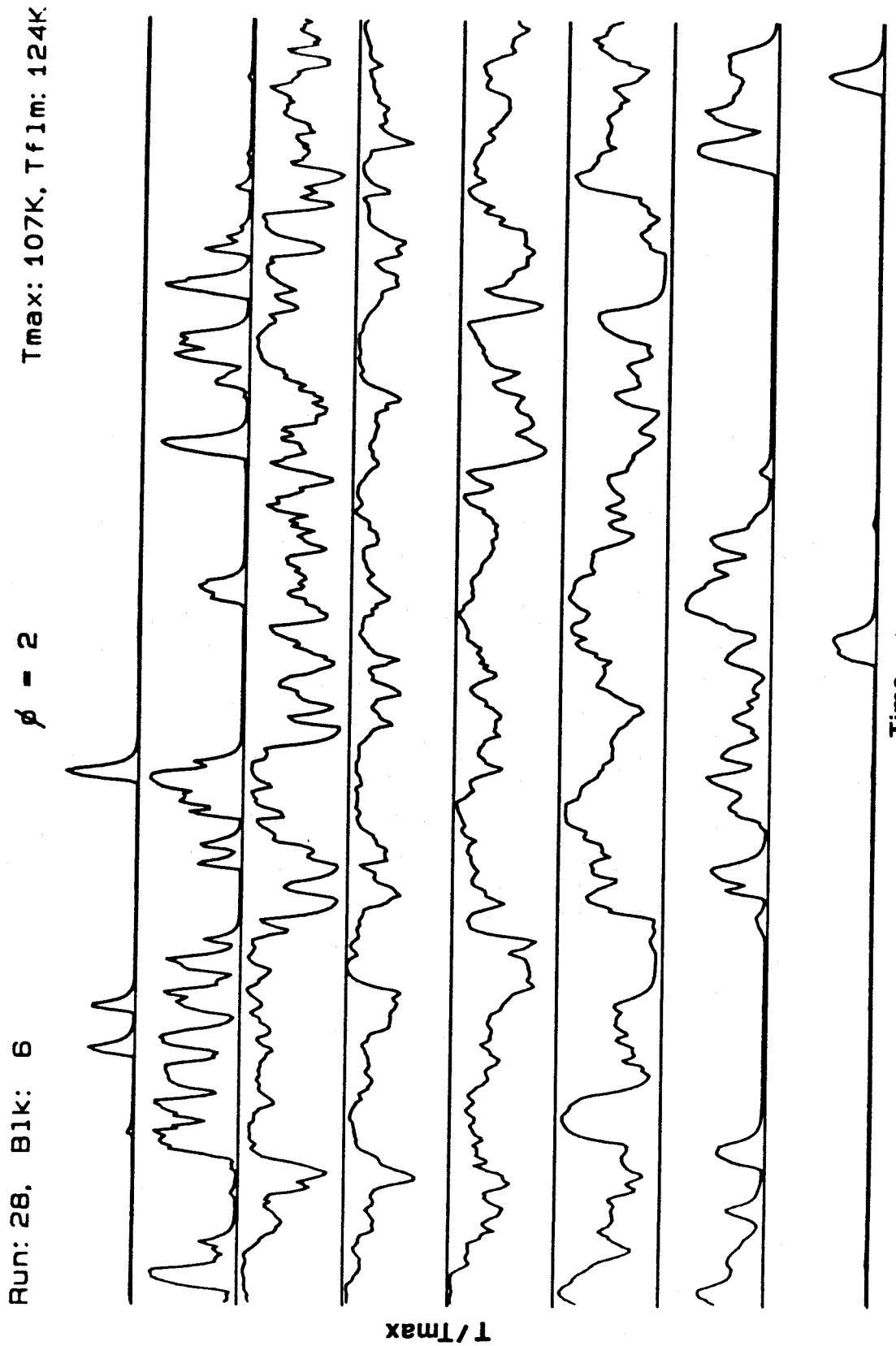

FIGURE 12a Temperature vs Time Trace, $\varphi = 2$, $\tau = 0.40$, $s = 1$, Run = 28. Flow from right to left, high speed on top. Time axis = 51.2 msec.

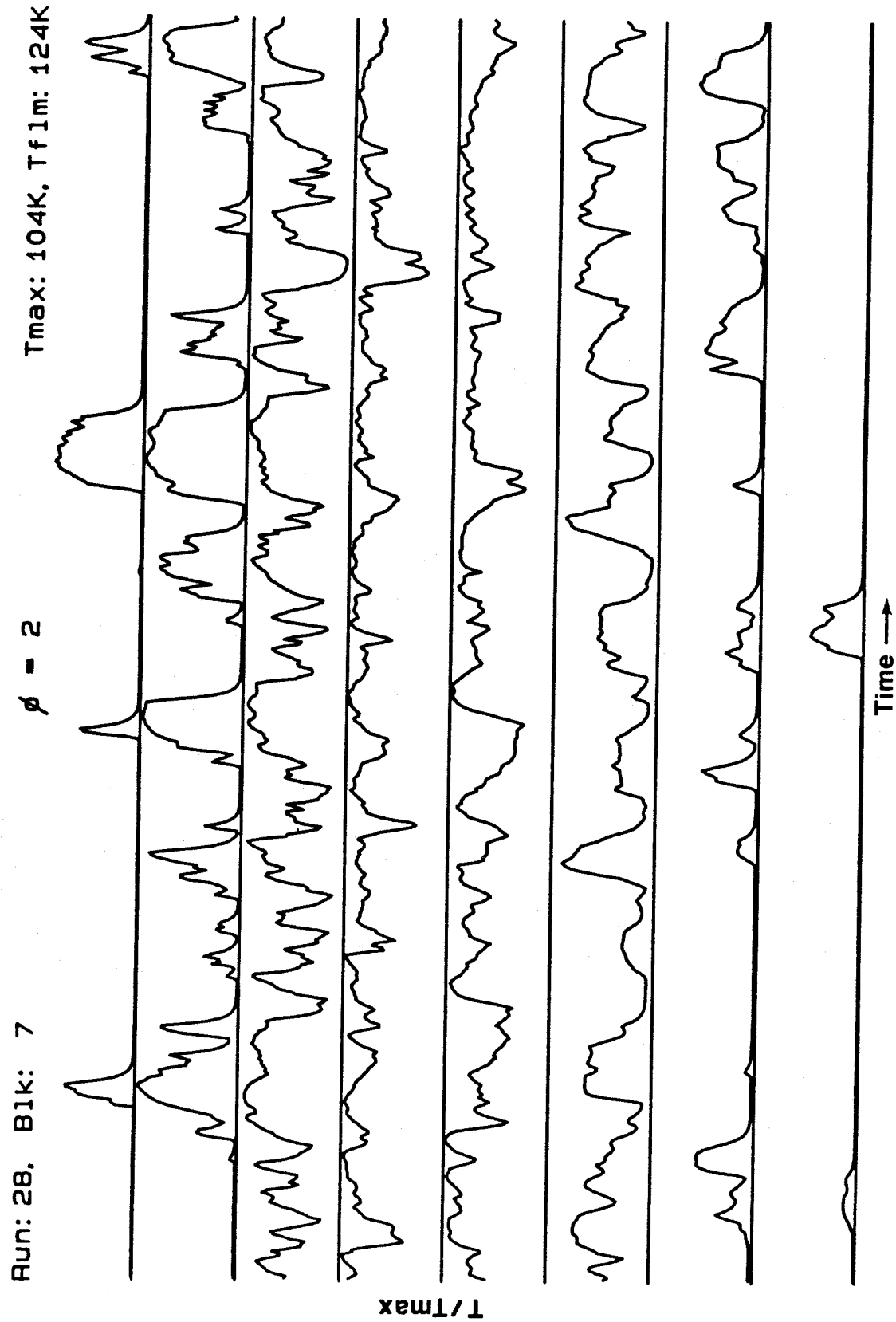

FIGURE 12b Temperature vs Time Trace, $\varphi = 2$, $\tau = 0.40$, $s = 1$, Run = 28. Flow from right to left, high speed on top. Time axis = 51.2 msec.

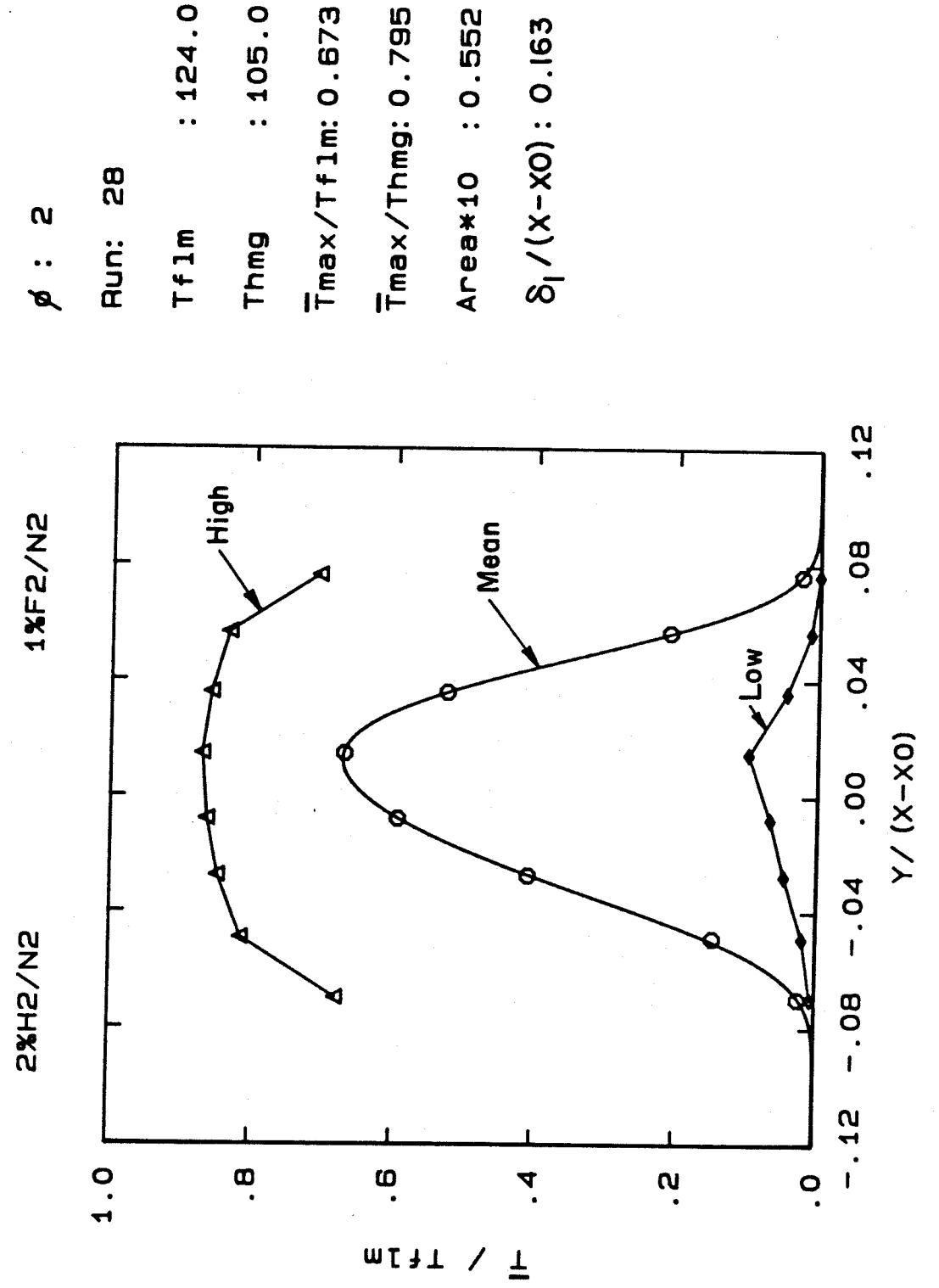

FIGURE 12c Mean Temperature Profile, $\varphi = 2$, $r = 0.40$, $s = 1$, Run = 28

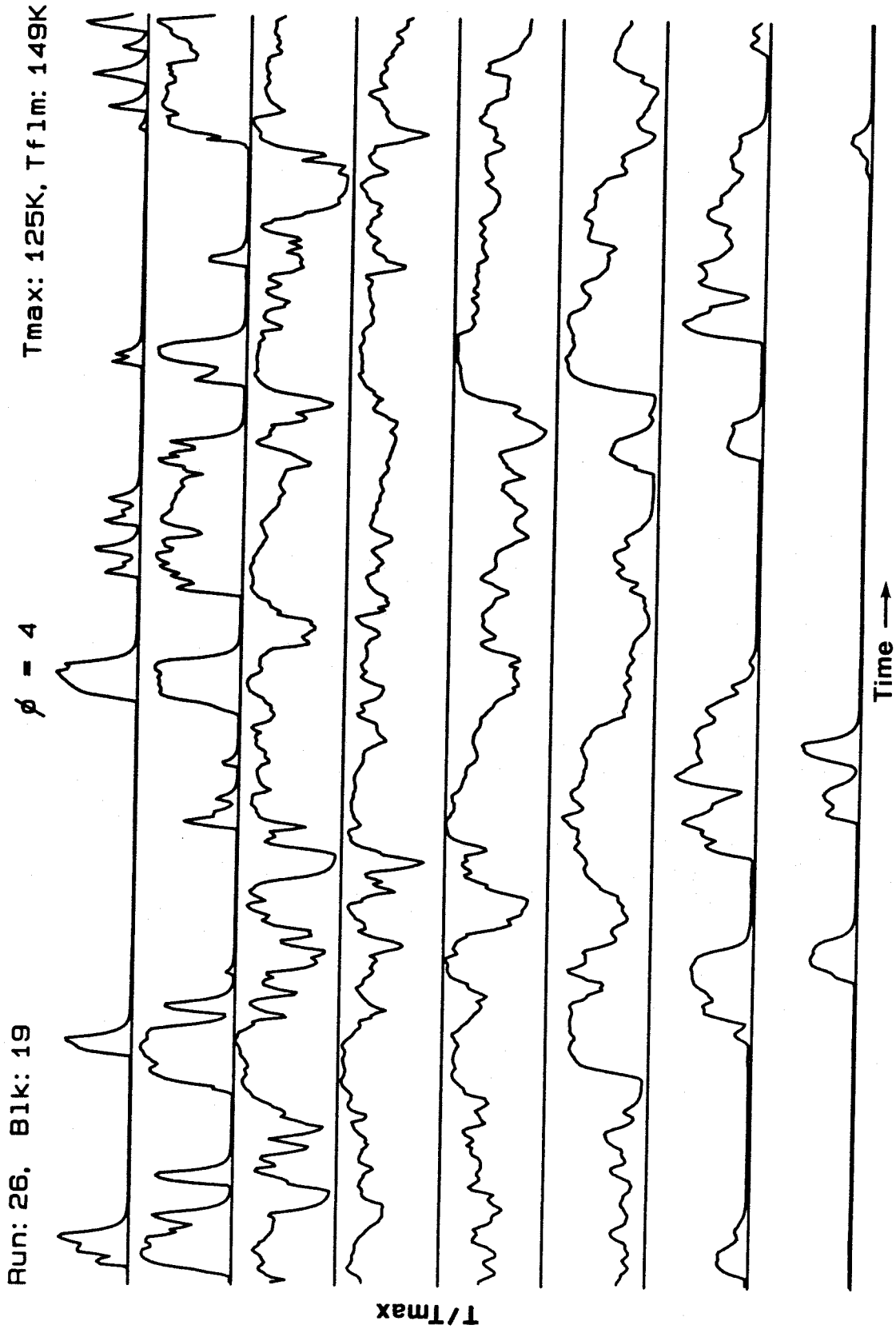

FIGURE 13a Temperature vs Time Trace, $\varphi = 4$, $\tau = 0.40$, $s = 1$, Run = 26. Flow from right to left, high speed on top. Time axis = 51.2 msec.

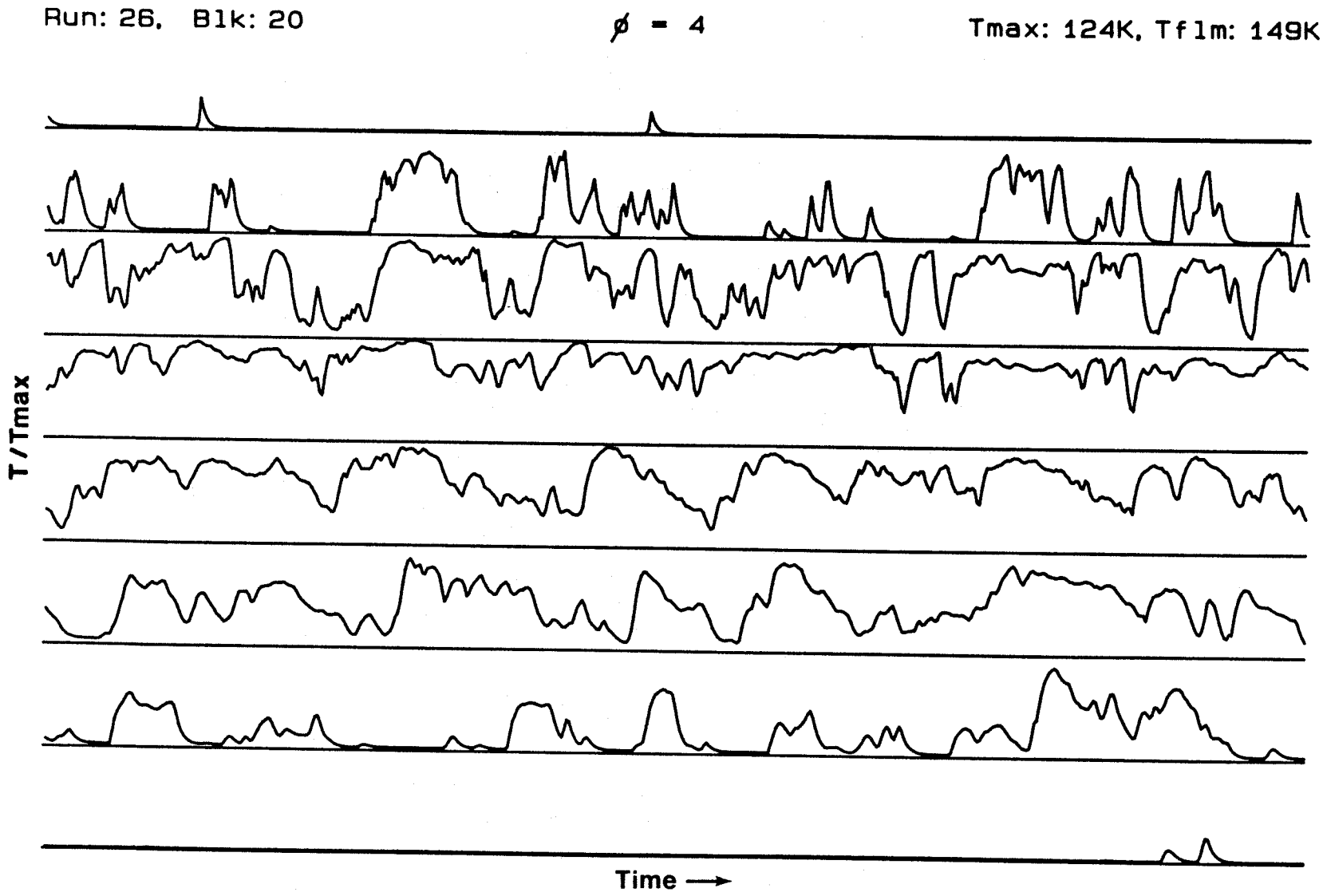

FIGURE 13b Temperature vs Time Trace, $\varphi = 4$, $r = 0.40$, $s = 1$, Run = 26. Flow from right to left, high speed on top. Time axis = 51.2 msec.

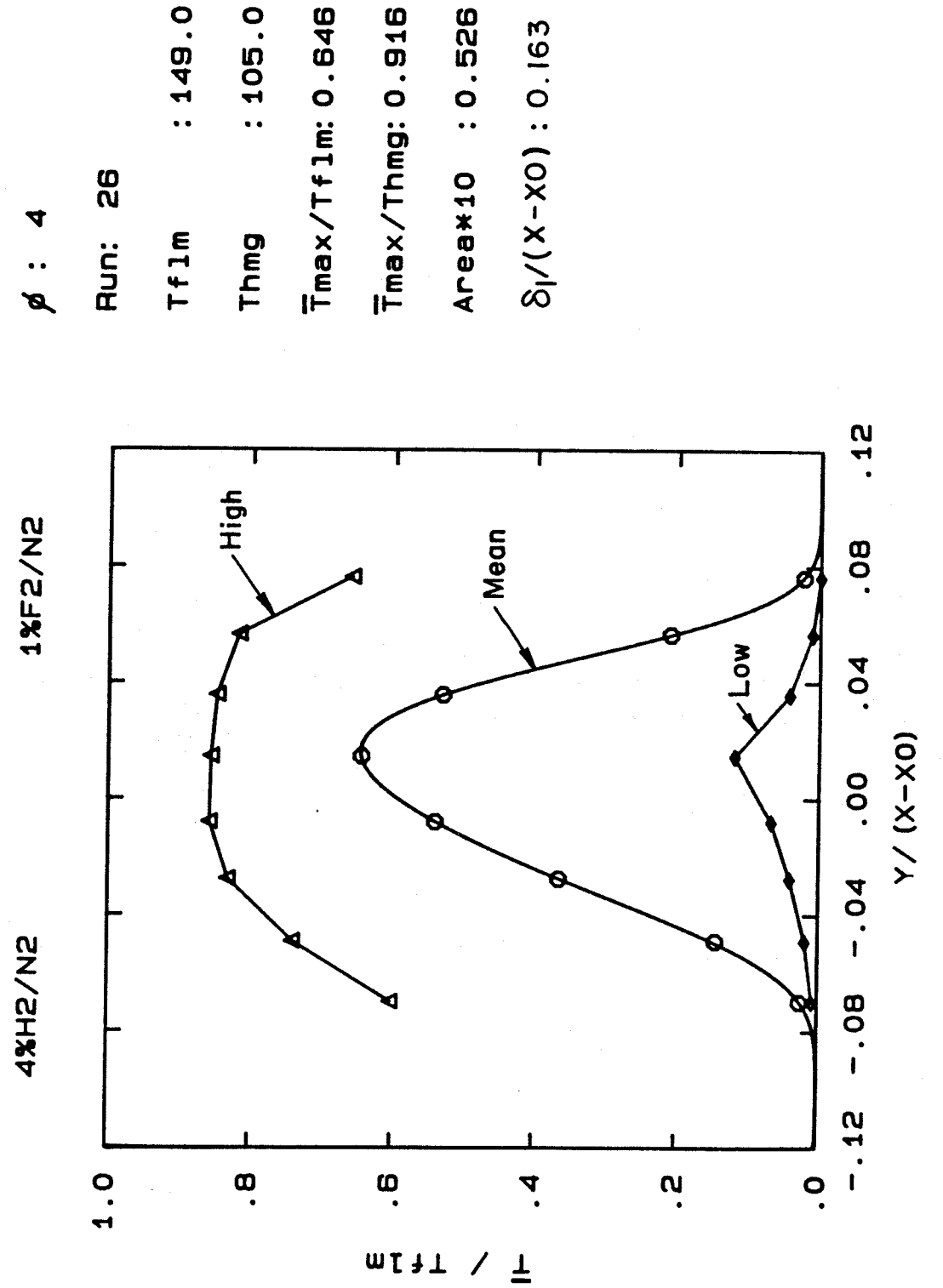

FIGURE 13c Mean Temperature Profile, $\varphi = 4, r = 0.40, s = 1$, Run = 26

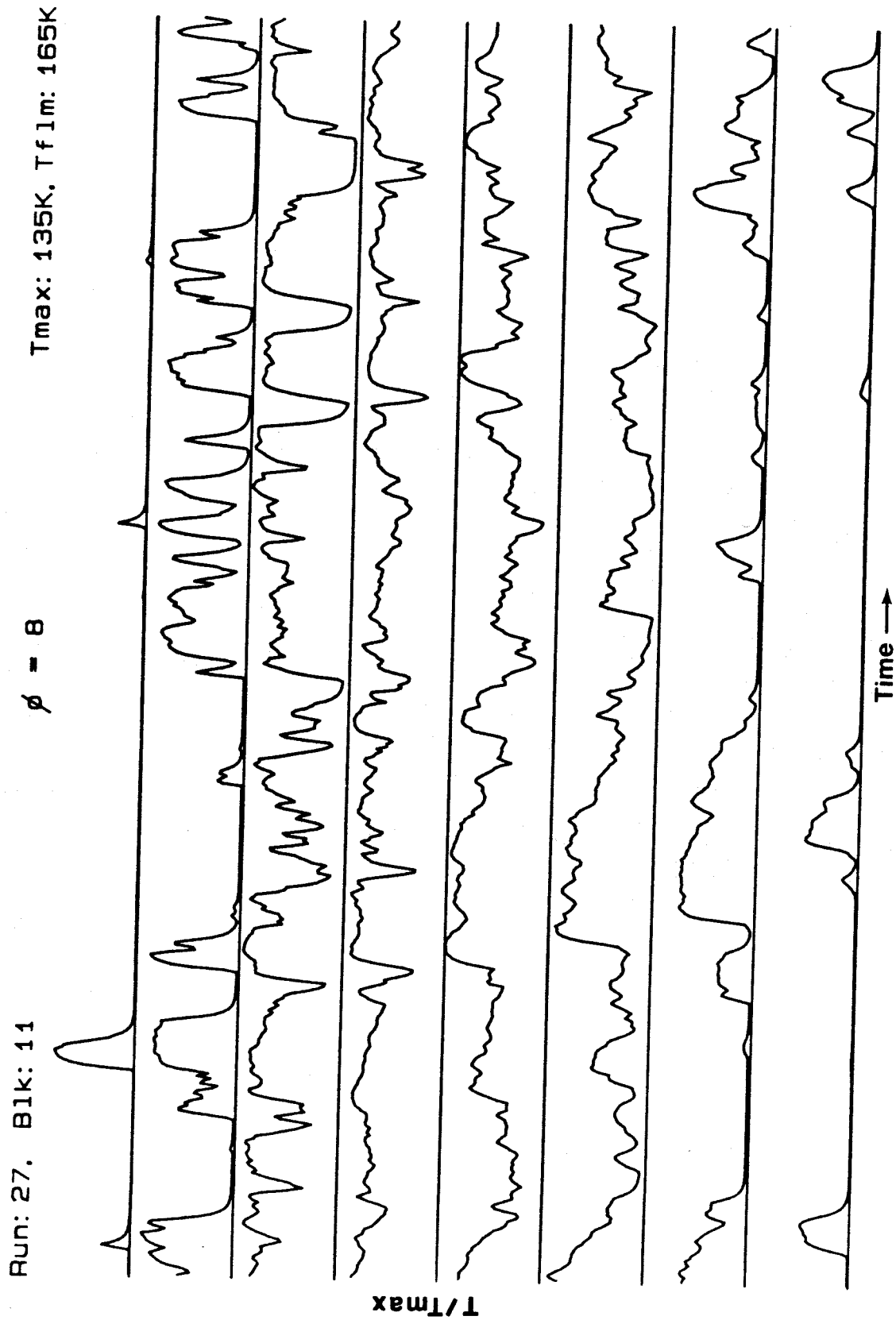

FIGURE 14a Temperature vs Time Trace, $\varphi = 8$, $r = 0.40$, $s = 1$, Run = 27. Flow from right to left, high speed on top. Time axis = 51.2 msec.

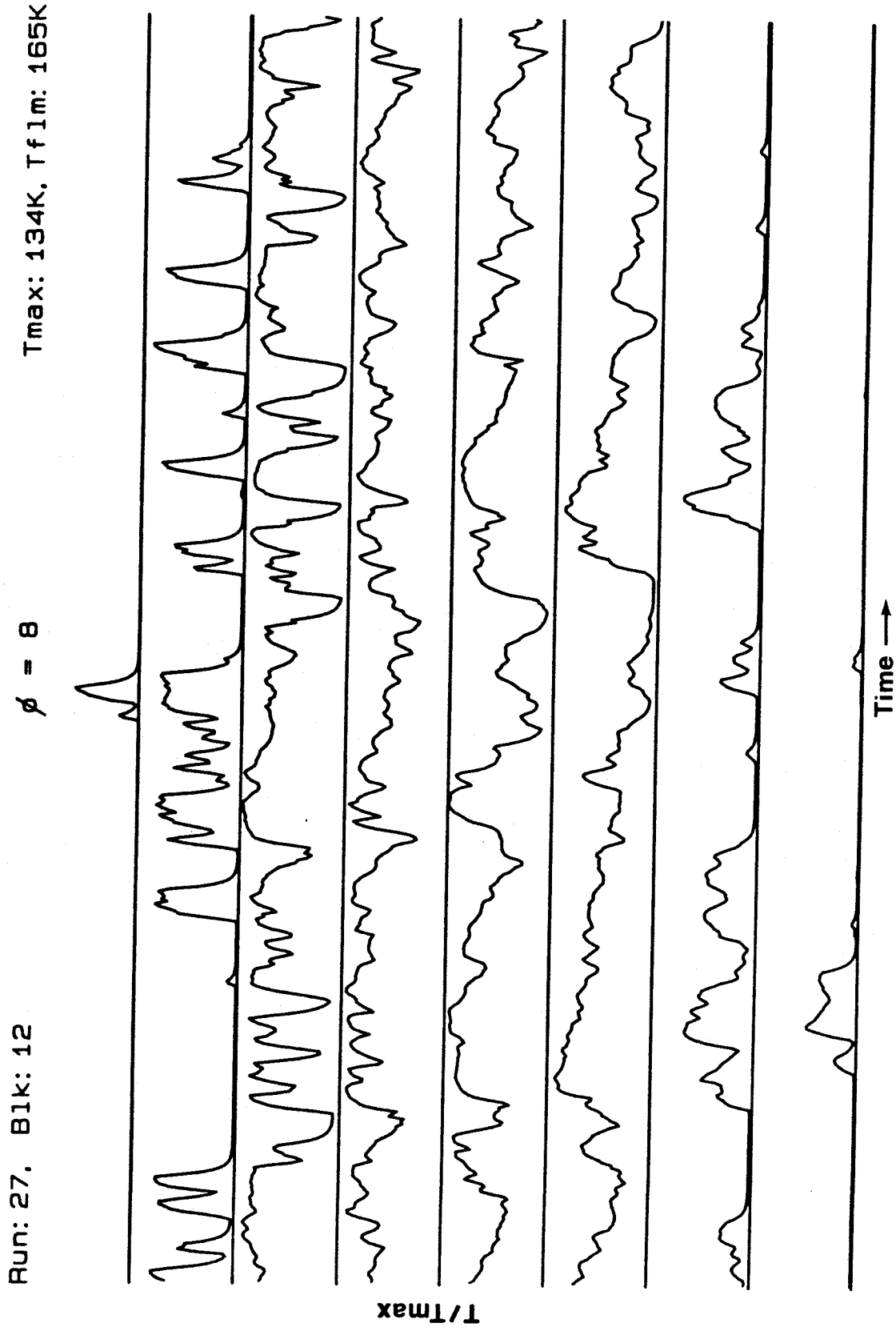

FIGURE 14b Temperature vs Time Trace, $\varphi = 8$, $r = 0.40$, $s = 1$, Run = 27.
Flow from right to left, high speed on top. Time axis = 51.2 msec.

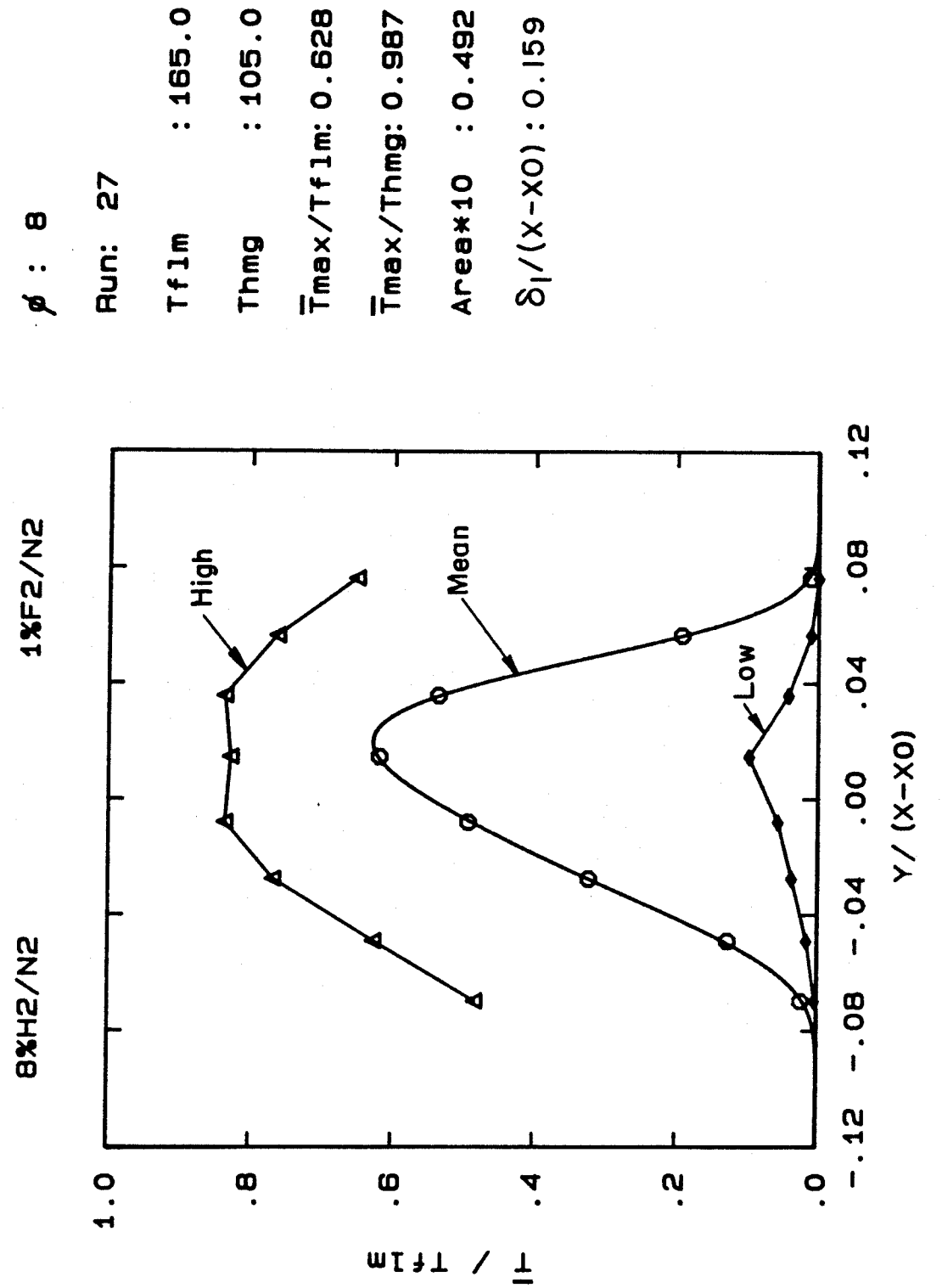

FIGURE 14c Mean Temperature Profile, $\varphi = 8$, $r = 0.40$, $s = 1$, Run = 27

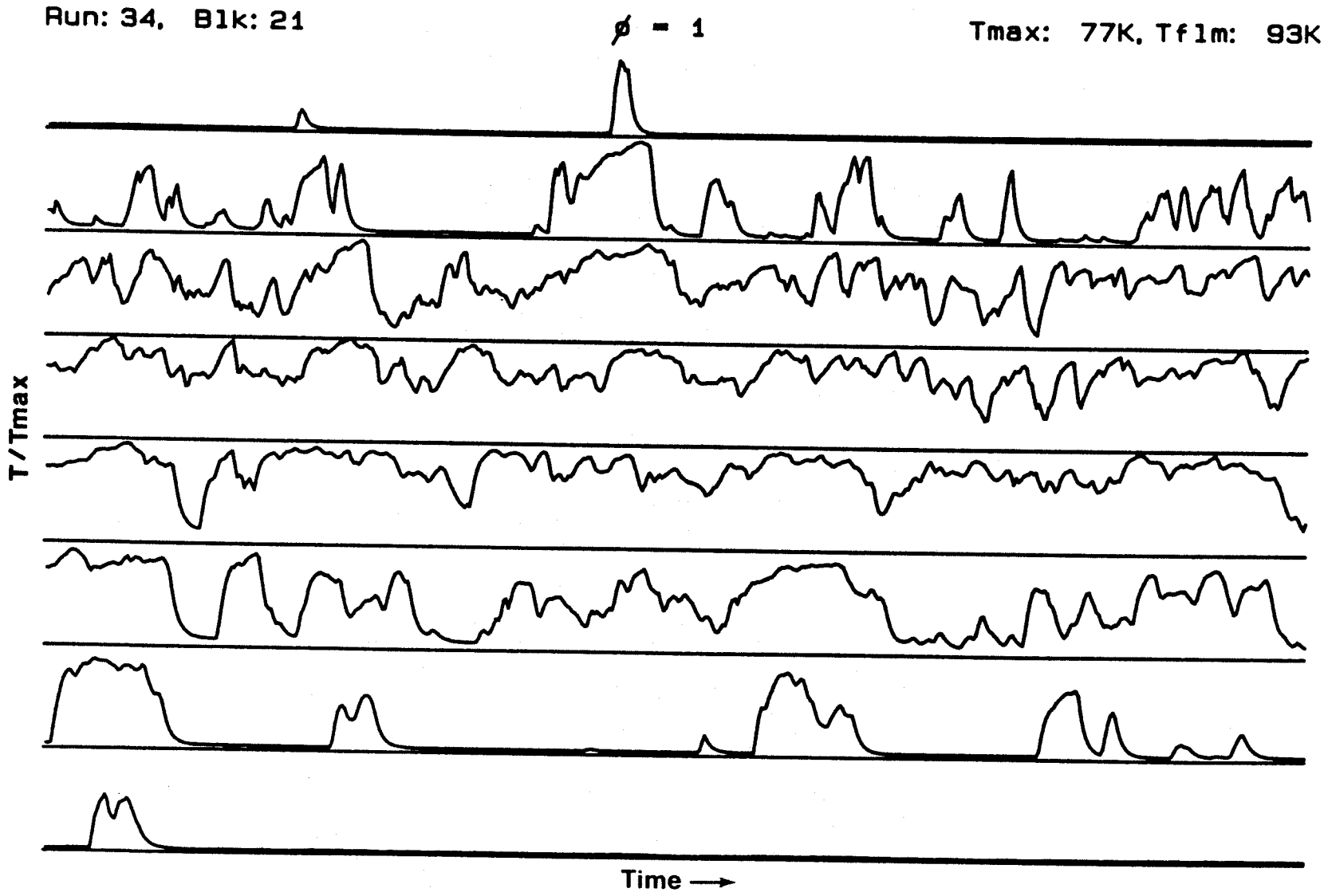

FIGURE 15a Temperature vs Time Trace, $\varphi = 1$, $r = 0.40$, $s = 1$, Run = 34. Flow from right to left, high speed on top. Time axis = 51.2 msec.

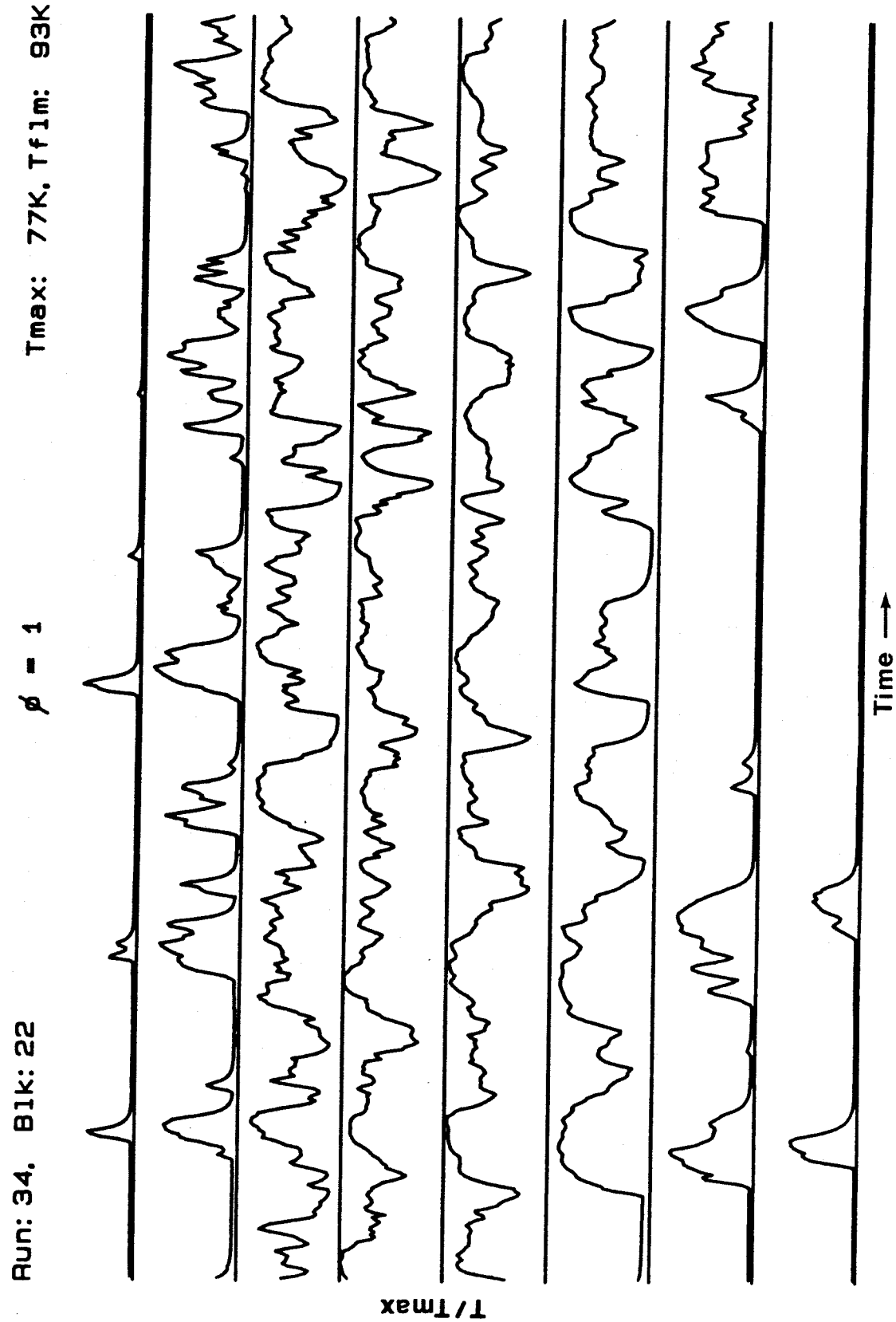

FIGURE 15b Temperature vs Time Trace, $\varphi = 1$, $r = 0.40$, $s = 1$, Run = 34.
Flow from right to left, high speed on top. Time axis = 51.2 msec.

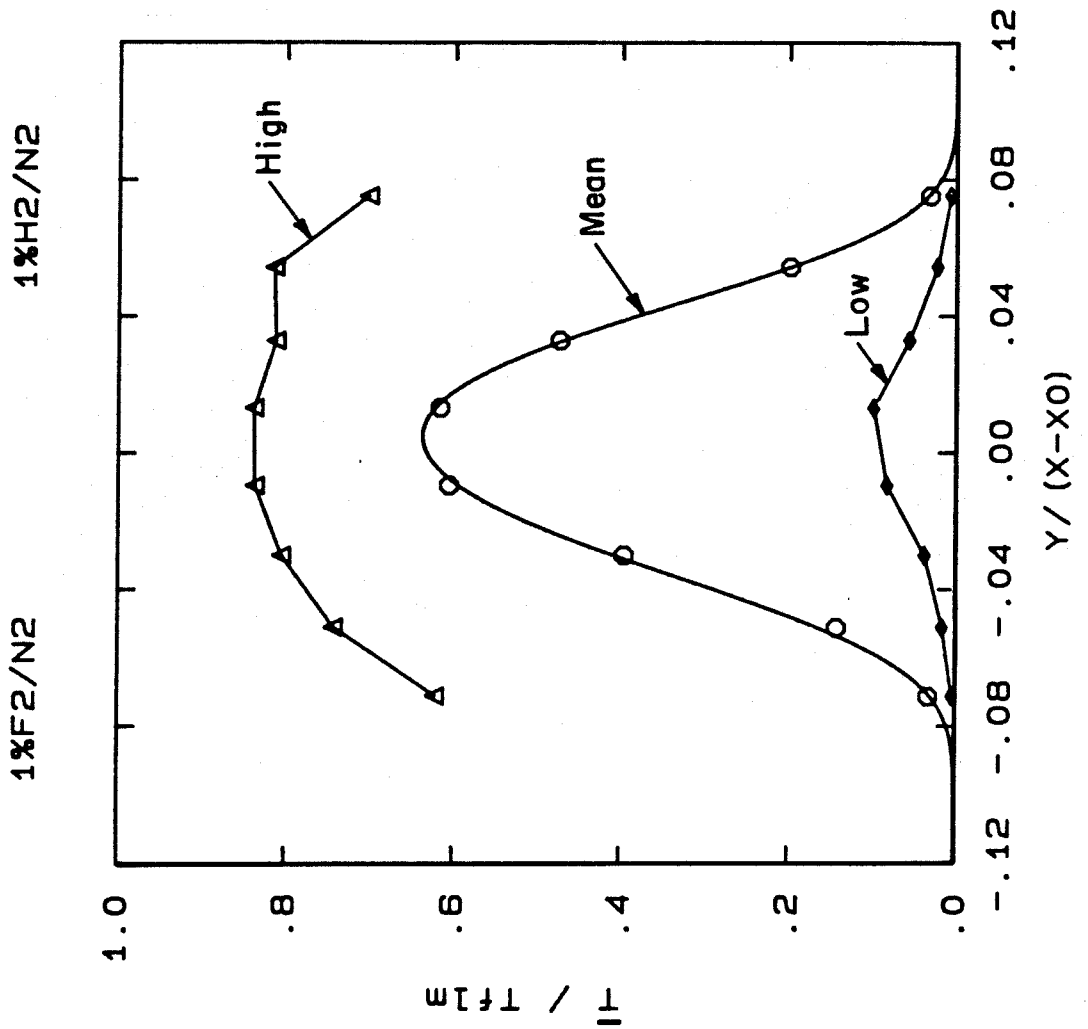

FIGURE 15c Mean Temperature Profile, $\varphi = 1, r = 0.40, s = 1$, Run = 34

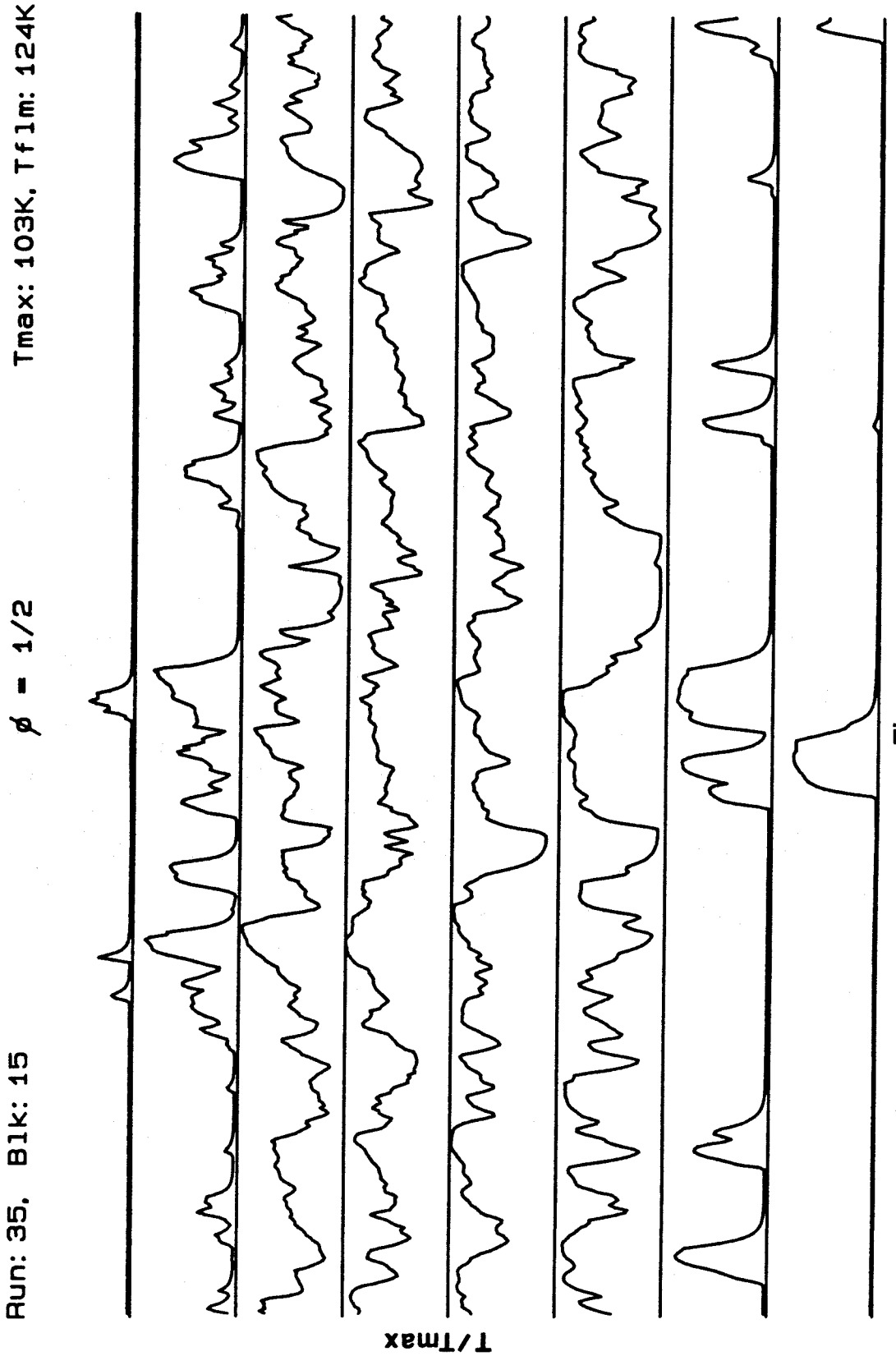

FIGURE 16a Temperature vs Time Trace, $\varphi = 1/2$, $r = 0.40$, $s = 1$, Run = 35.
Flow from right to left, high speed on top. Time axis = 51.2 msec.

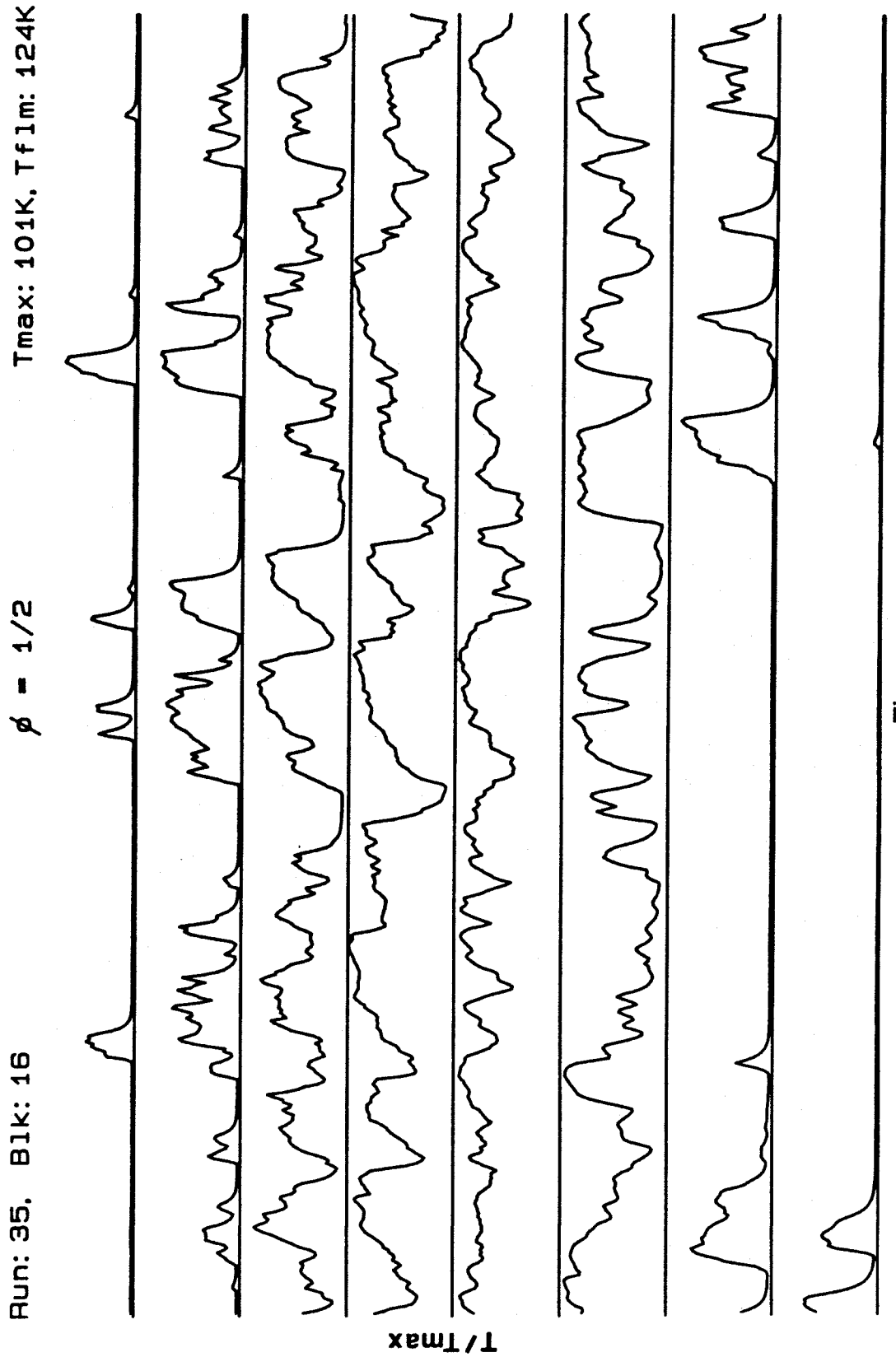

FIGURE 16b Temperature vs Time Trace, $\phi = 1/2$, $r = 0.40$, $s = 1$, Run = 35.
Flow from right to left, high speed on top. Time axis = 51.2 msec.

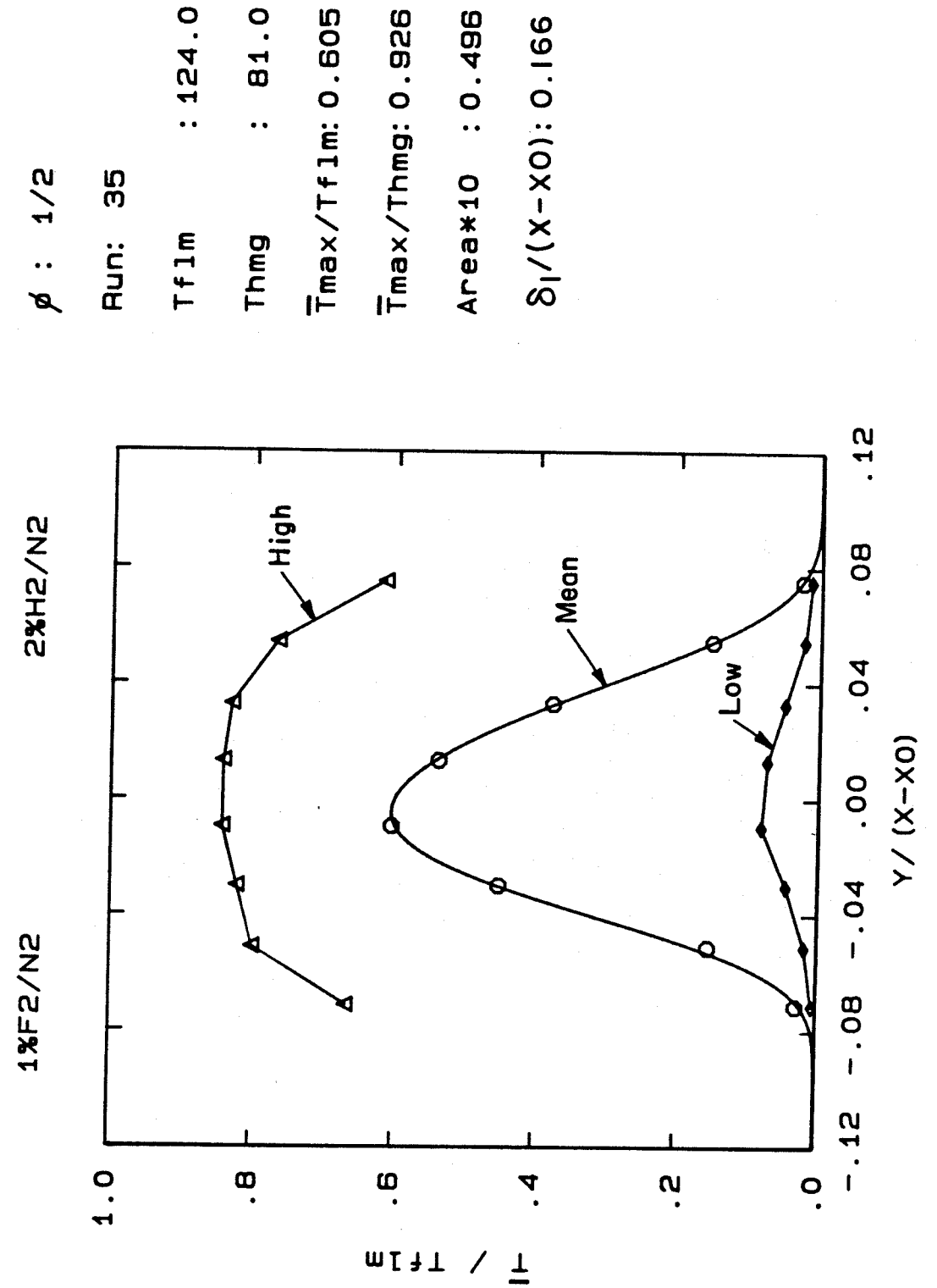

FIGURE 16c Mean Temperature Profile, $\varphi = 1/2$, $r = 0.40$, $s = 1$, Run = 35

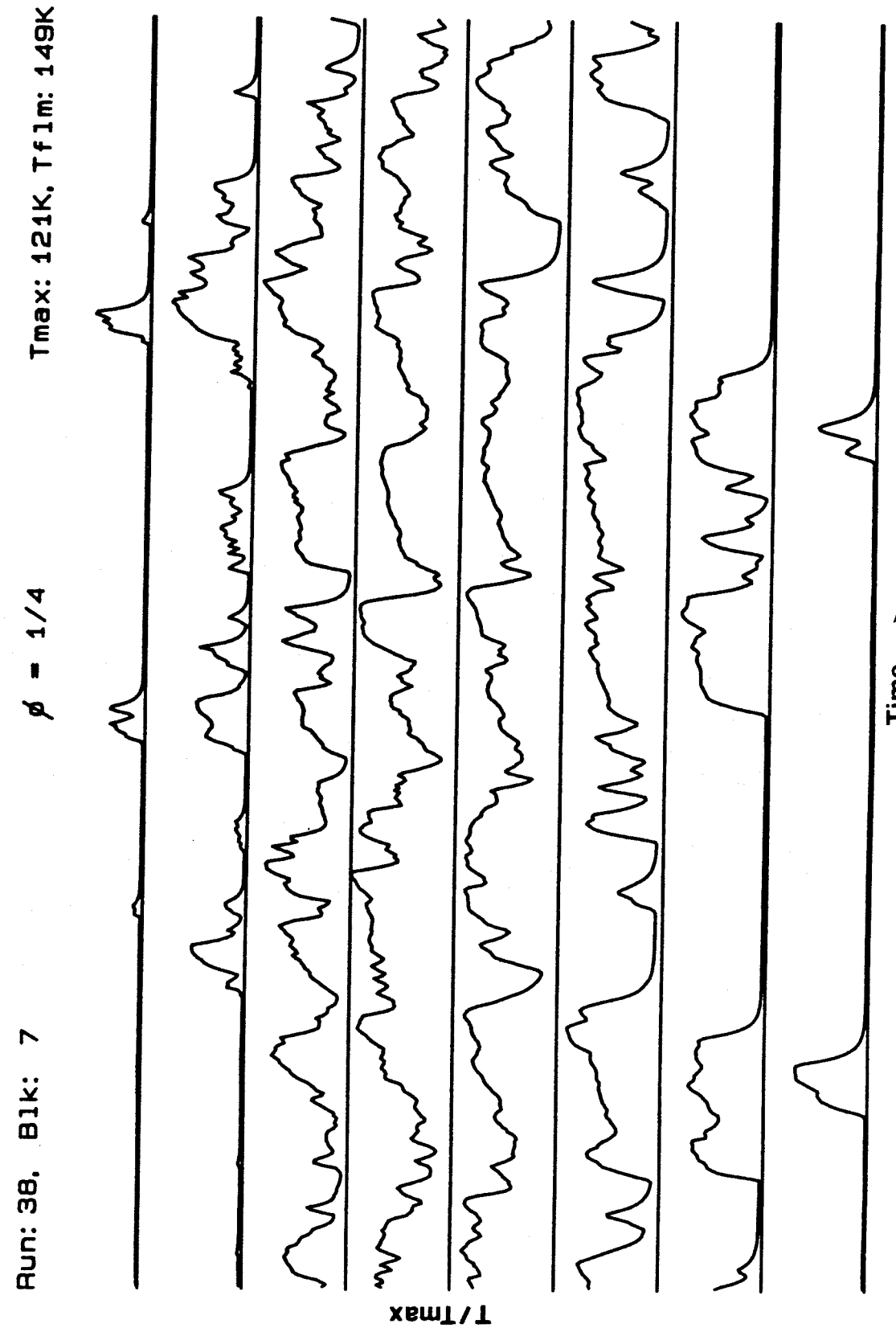

FIGURE 17a Temperature vs Time Trace, $\varphi = 1/4$, $r = 0.40$, $s = 1$, Run = 38. Flow from right to left, high speed on top. Time axis = 51.2 msec.

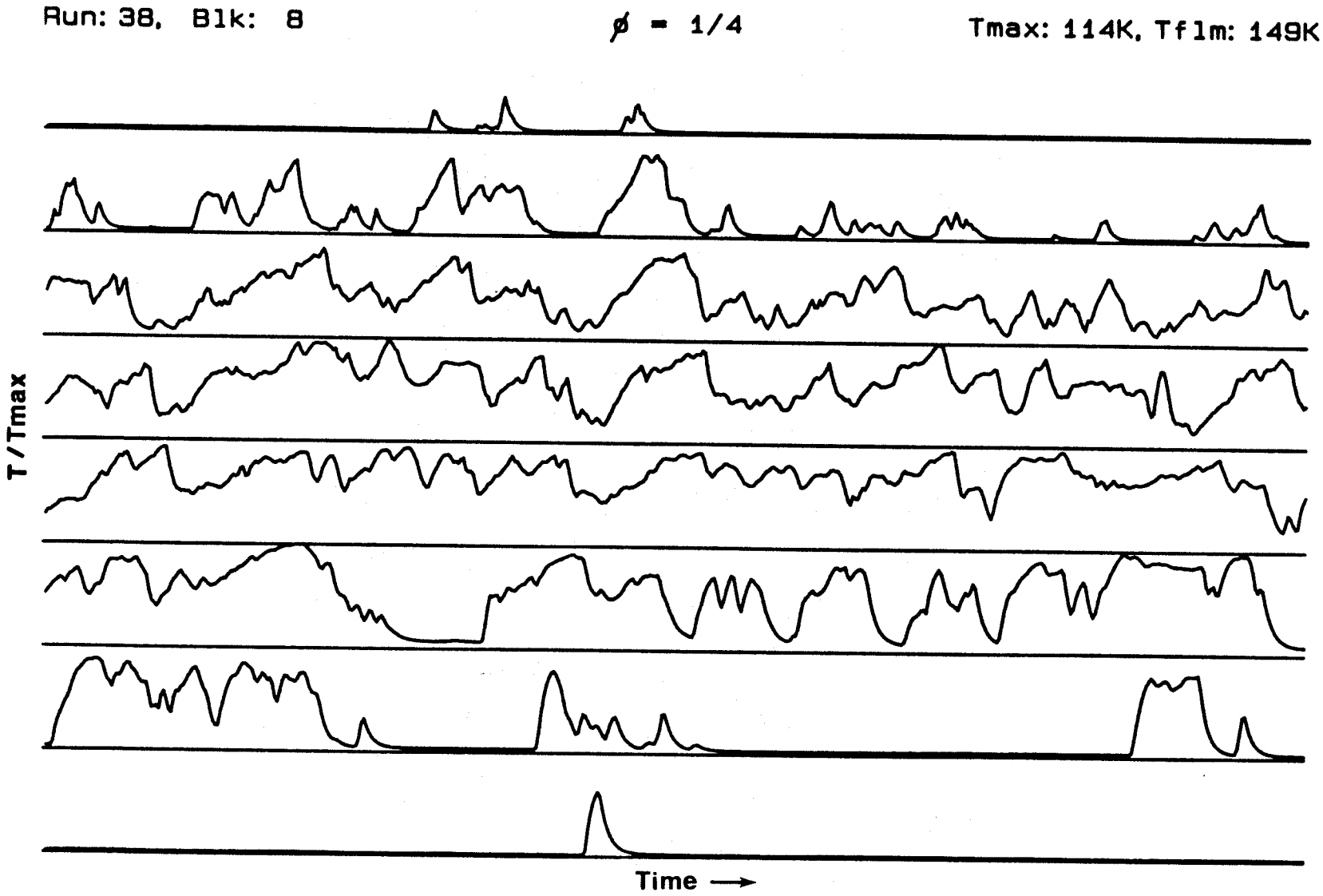

FIGURE 17b Temperature vs Time Trace, $\varphi = 1/4$, $r = 0.40$, $s = 1$, Run = 38. Flow from right to left, high speed on top. Time axis = 51.2 msec.

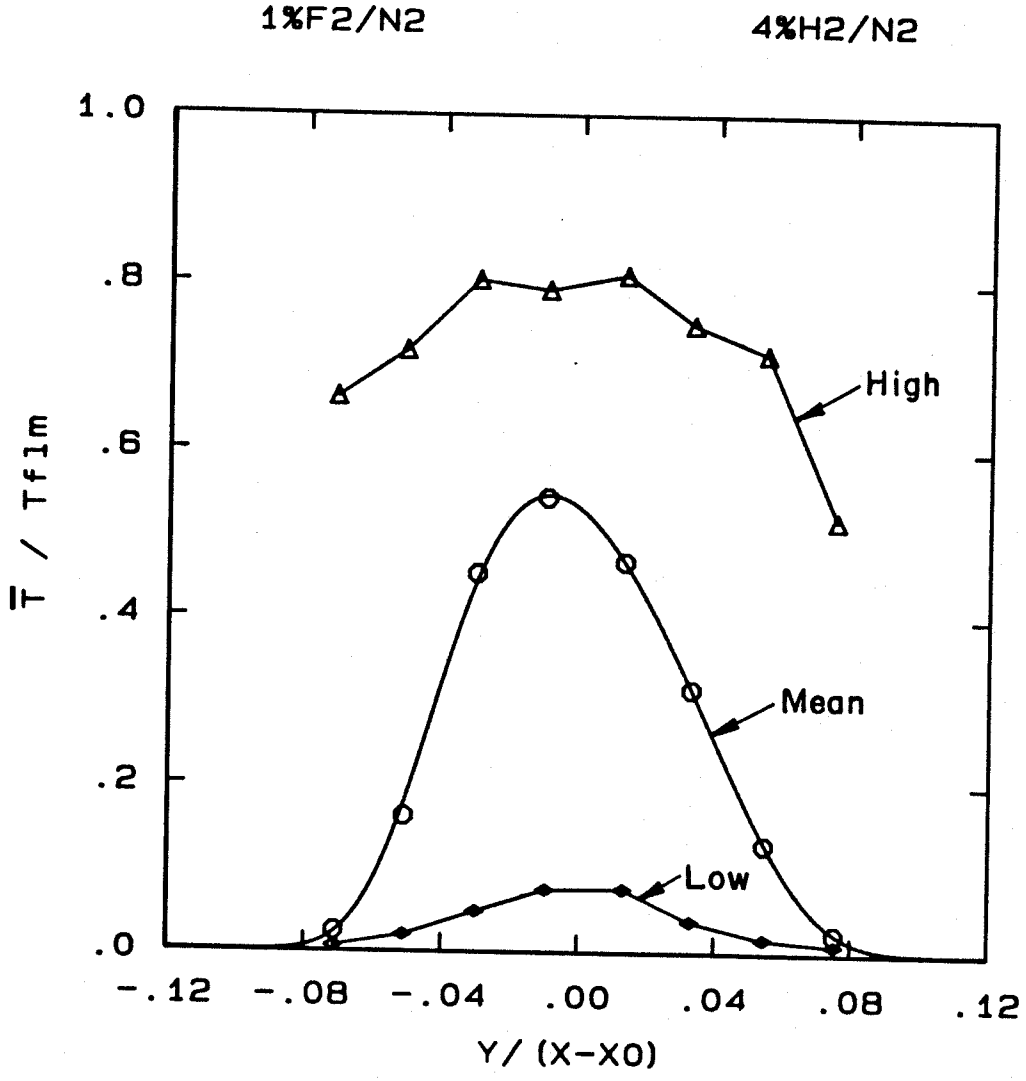

ϕ : 1/4

Run: 38

Tflm : 149.0

Thmg : 81.0

$\bar{T}$max/Tflm: 0.546

$\bar{T}$max/Thmg: 1.005

Area*10 : 0.449

$\delta_1/(X-XO)$: 0.166

FIGURE 17c Mean Temperature Profile, φ = 1/4, r = 0.40, s = 1, Run = 38

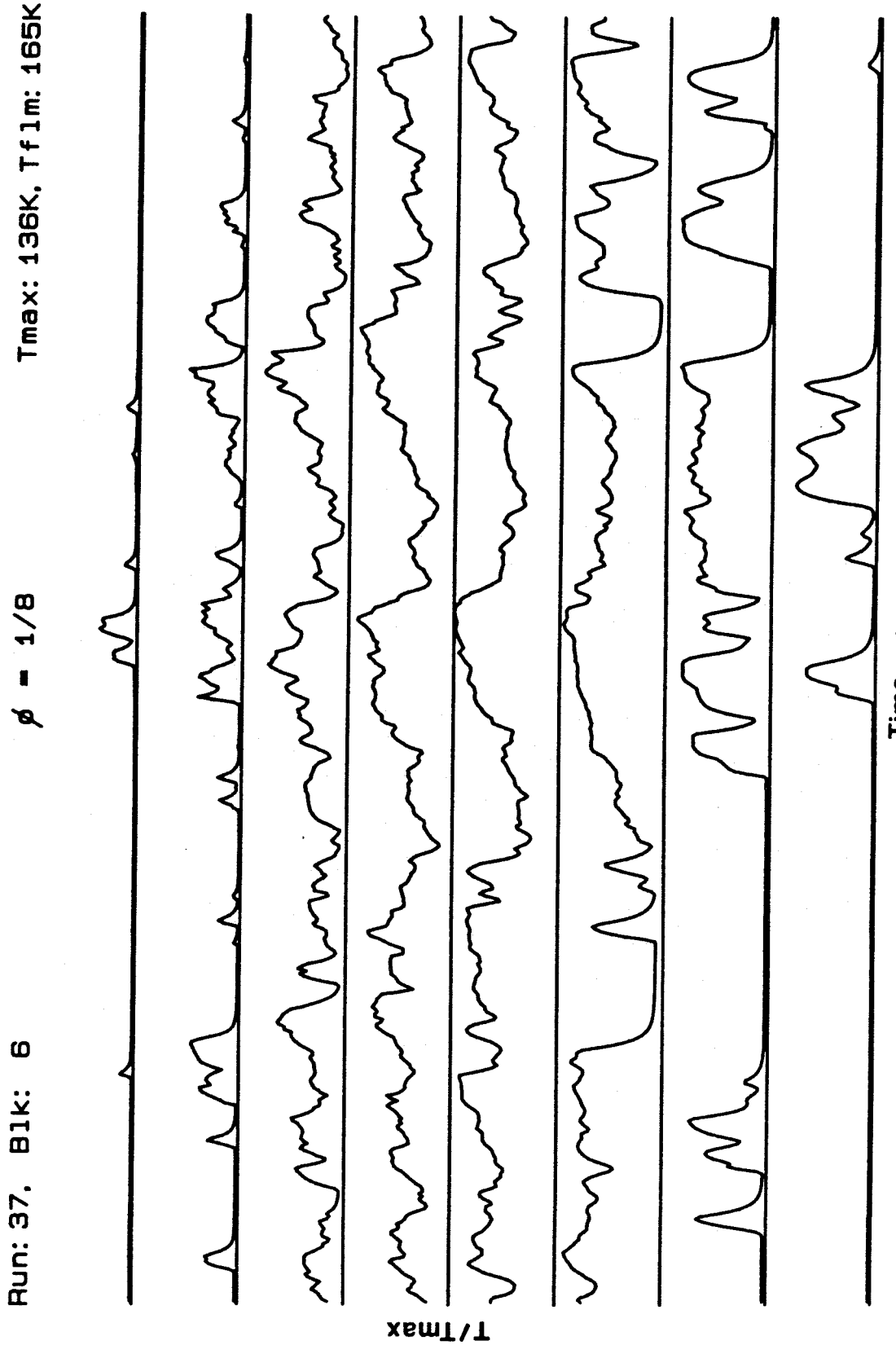

FIGURE 18a Temperature vs Time Trace, $\varphi = 1/8$, $r = 0.40$, $s = 1$, Run = 37.
Flow from right to left, high speed on top. Time axis = 51.2 msec.

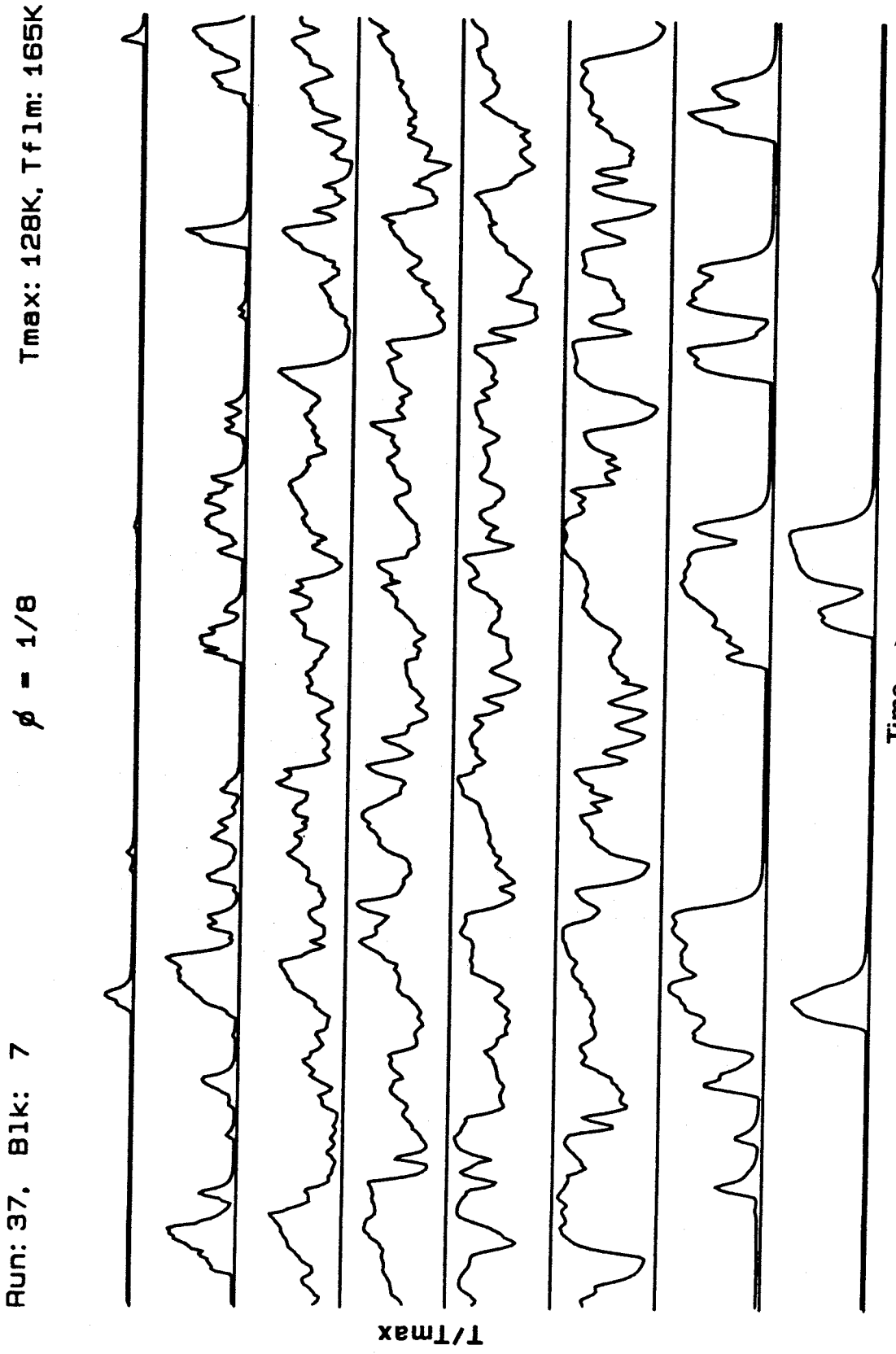

FIGURE 18b Temperature vs Time Trace, $\varphi = 1/8$, $r = 0.40$, $s = 1$, Run = 37.
Flow from right to left, high speed on top. Time axis = 51.2 msec.

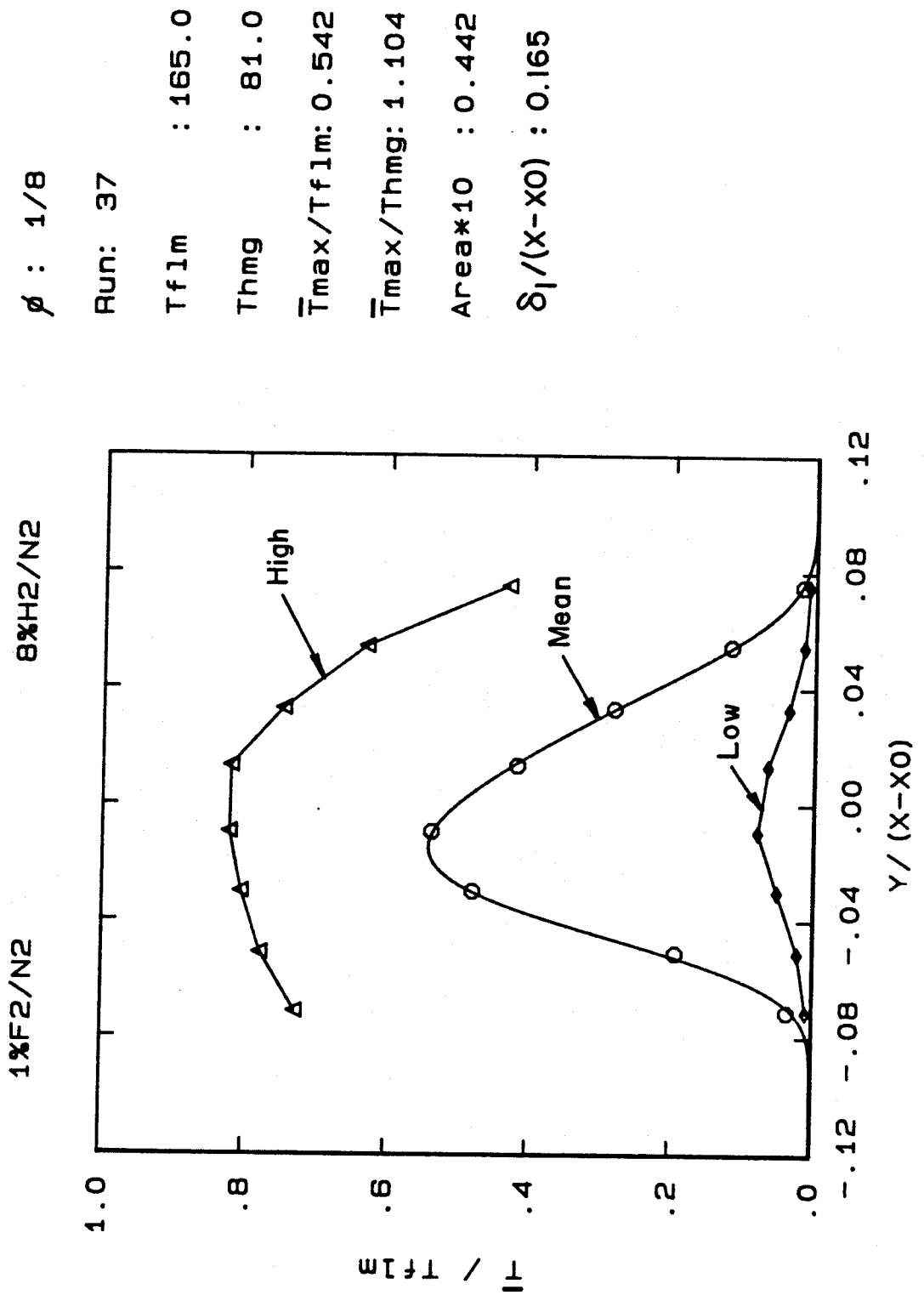

FIGURE 18c Mean Temperature Profile, $\varphi = 1/8$, $r = 0.40$, $s = 1$, Run = 37

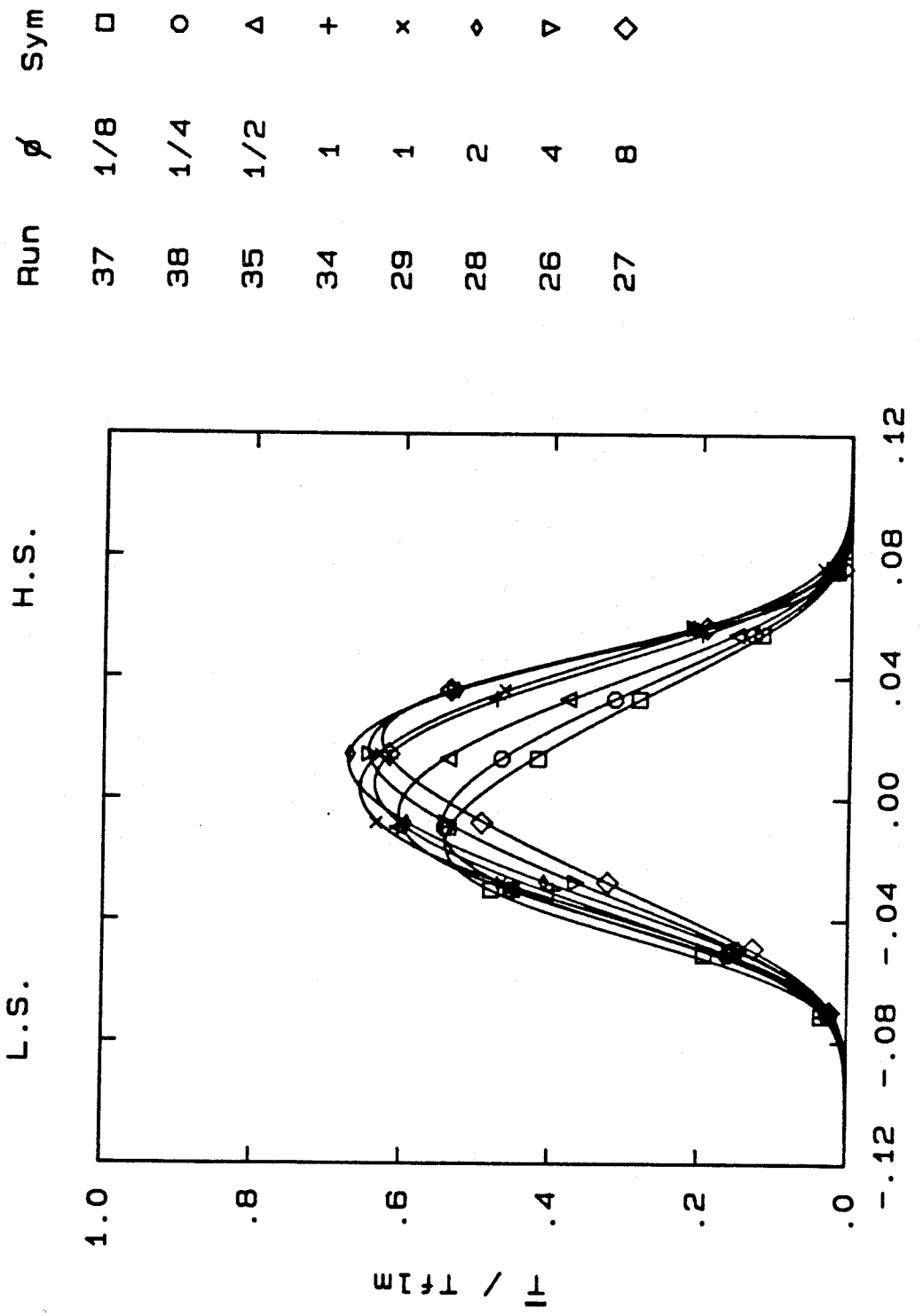

FIGURE 19 Normalized Mean Temperature Profiles, all φ.

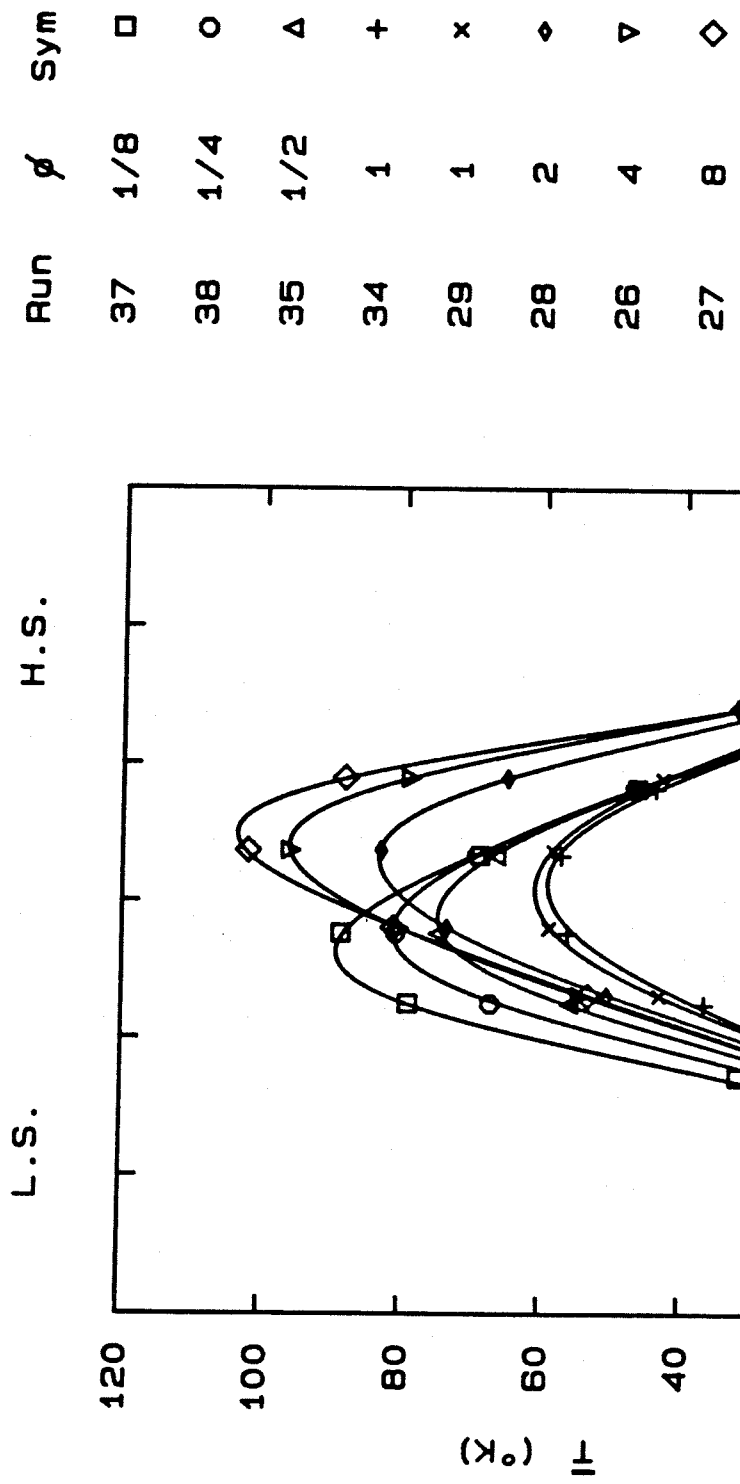

FIGURE 20 Actual Mean Temperature Profiles, all ϕ.

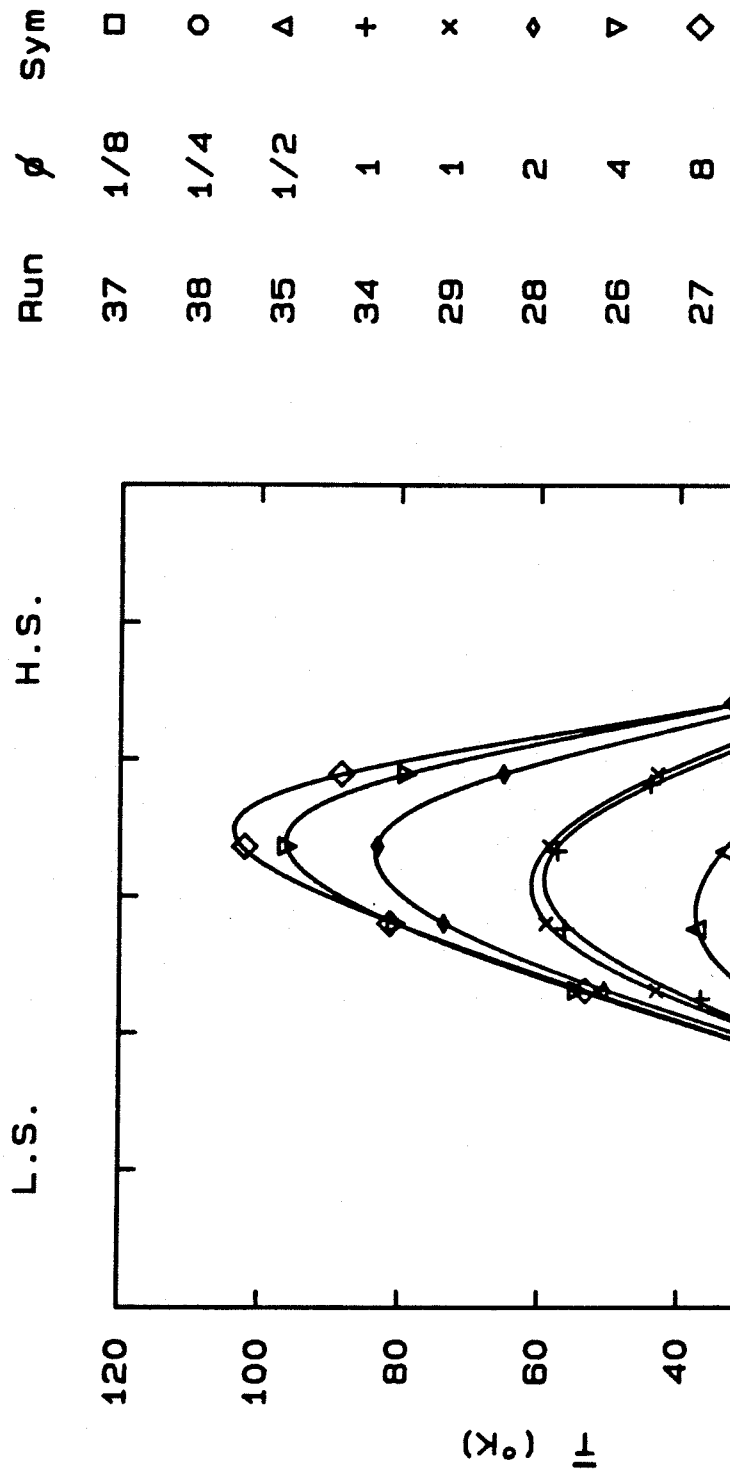

FIGURE 21a Inferred Mean Temperature Profiles for $c_{H.S.}$ = 1%, all φ.

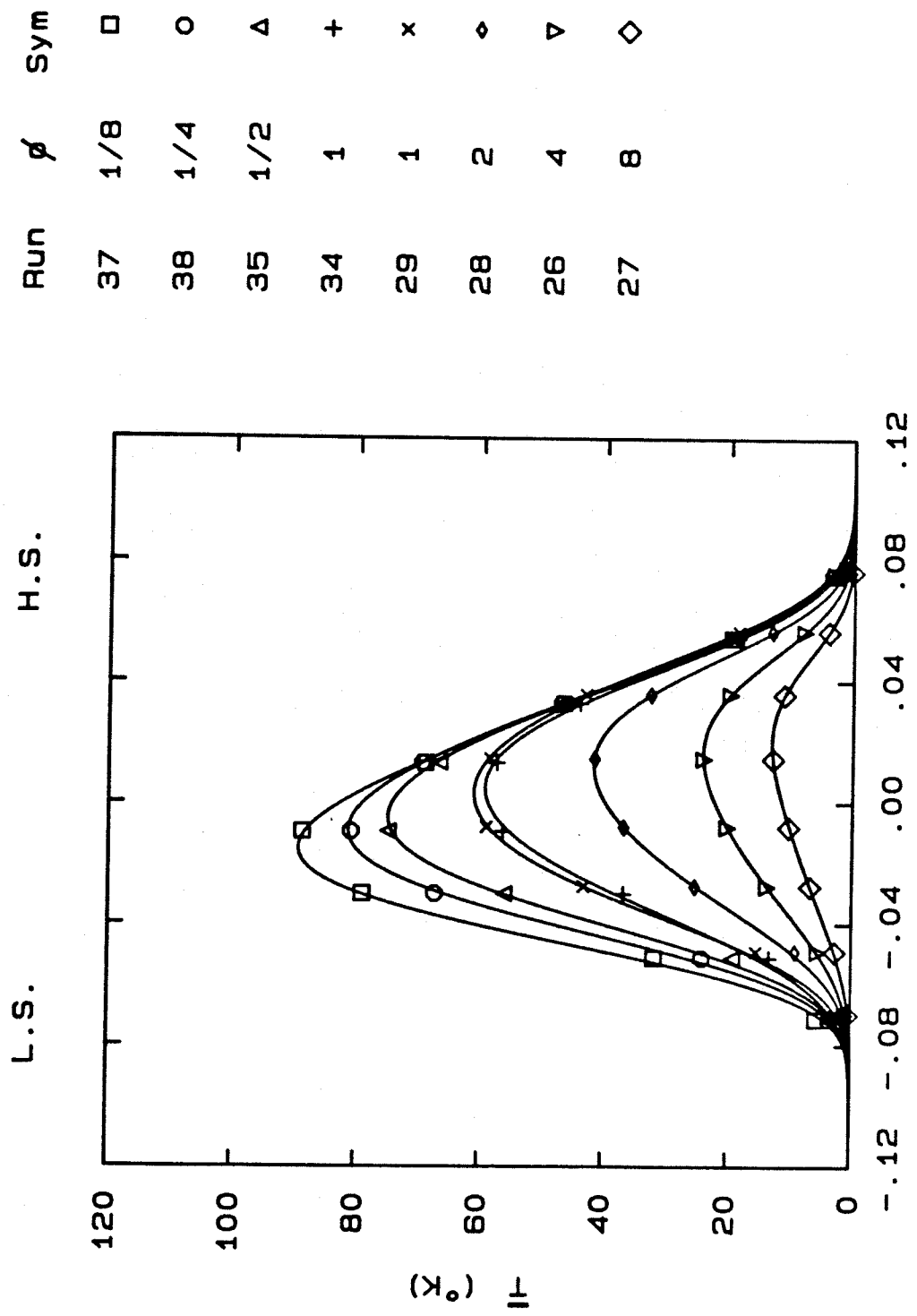

FIGURE 21b Inferred Mean Temperature Profiles for $c_{L.S.}$ = 1%, all φ.

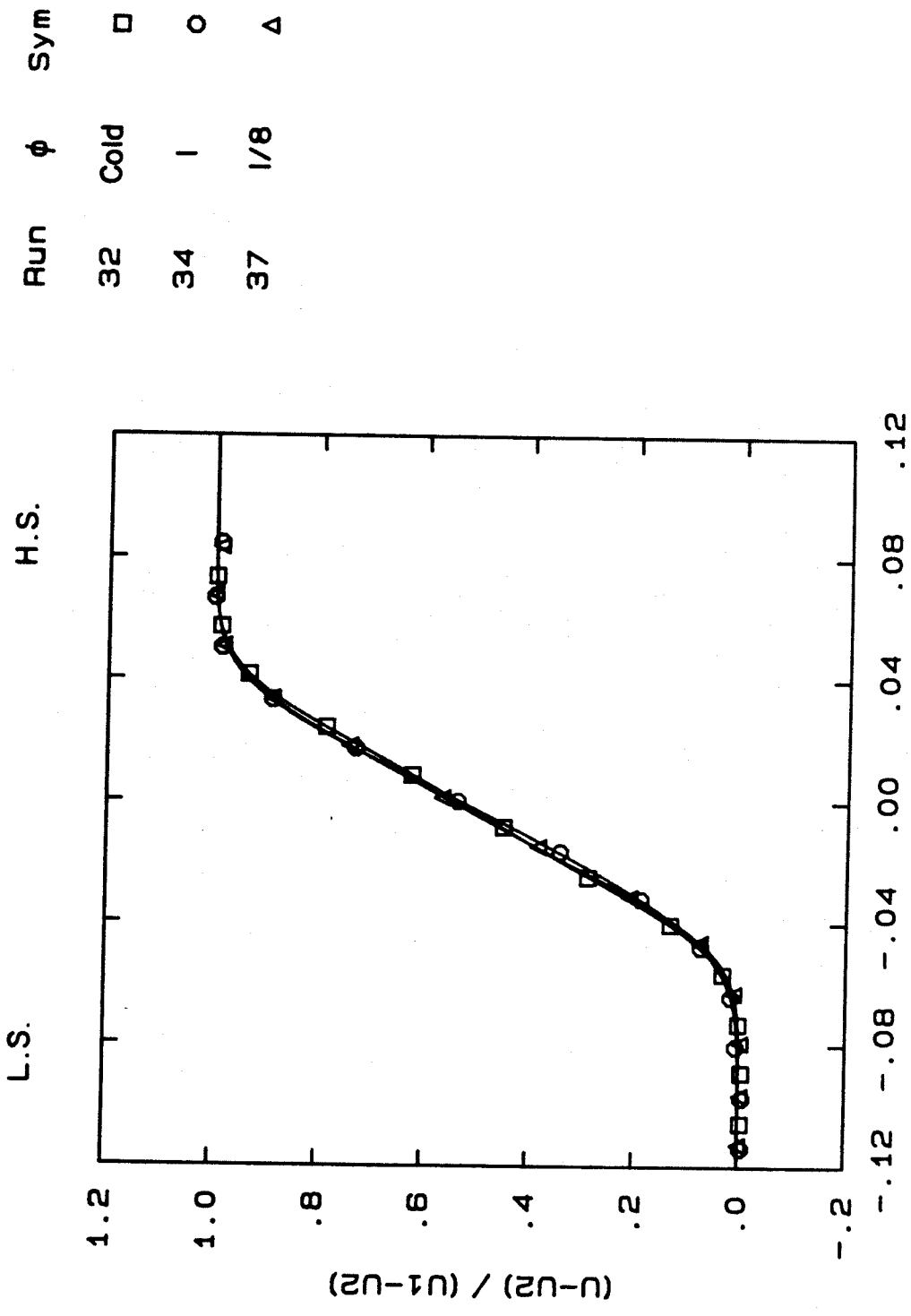

FIGURE 22 Mean Velocity Profiles

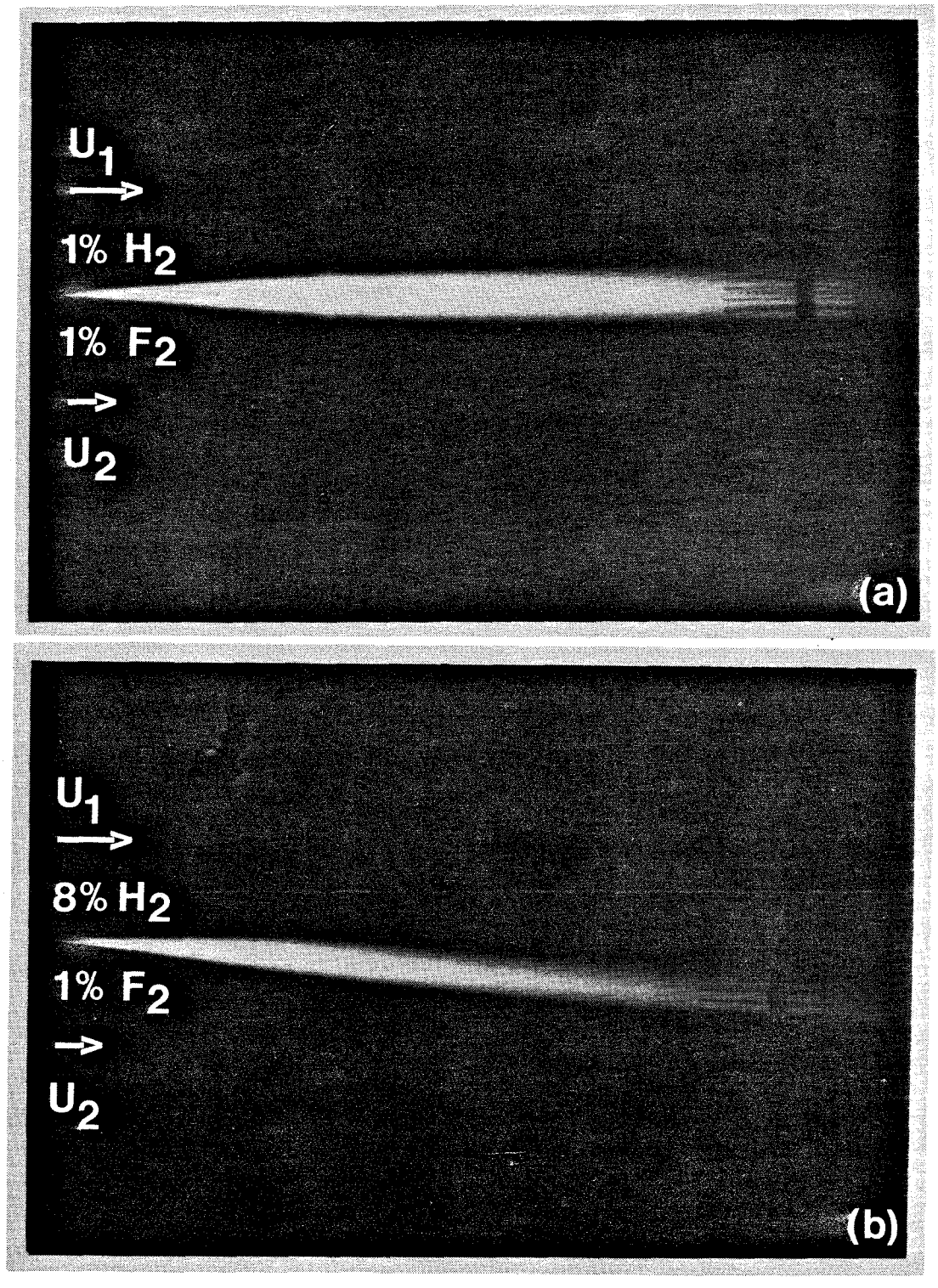

FIGURE 23 Time-Exposed Photographs of Mixing Layer
(a) $\varphi = 1$, Run 34 (b) $\varphi = 1/8$, Run 37

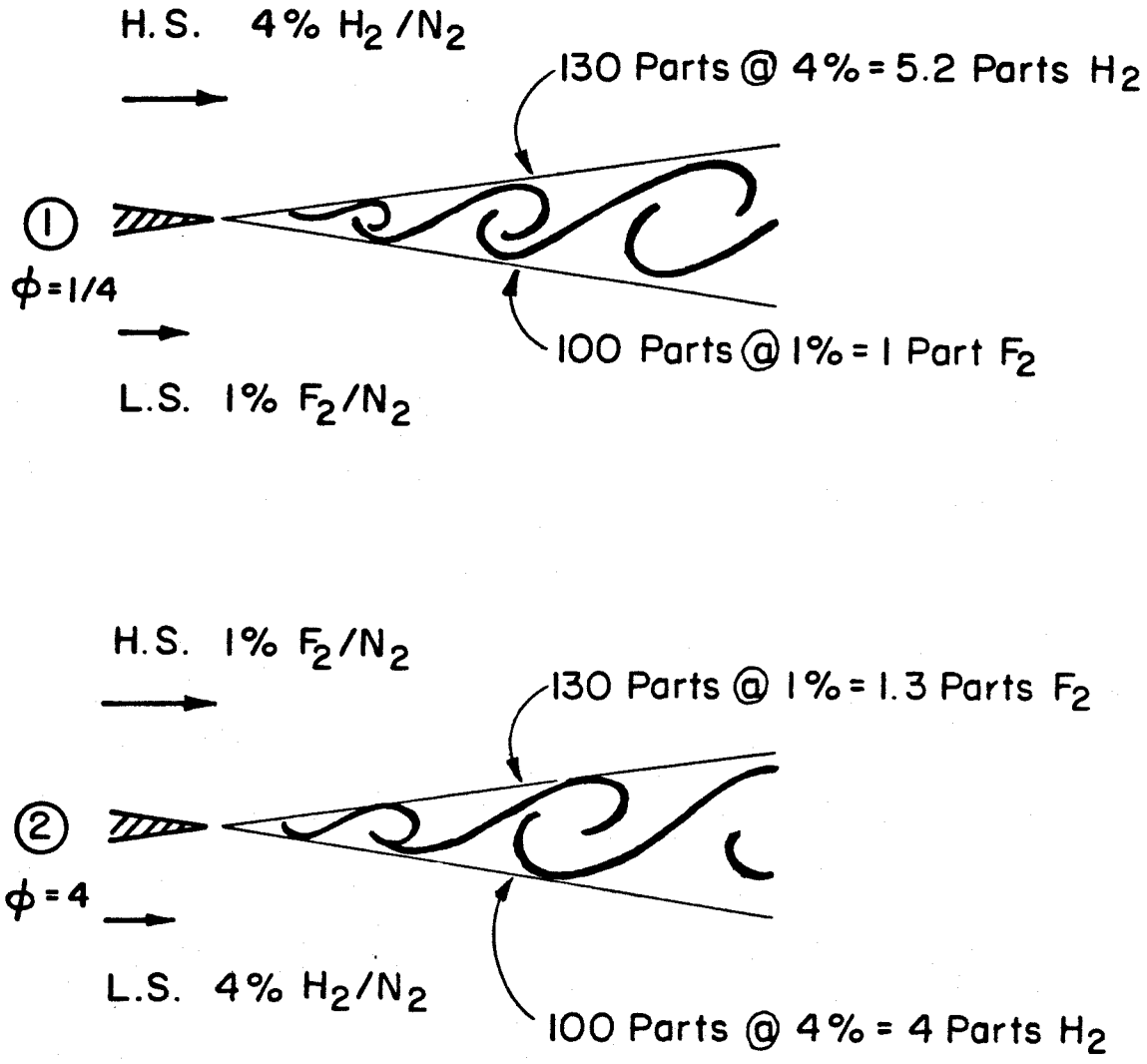

Homogeneous temperature 30% greater for case ② than for case ①

Flame sheet contribution same for cases ① , ②

FIGURE 24 Broadwell-Breidenthal View of Mixing Layer

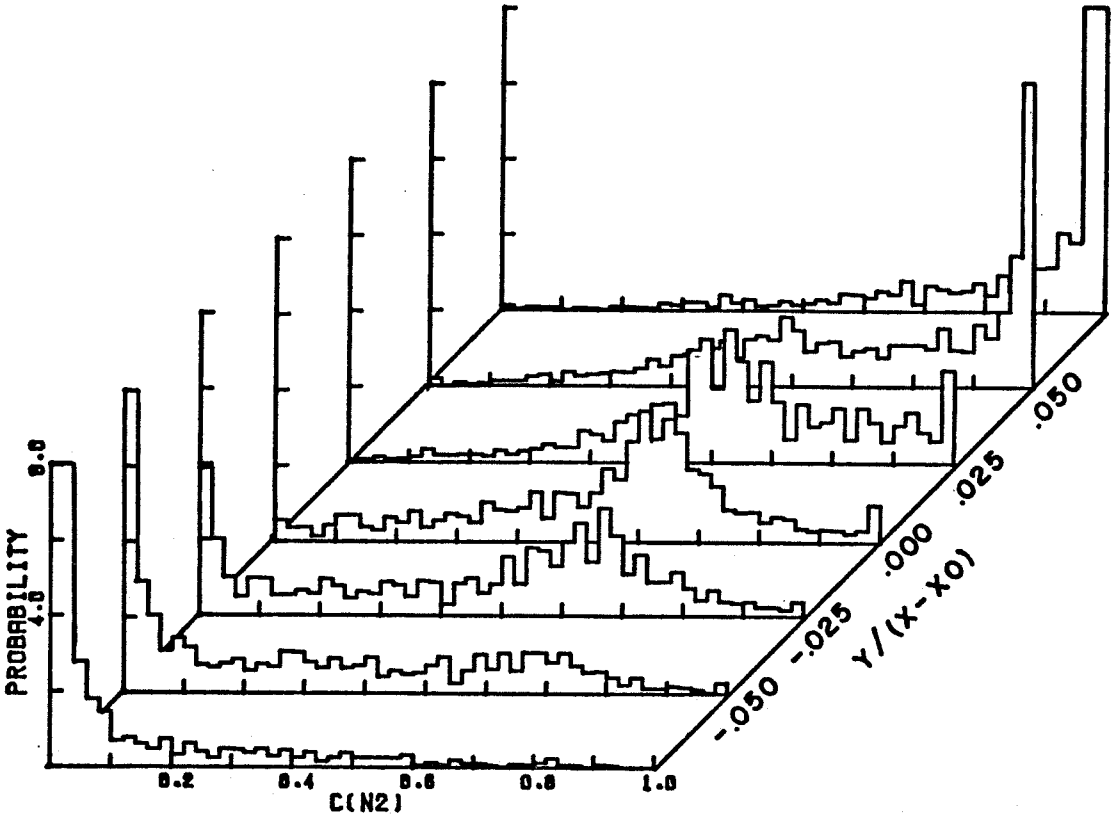

(a)

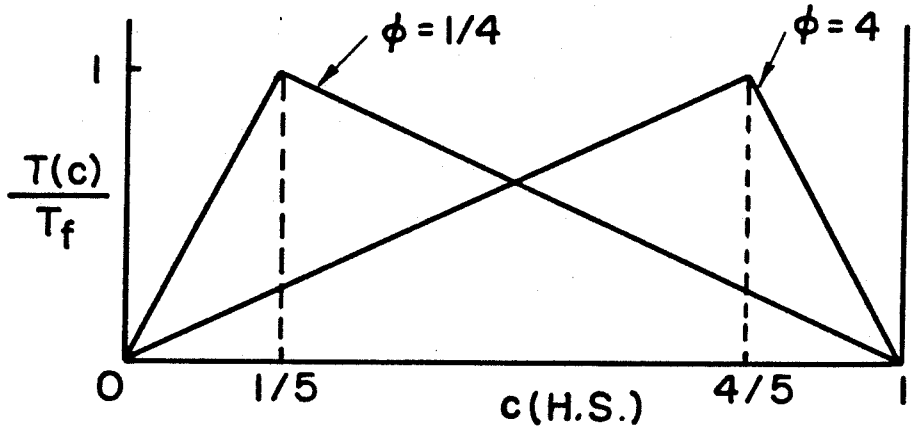

(b)

$$\overline{T} = \int_0^1 T(c)\,p(c)\,dc$$

FIGURE 25 (a) Konrad's *PDF* (b) Computation of Mean Temperature from *PDF*

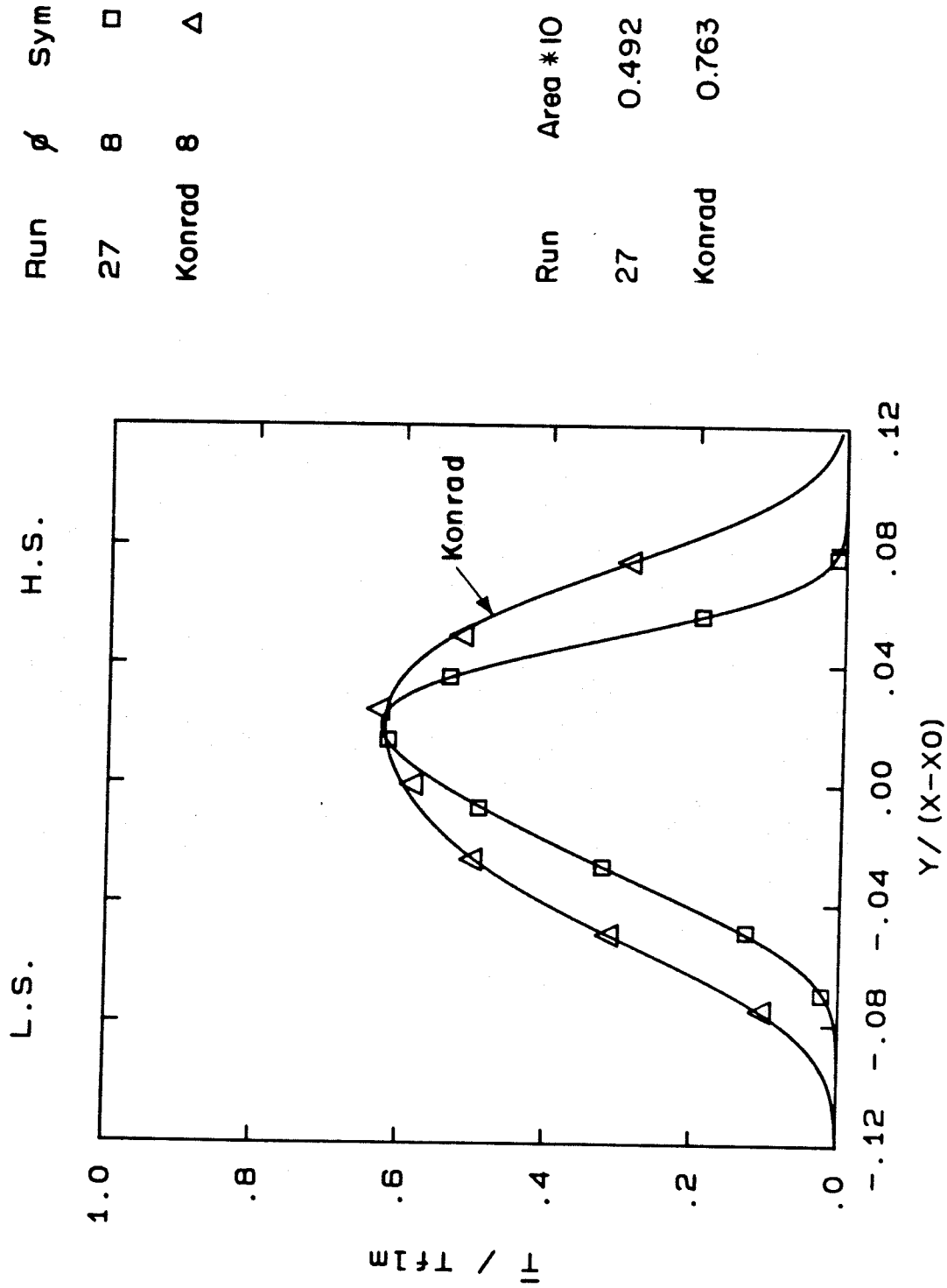

FIGURE 26a Comparison with Konrad, $\varphi = 8$

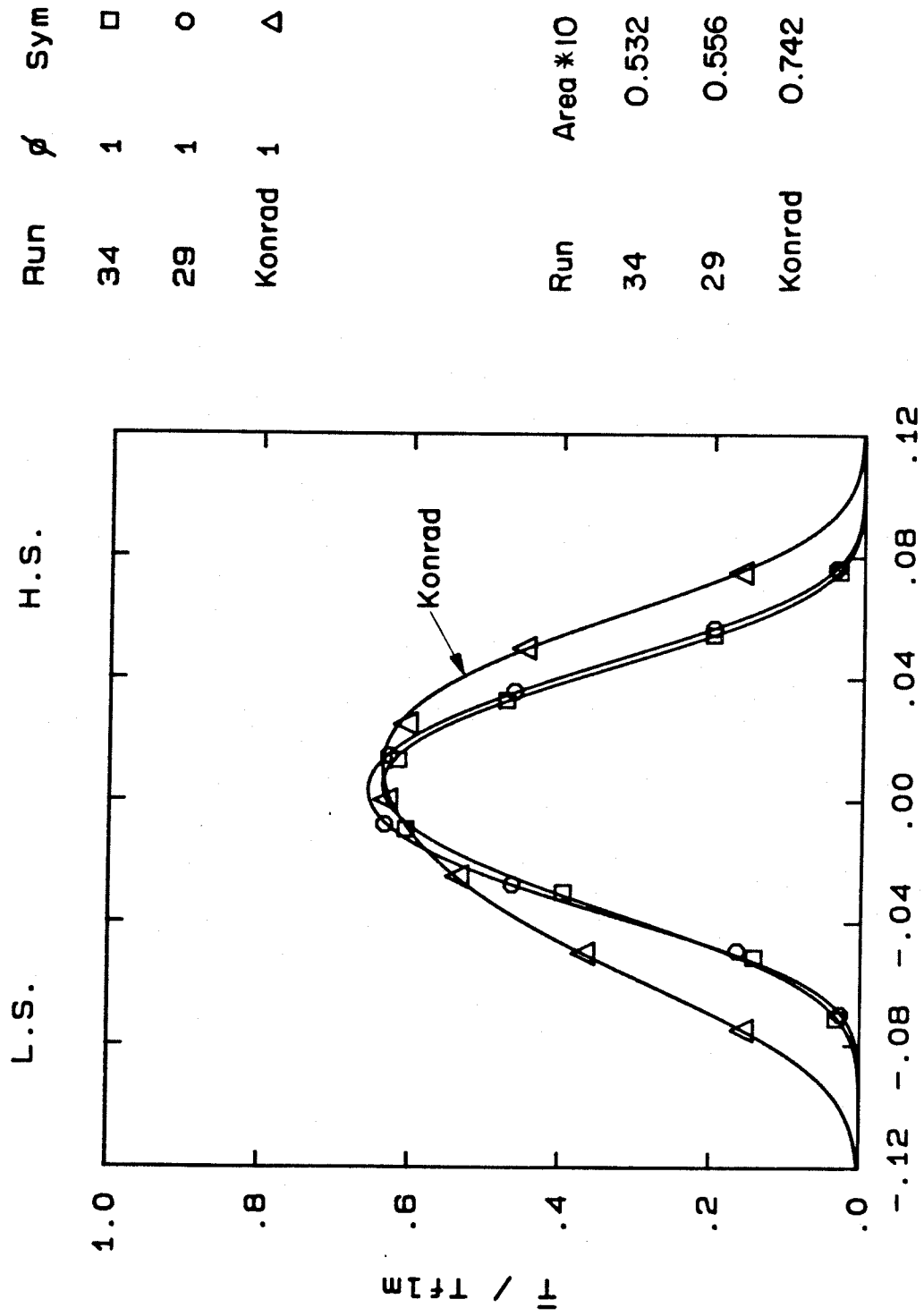

FIGURE 26b Comparison with Konrad, $\varphi = 1$

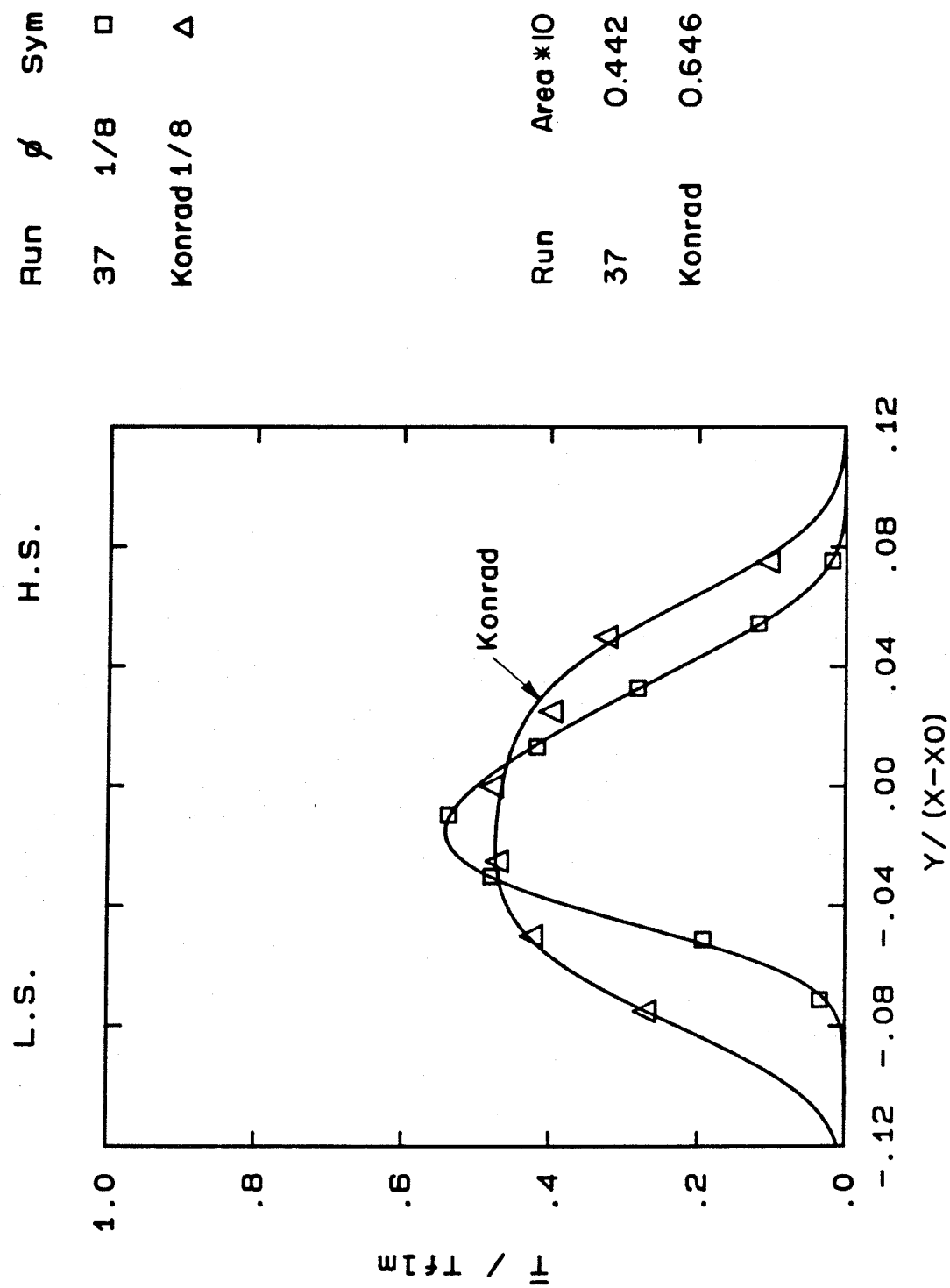

FIGURE 26c Comparison with Konrad, $\varphi = 1/8$

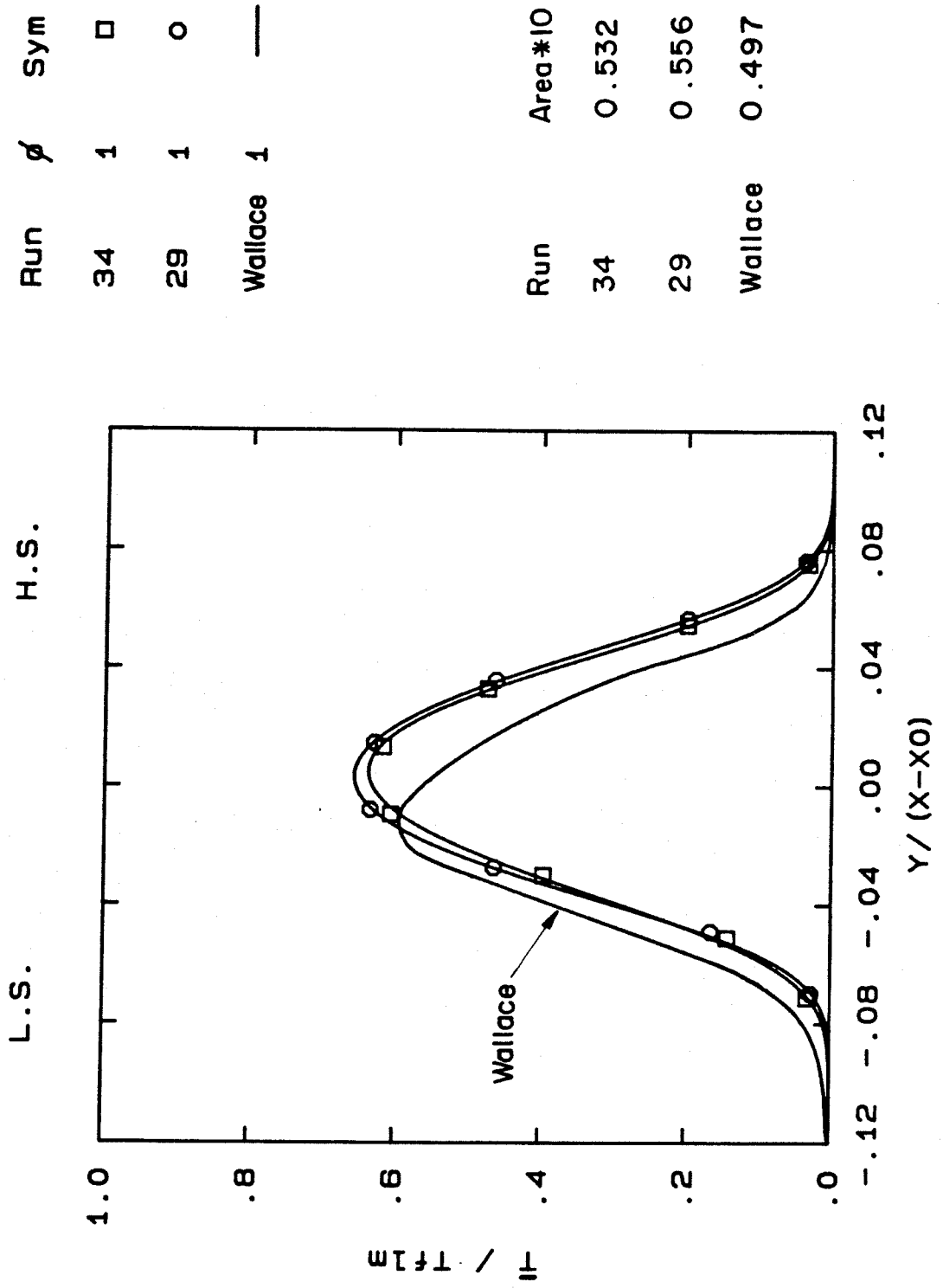

FIGURE 27 Comparison with Wallace, $\varphi = 1$

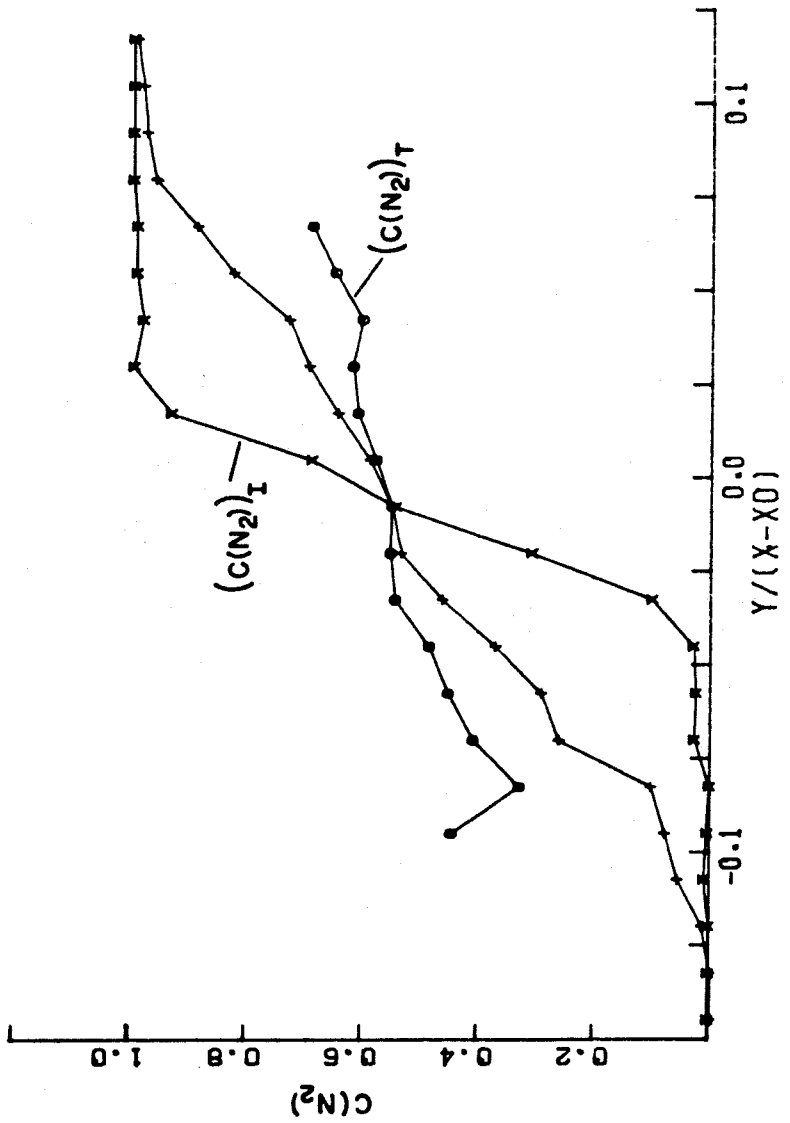

FIGURE 28 Konrad's Mean Mixed Concentration in Mixing Layer

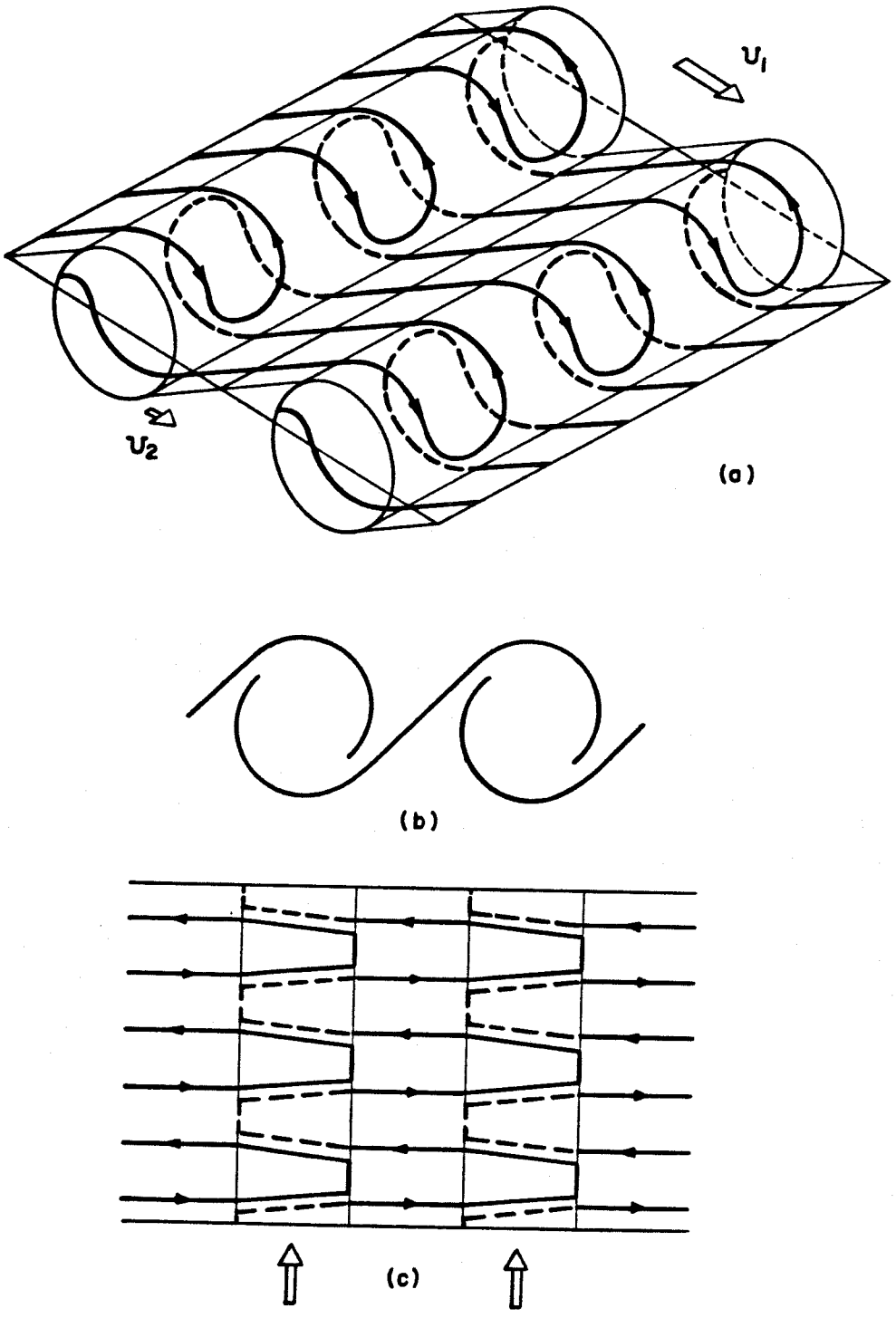

FIGURE 29 Bernal View of Vortex Structure in Mixing Layer
(a) Isometric View (b) Side View (c) Plan View

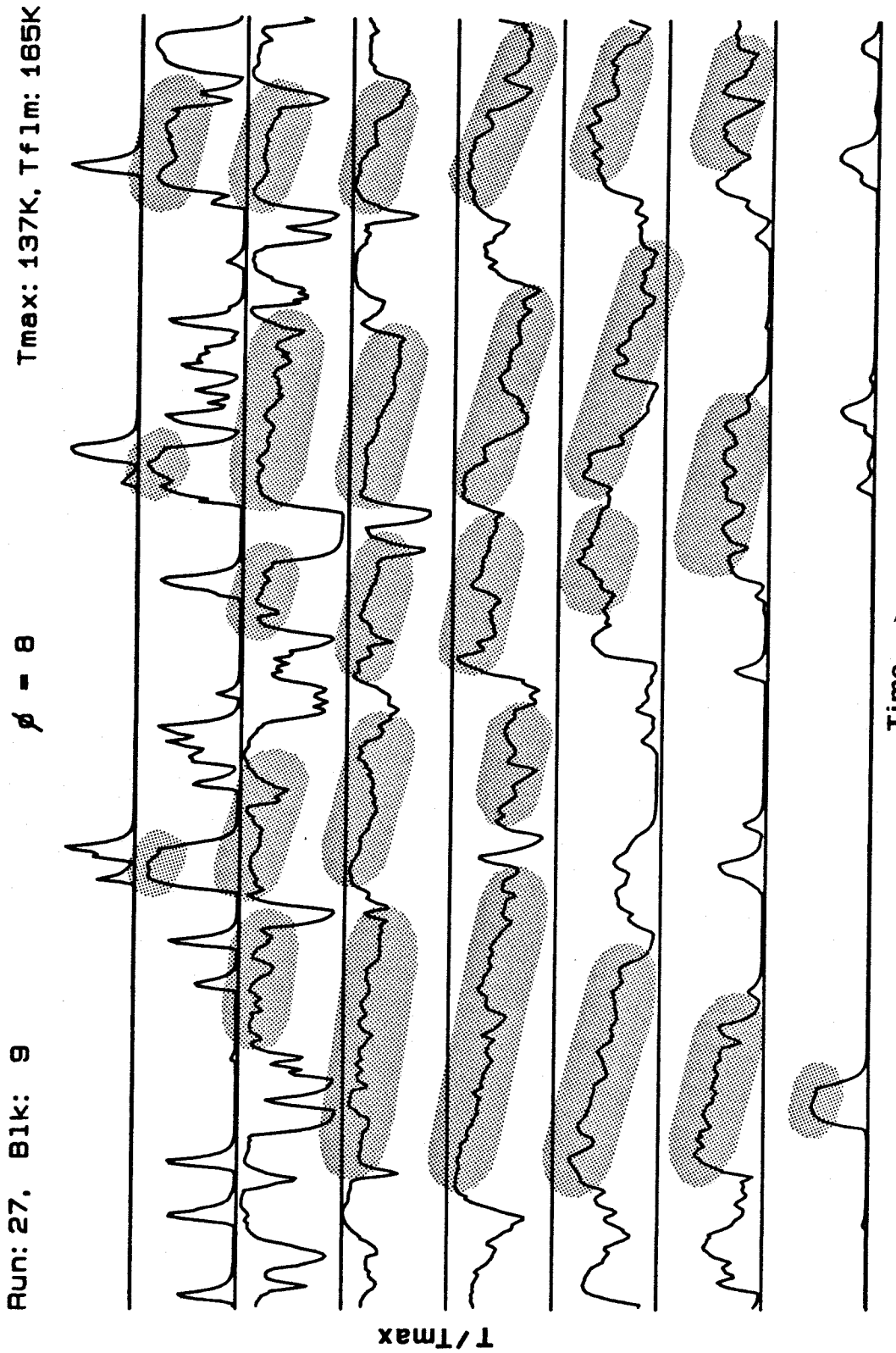

FIGURE 30a Temperature vs Time Trace, $\varphi = 8$

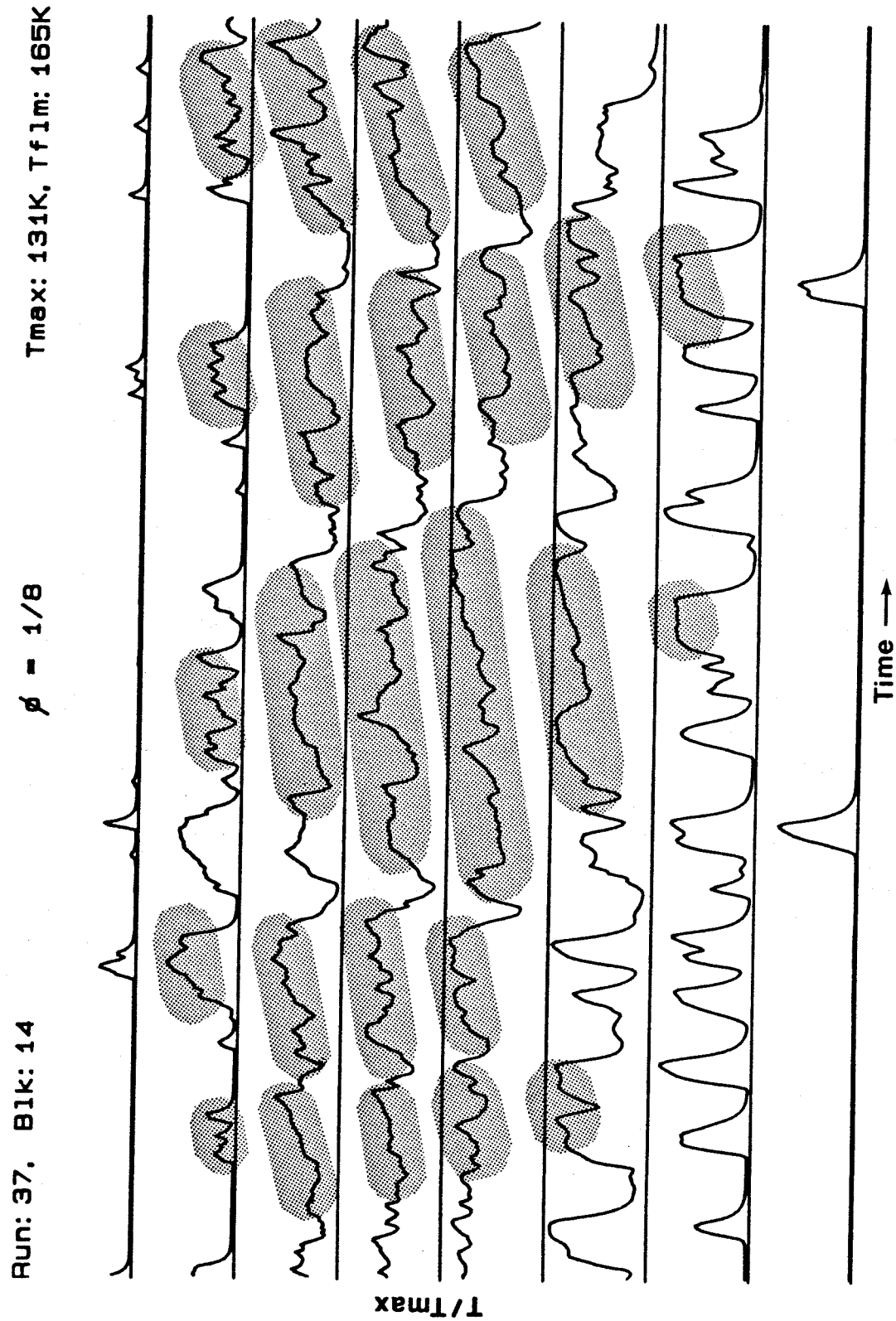

FIGURE 30b Temperature vs Time Trace, $\varphi = 1/8$

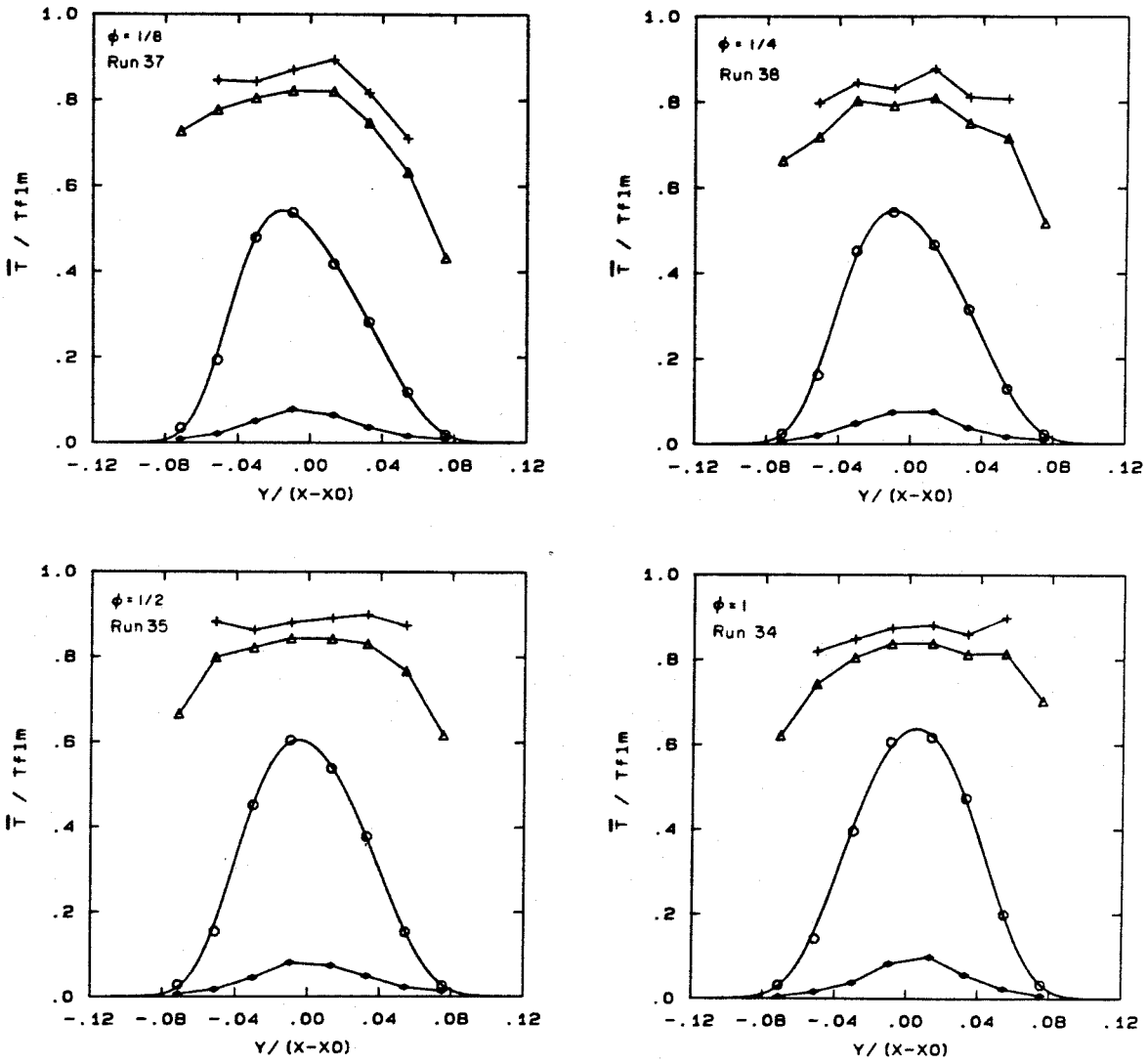

FIGURE 31a Compensated Highs, $\varphi \leq 1$

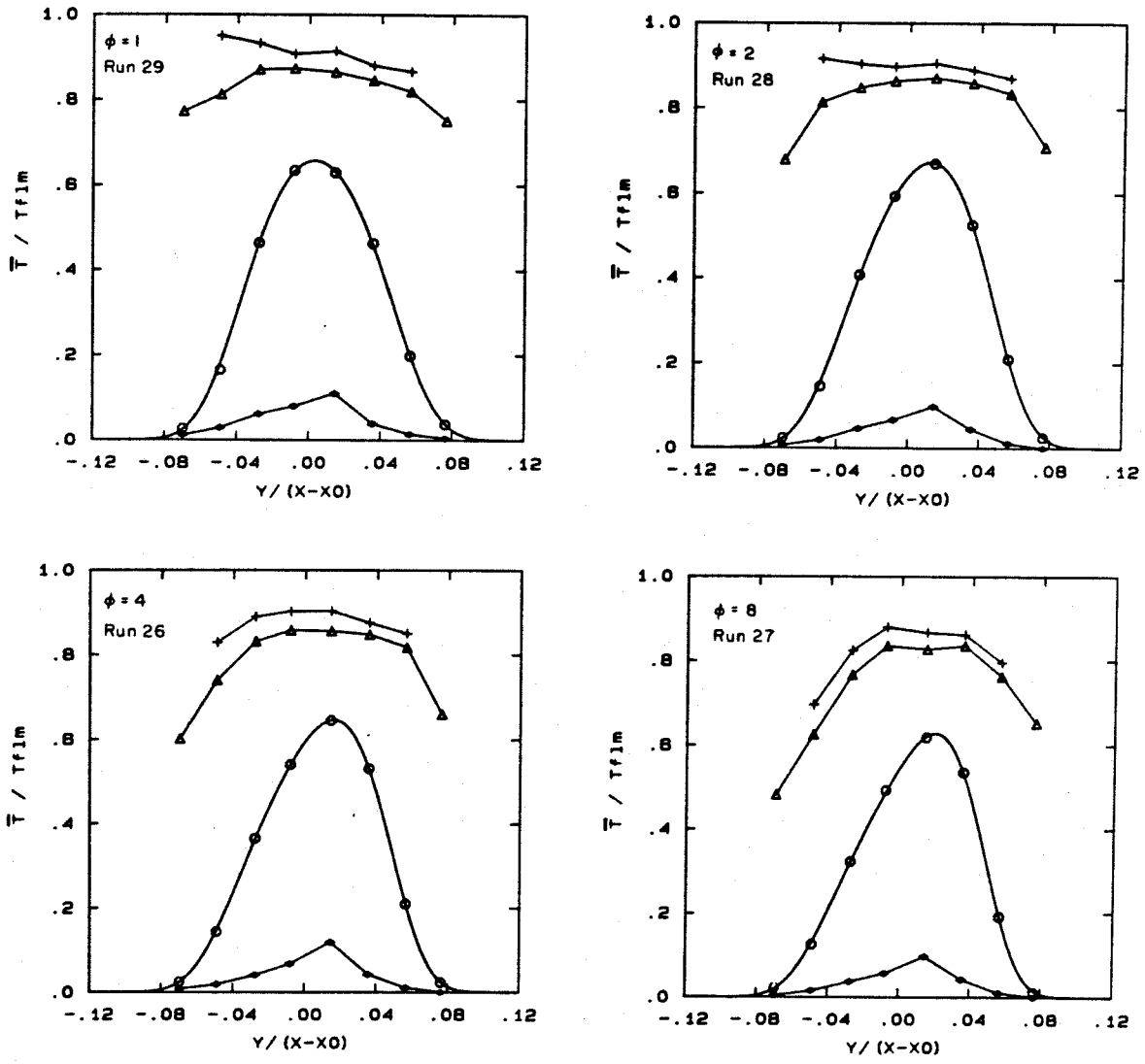

FIGURE 31b Compensated Highs, $\varphi \geq 1$

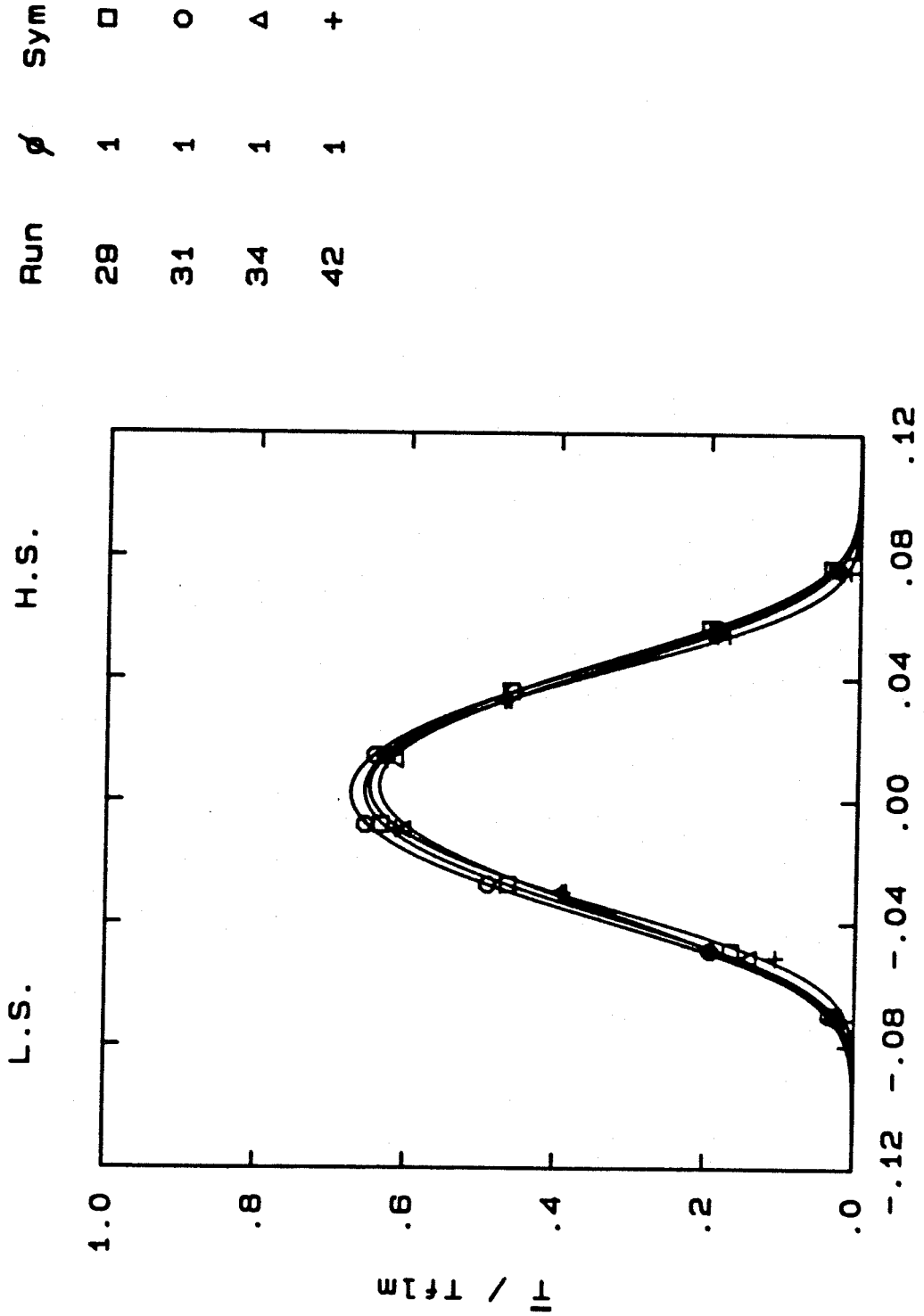

FIGURE 32 Effects of Chemistry, $\varphi = 1$

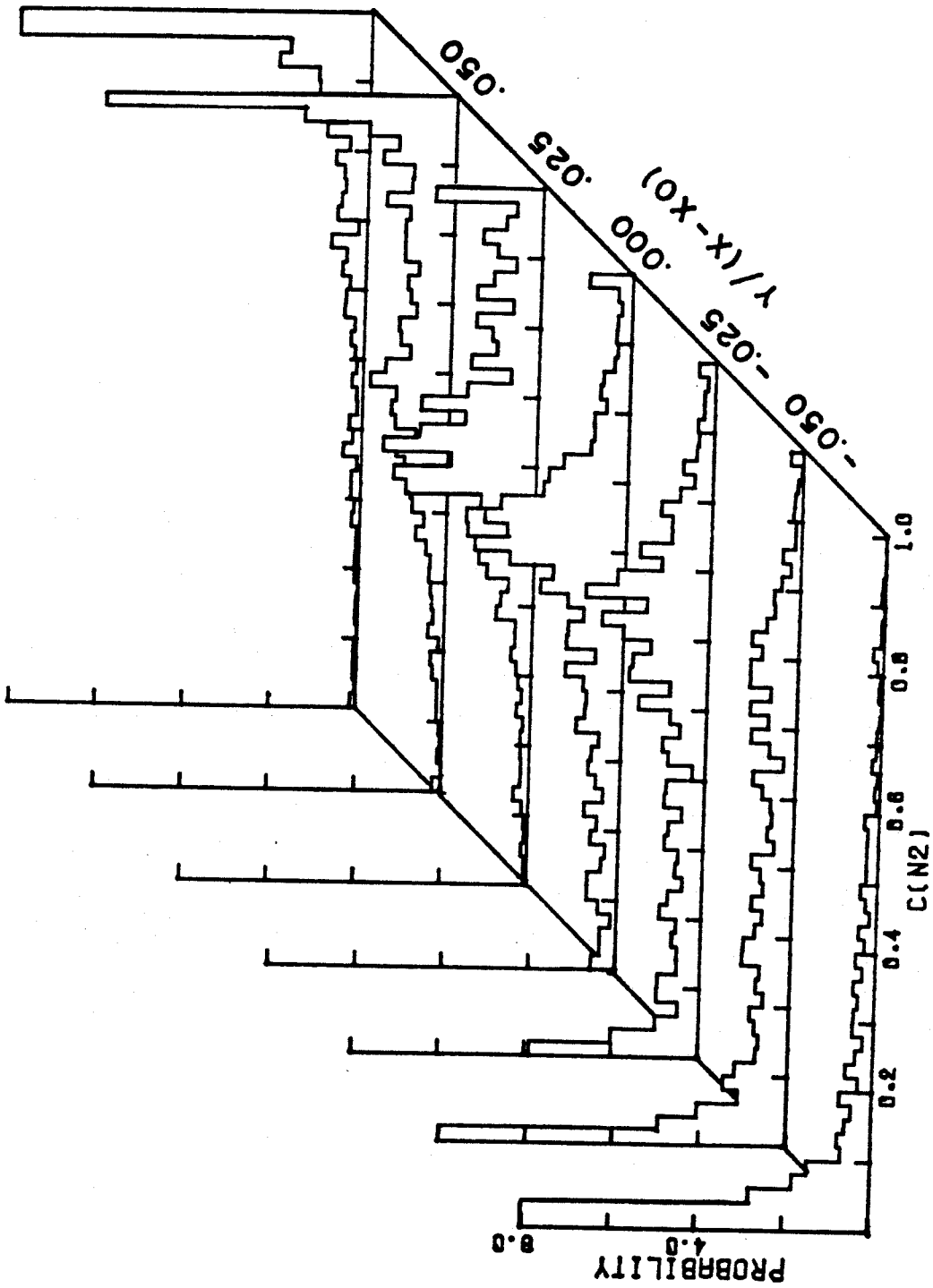

FIGURE 33 *PDF* of Turbulent Mixing Layer (Konrad)

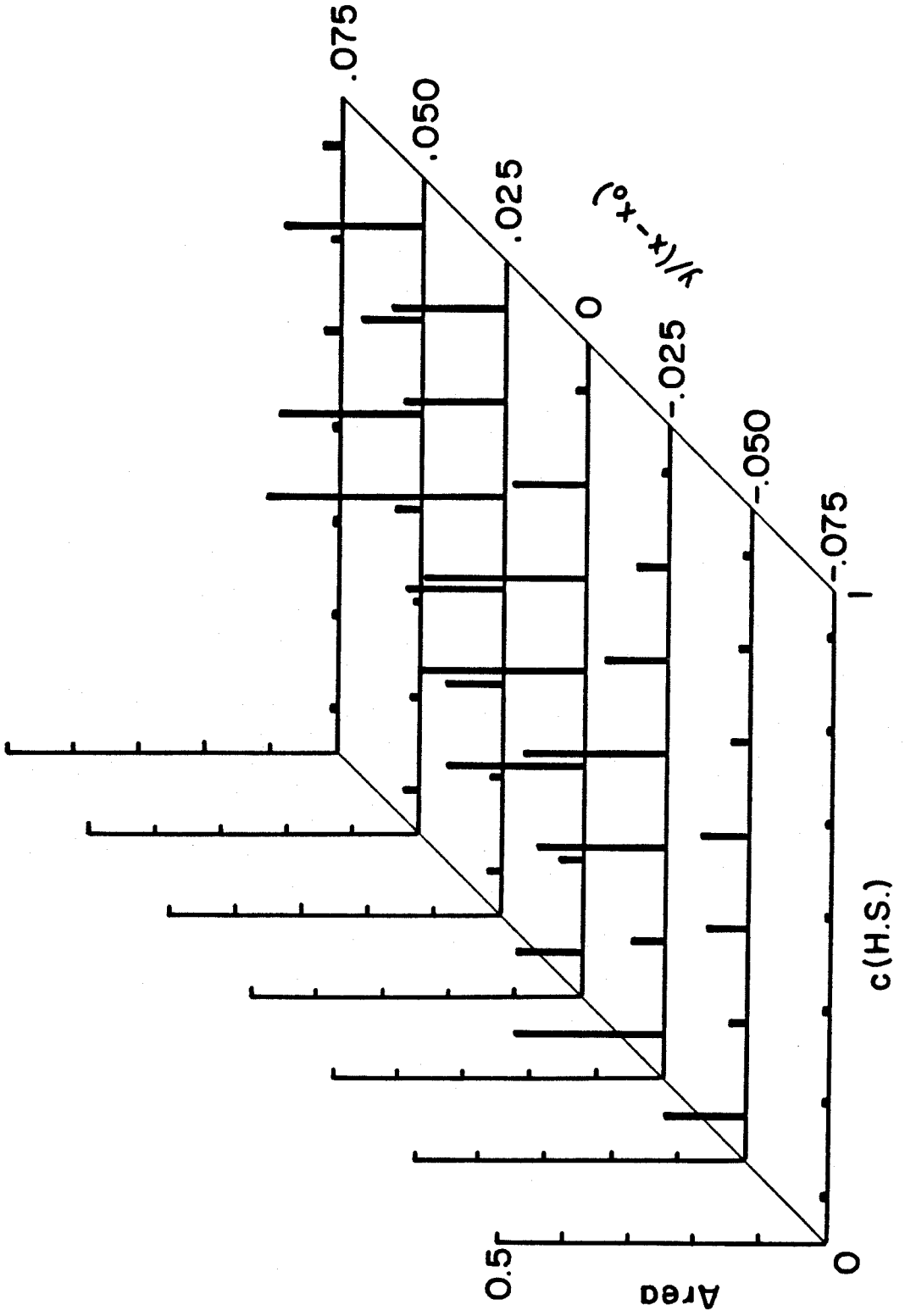

FIGURE 34 *PDF* by Direct Method

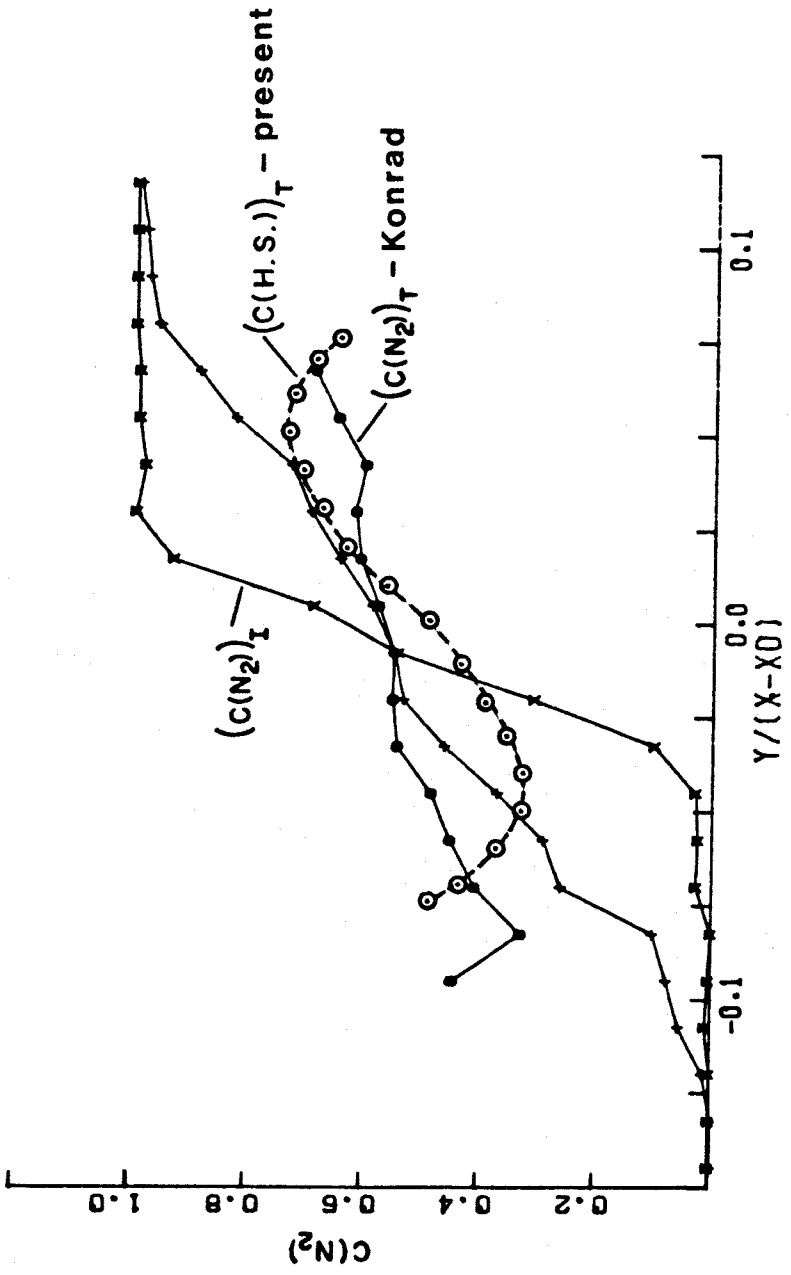

FIGURE 35 Comparison of Mean Mixed Concentration with Konrad

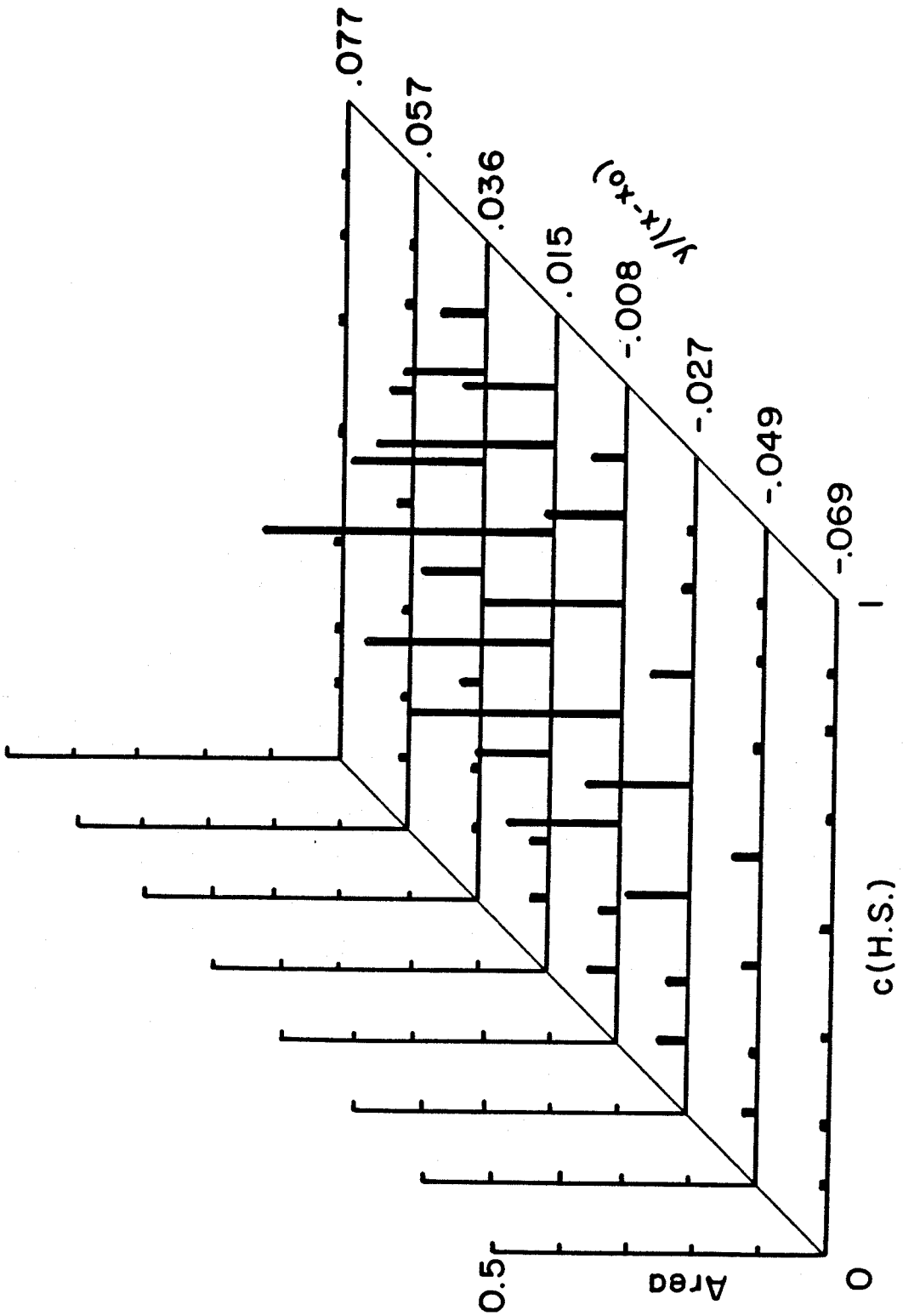

FIGURE 36 *PDF* by Franklin 3 Method

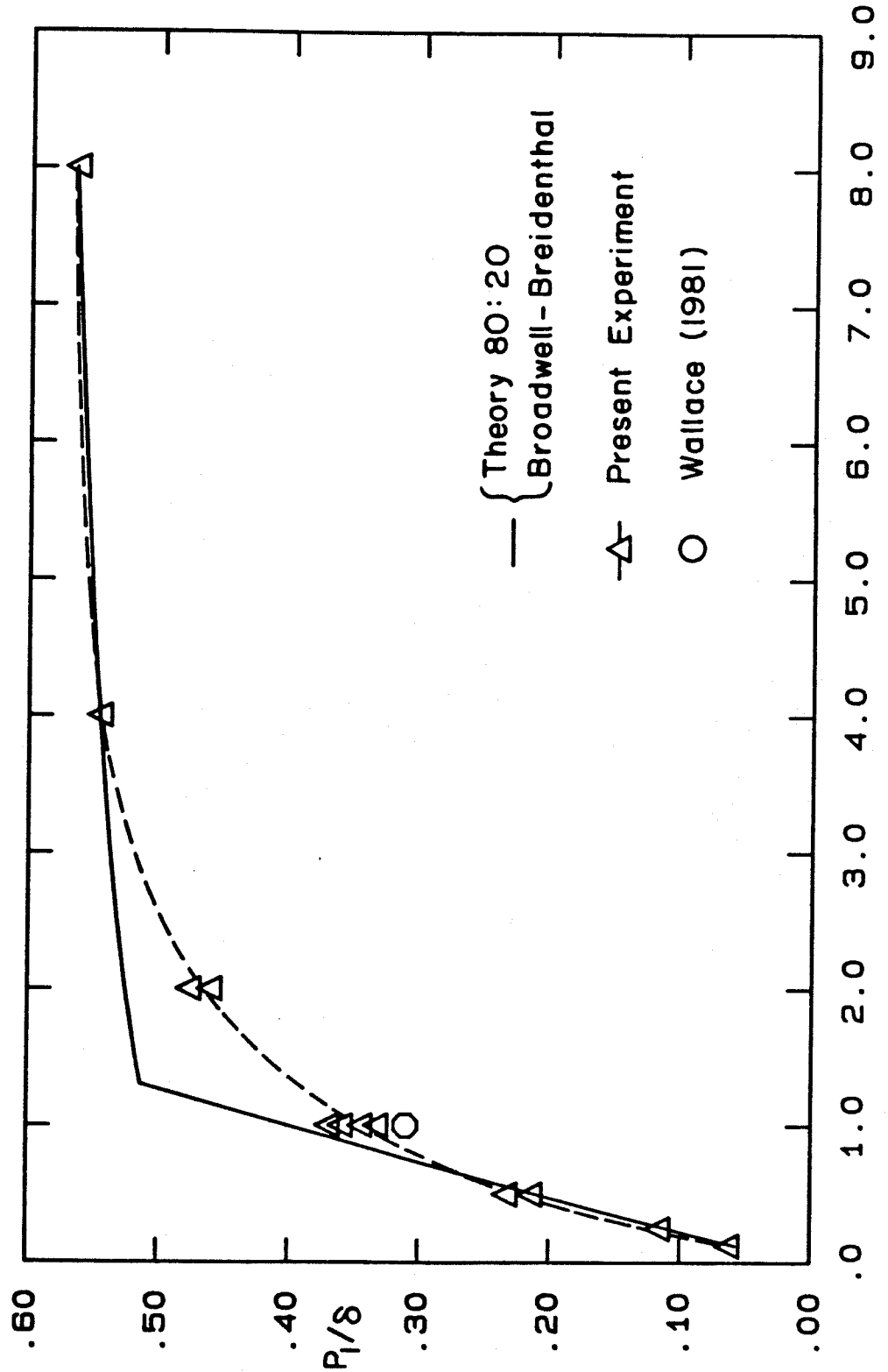

FIGURE 37 Dependence of Product Thickness on Equivalence Ratio

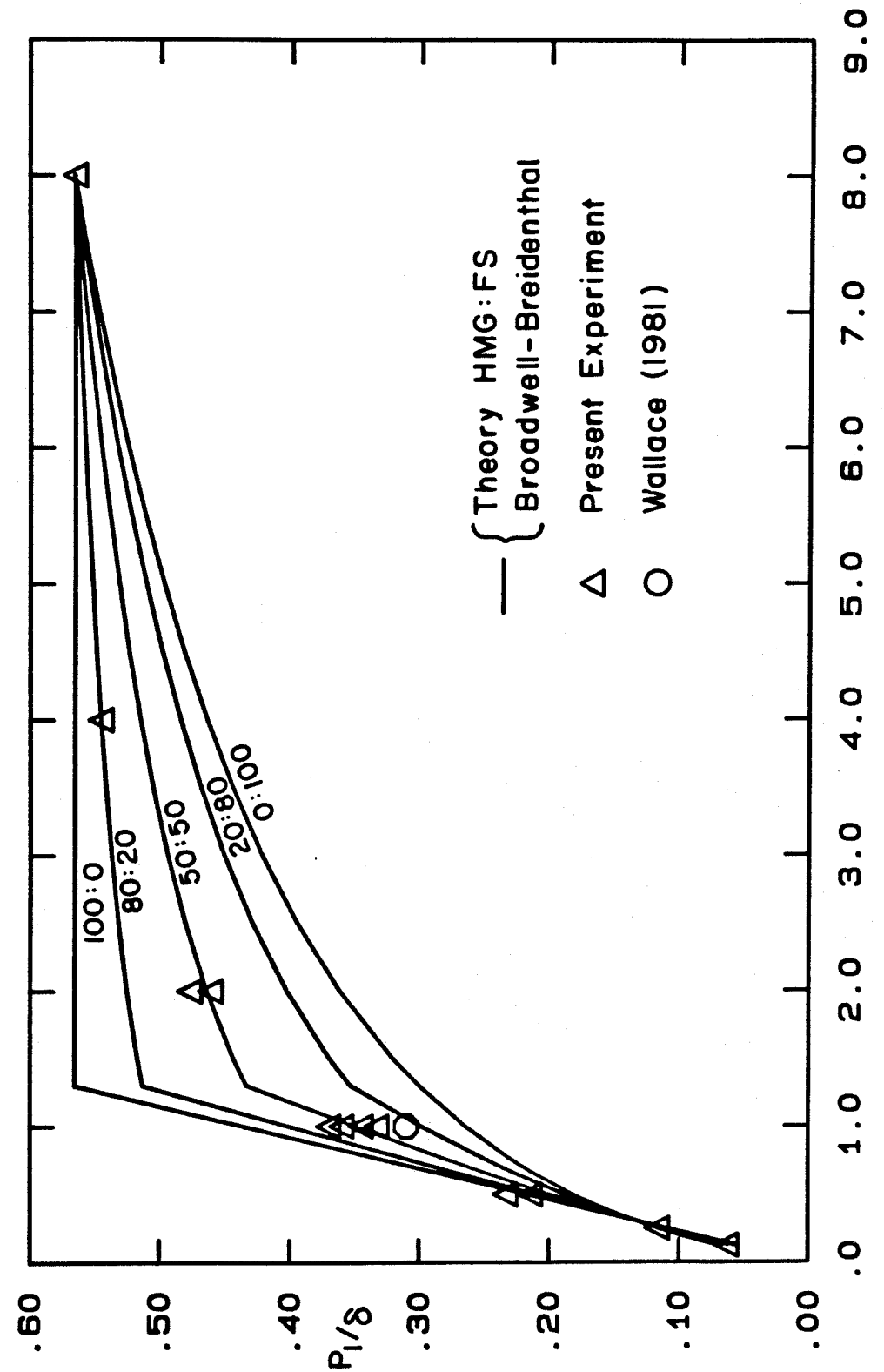

FIGURE 38 Dependence of Product Thickness on Homogeneous to Flame Sheet Ratio

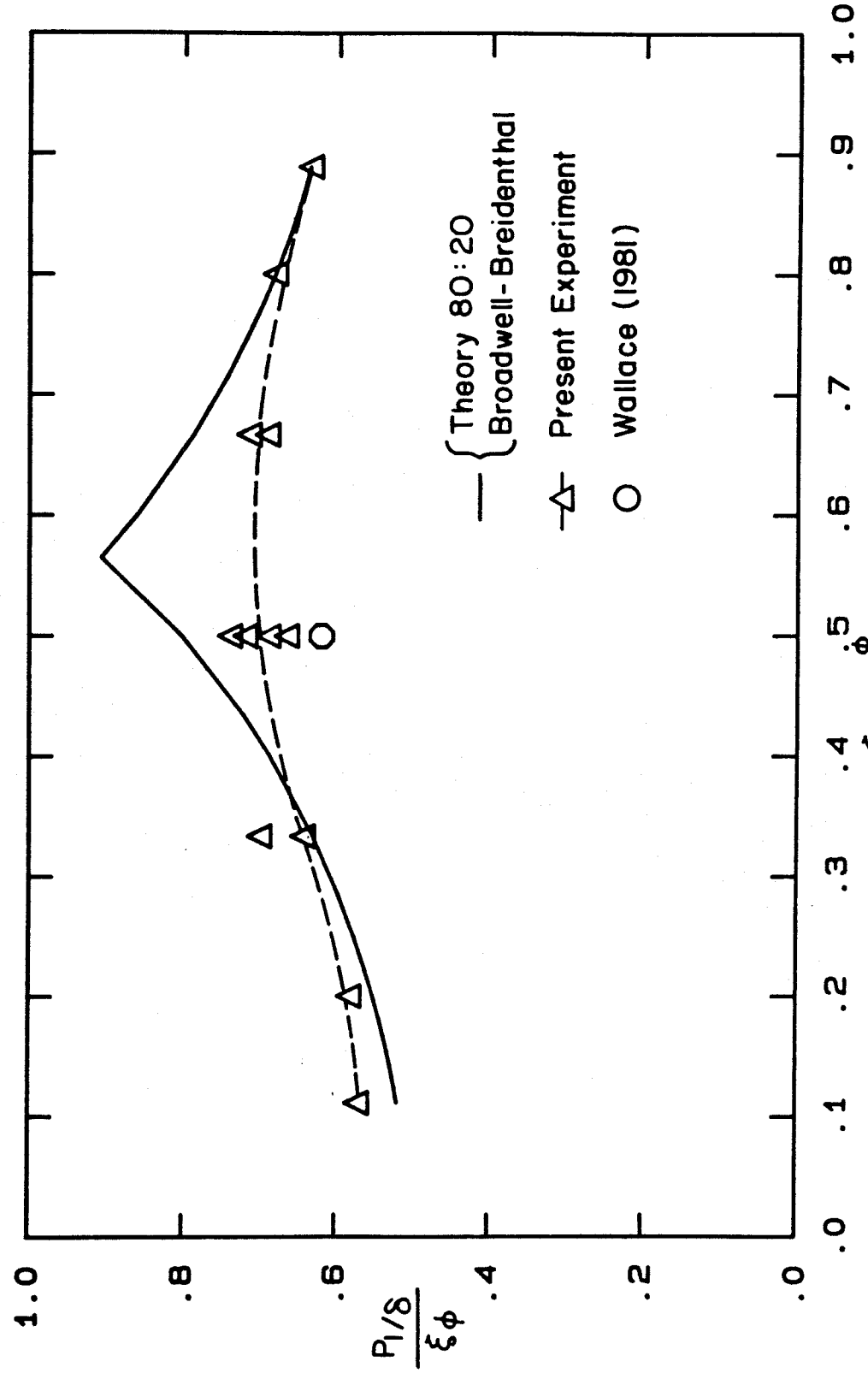

FIGURE 39 Product Thickness vs Normalized Equivalence Ratio

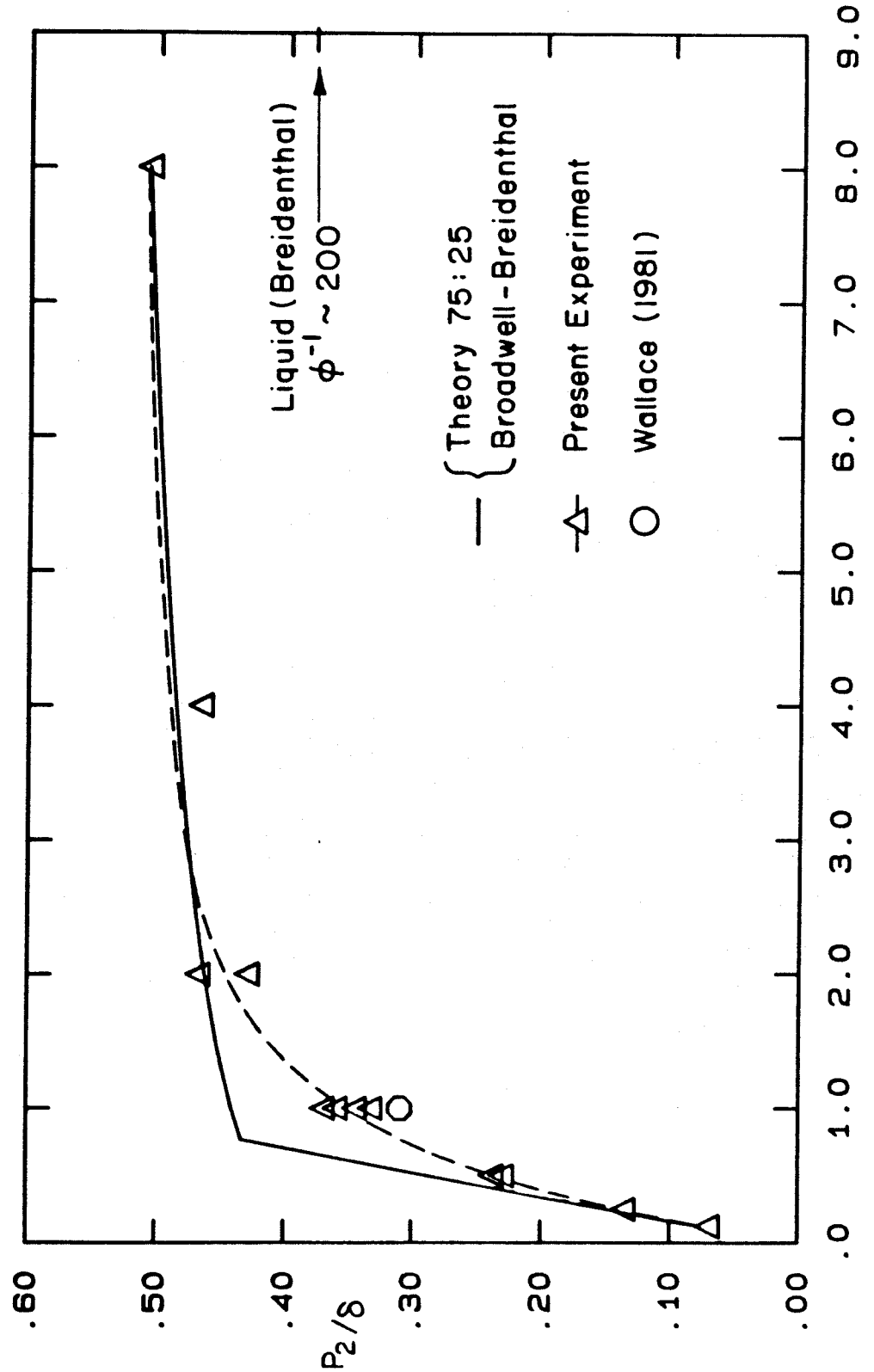

FIGURE 40 Dependence of Product Thickness on Inverse Equivalence Ratio

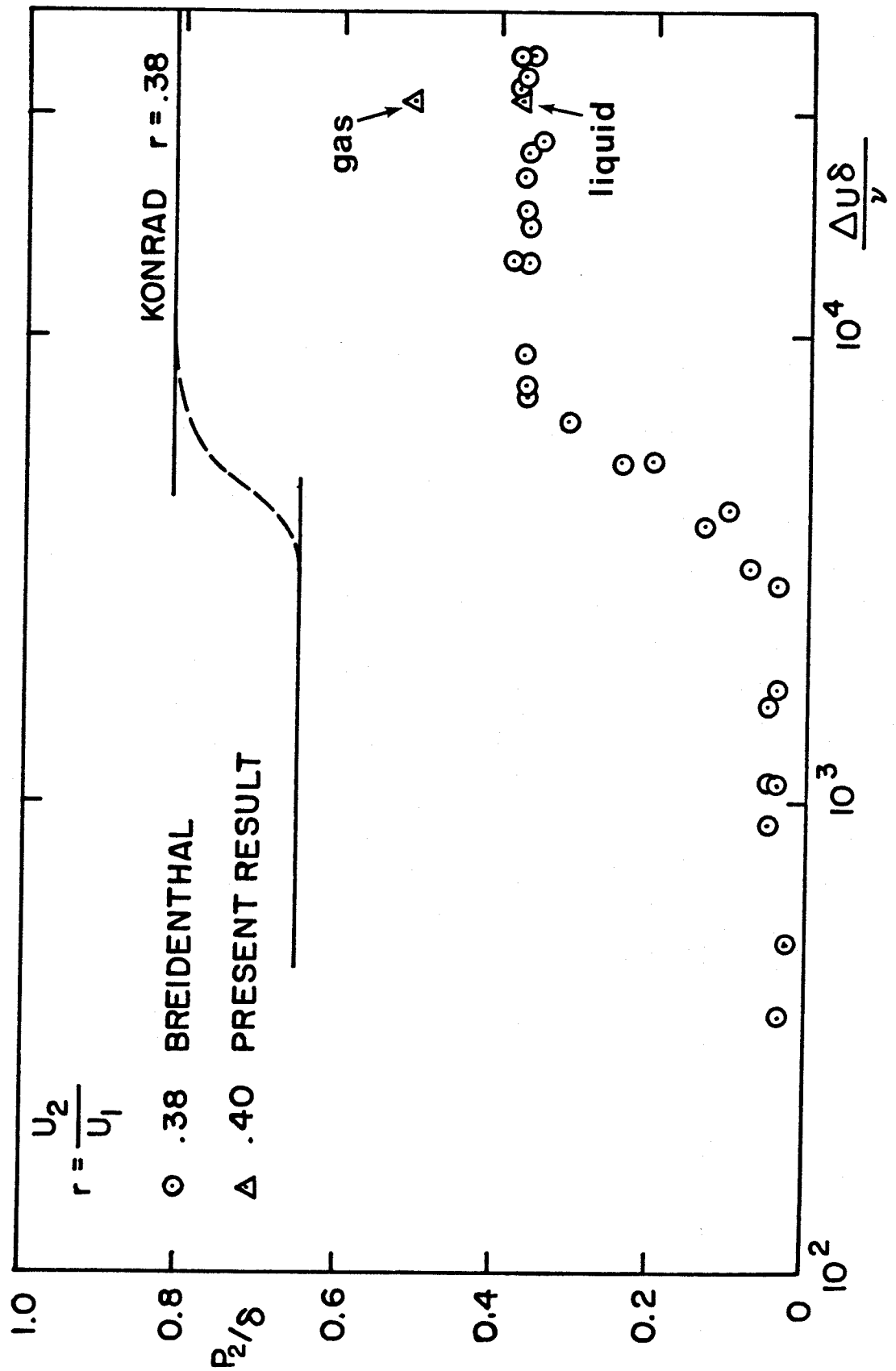

FIGURE 41 Comparison of Product Thickness with Breidenthal, Konrad

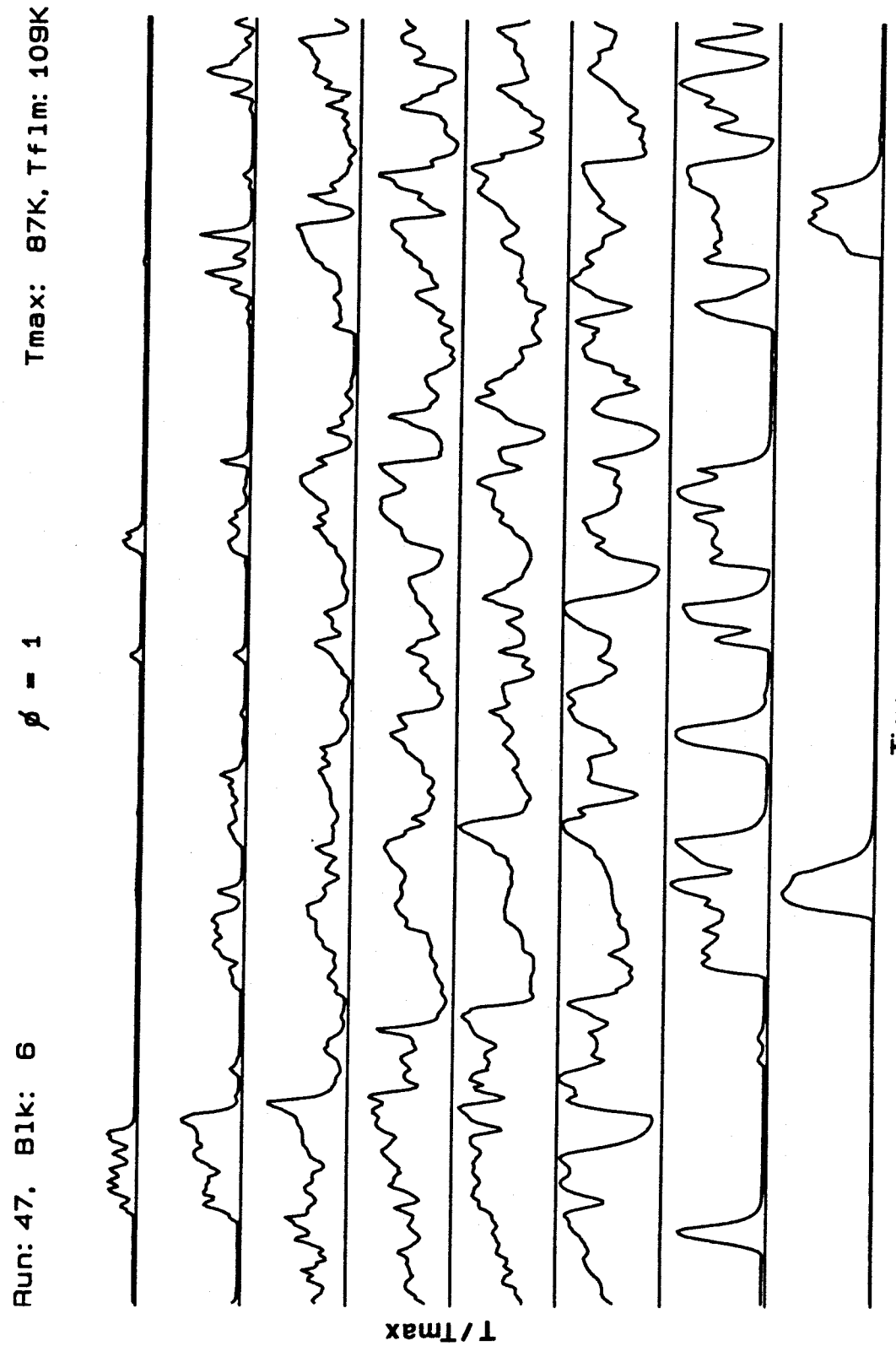

FIGURE 42a Temperature vs Time Trace, $\varphi = 1, r = 0.38, s = 7$, Run = 47.
Flow from right to left, high speed on top. Time axis = 51.2 msec.

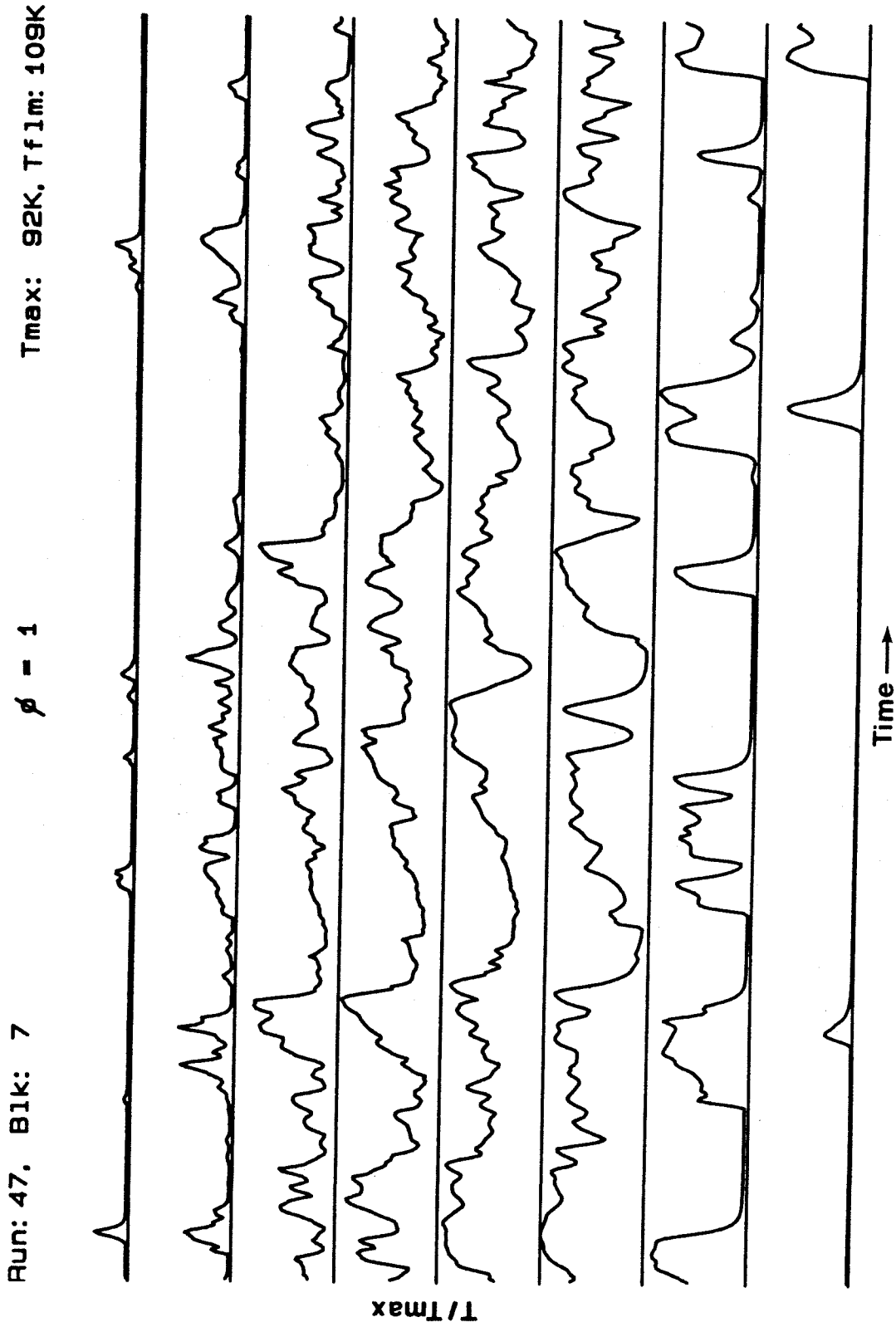

FIGURE 42b Temperature vs Time Trace, $\varphi = 1$, $r = 0.38$, $s = 7$, Run = 47.
Flow from right to left, high speed on top. Time axis = 51.2 msec.

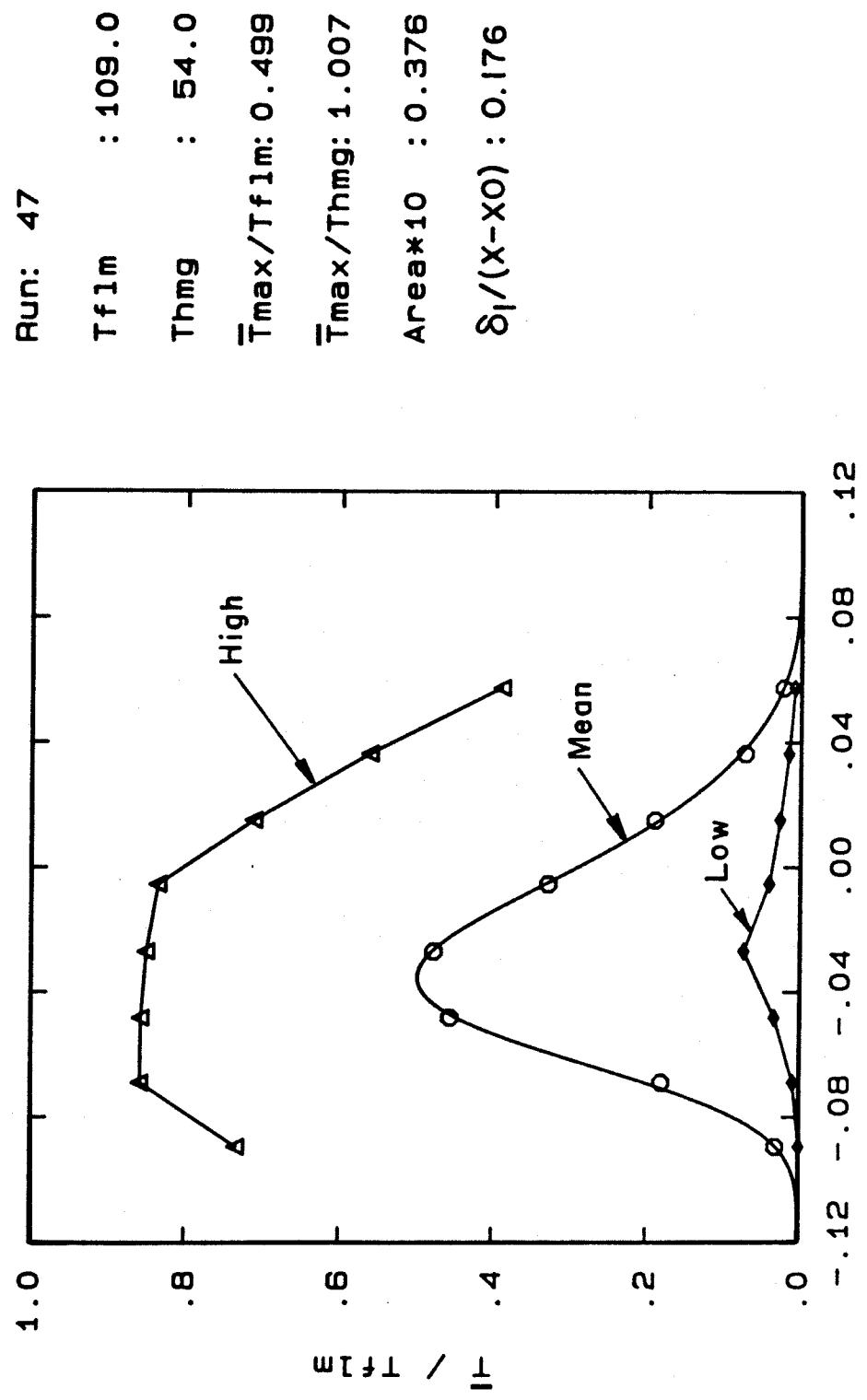

FIGURE 42c Mean Temperature Profile, $\varphi = 1, r = 0.38, s = 7$, Run = 47

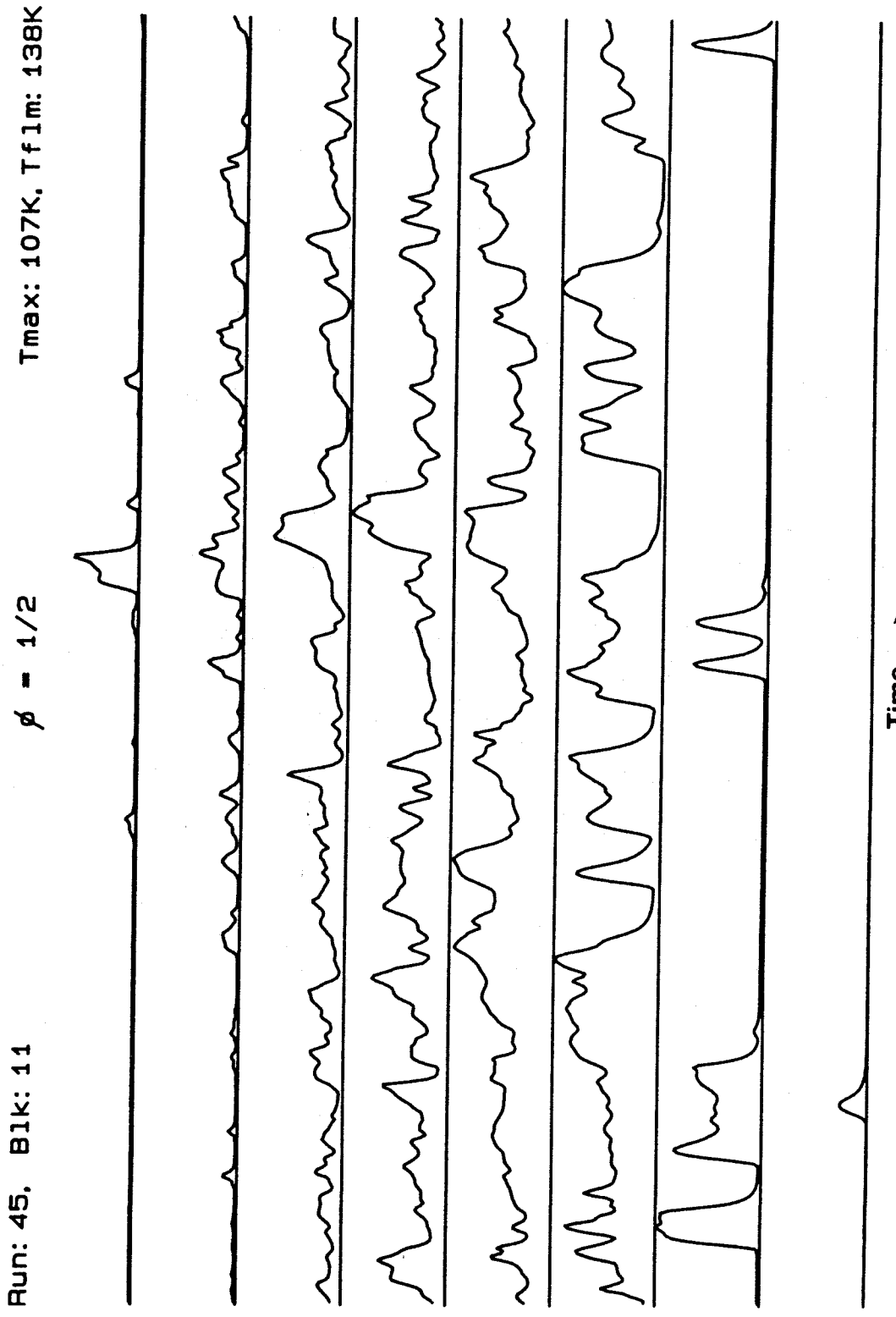

FIGURE 43a Temperature vs Time Trace, $\varphi = 1/2$, $r = 0.38$, $s = 7$, Run = 45.
Flow from right to left, high speed on top. Time axis = 51.2 msec.

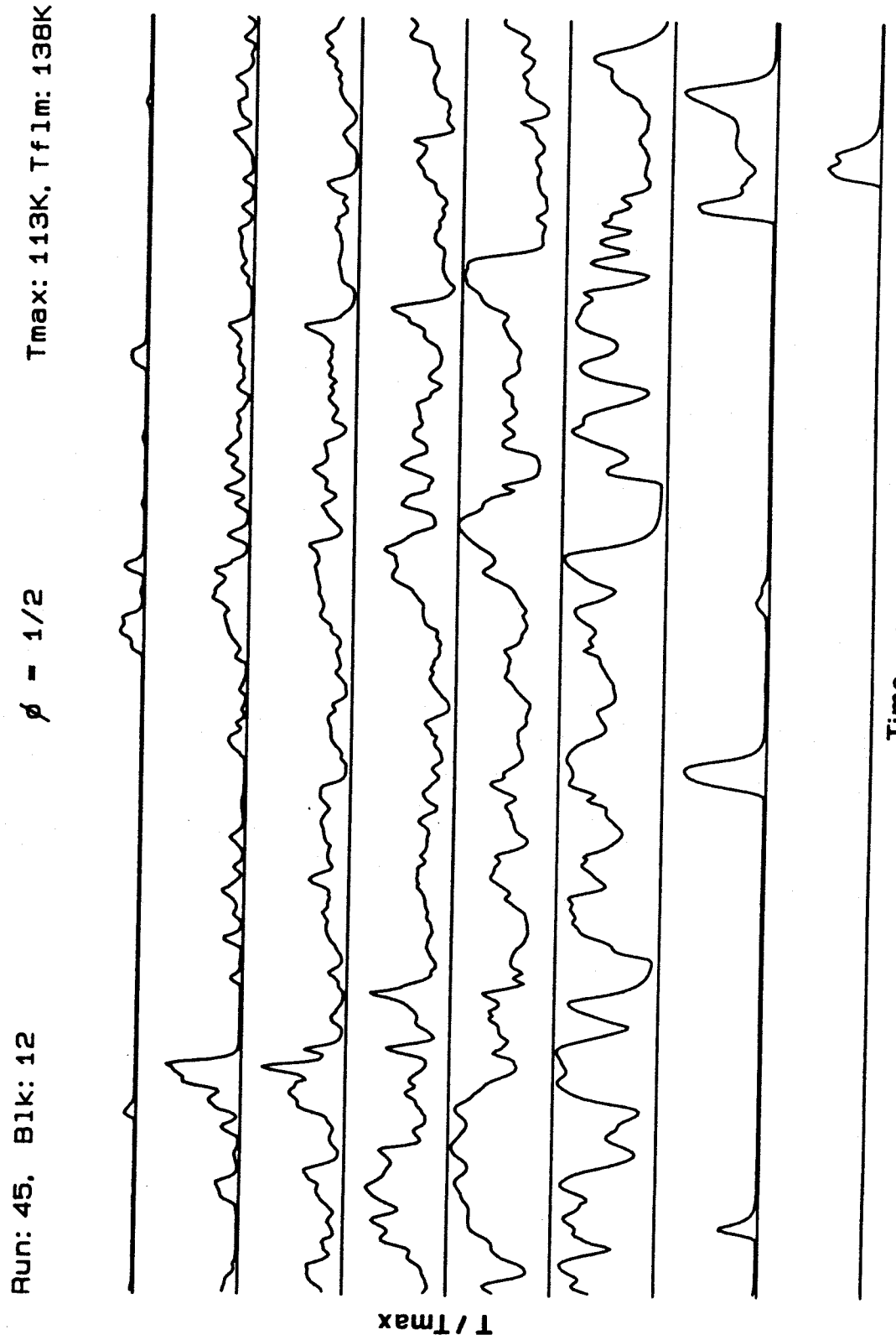

FIGURE 43b Temperature vs Time Trace, $\varphi = 1/2$, $r = 0.38$, $s = 7$, Run = 45.
Flow from right to left, high speed on top. Time axis = 51.2 msec.

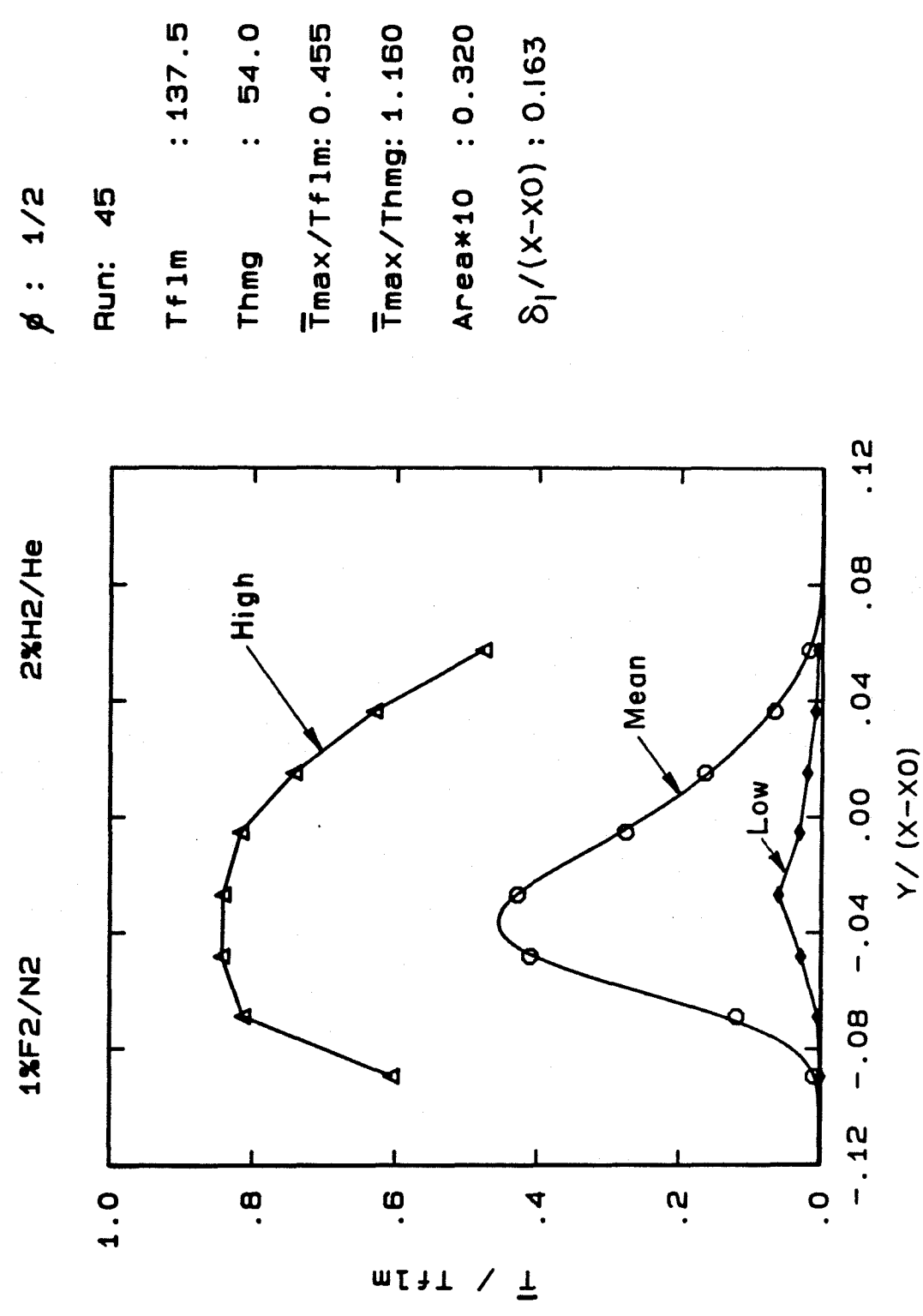

FIGURE 43c Mean Temperature Profile, $\varphi = 1/2$, $r = 0.38$, $s = 7$, Run = 45

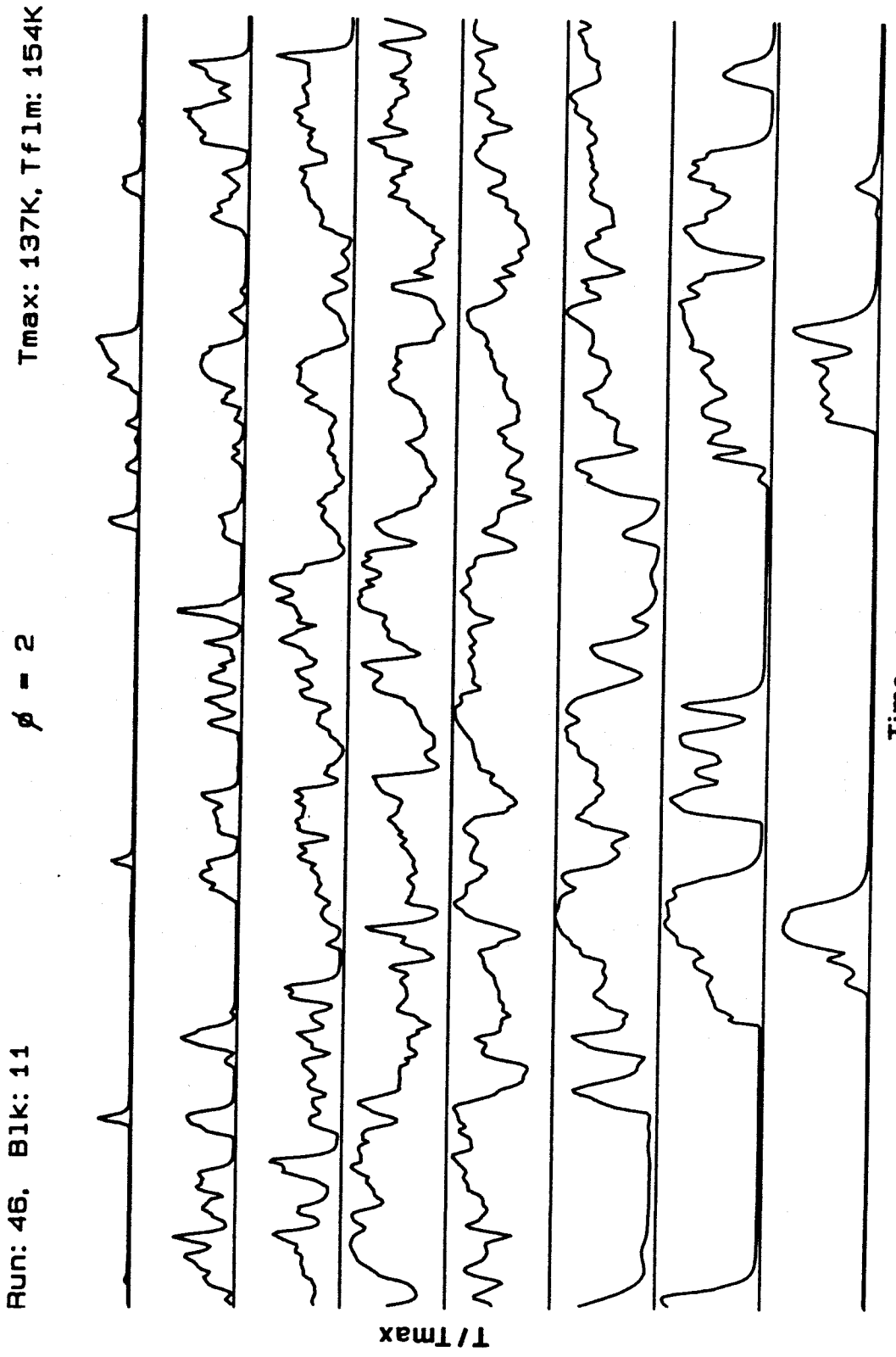

FIGURE 44a Temperature vs Time Trace, $\varphi = 2$, $r = 0.38$, $s = 7$, Run = 46.
Flow from right to left, high speed on top. Time axis = 51.2 msec.

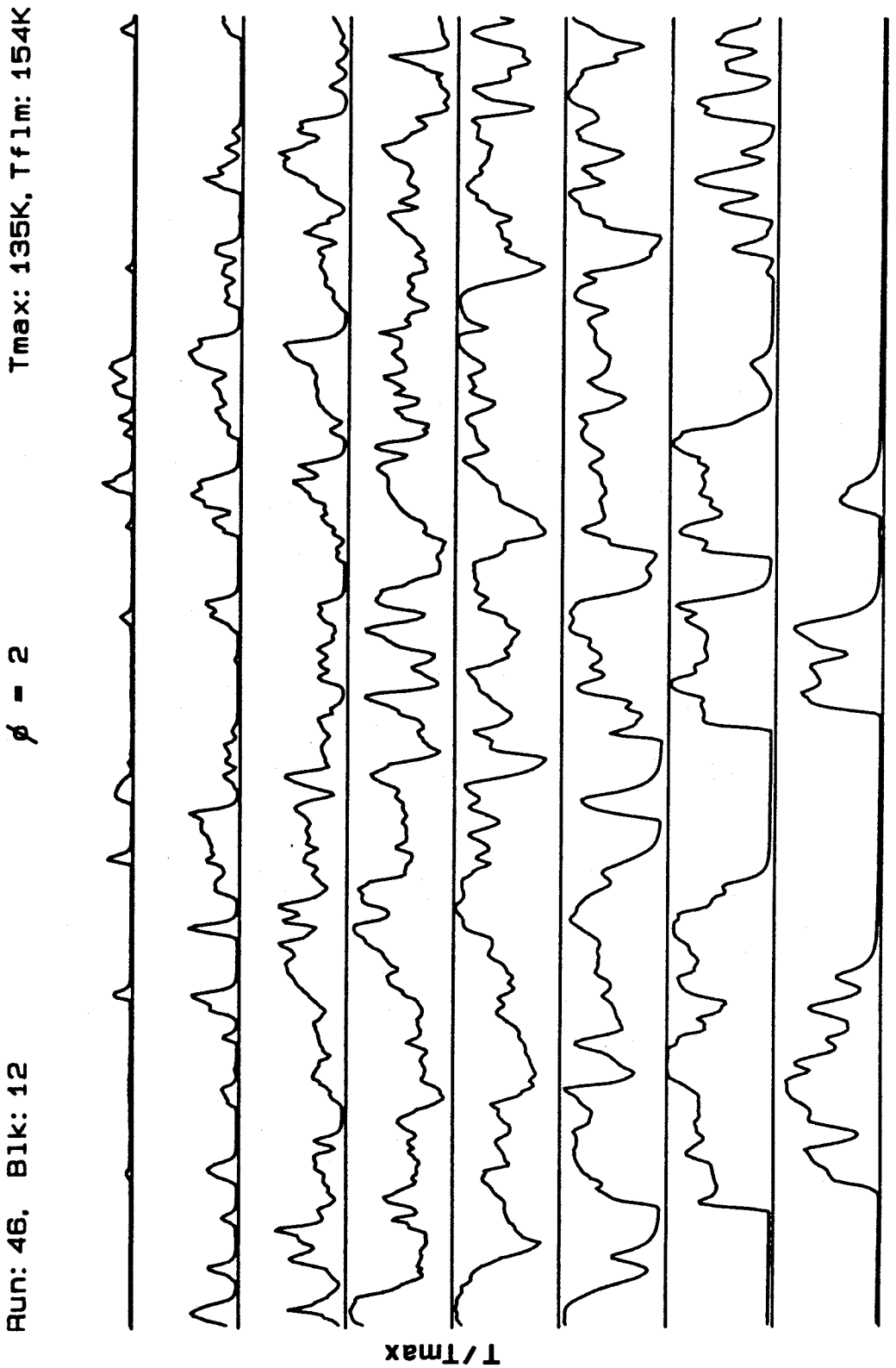

FIGURE 44b Temperature vs Time Trace, $\varphi = 2$, $r = 0.38$, $s = 7$, Run = 46.
Flow from right to left, high speed on top. Time axis = 51.2 msec.

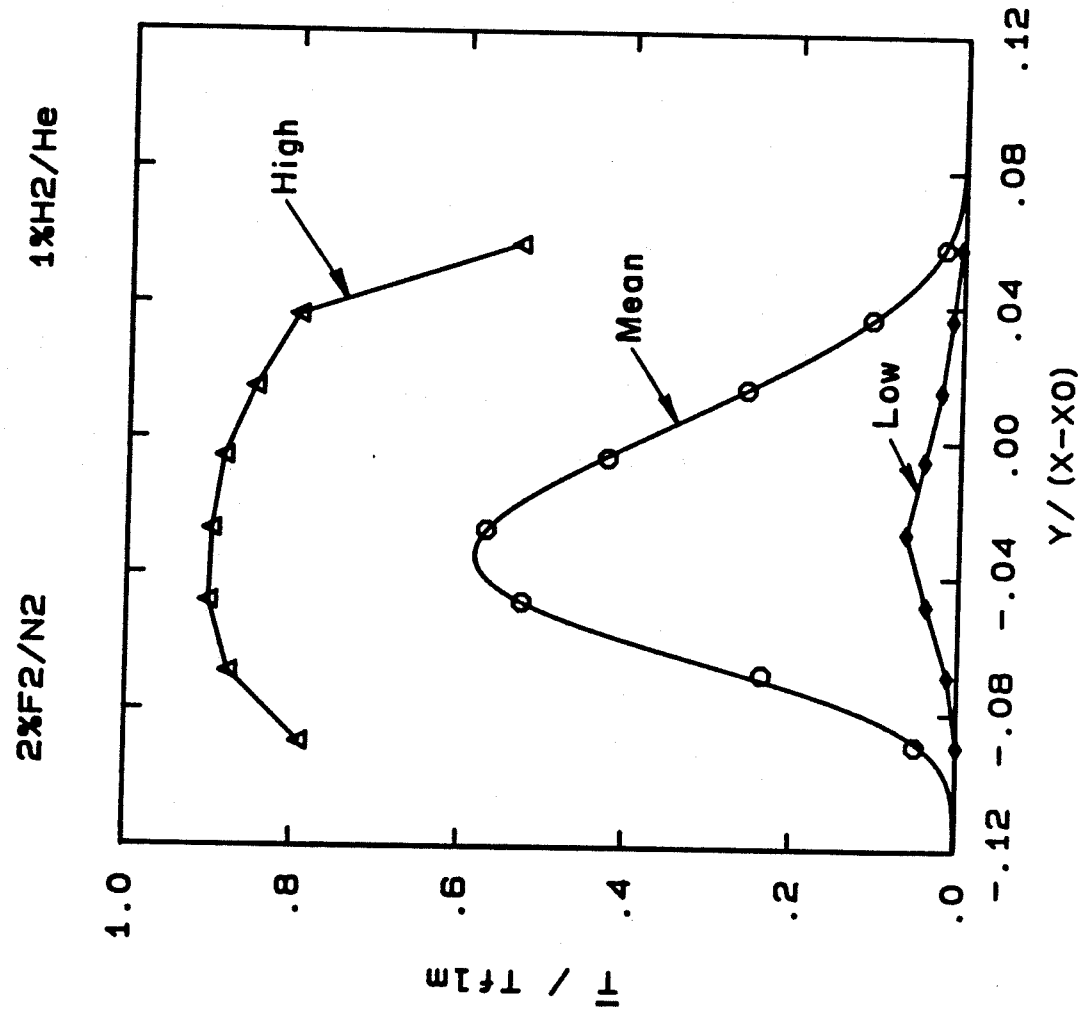

FIGURE 44c Mean Temperature Profile, $\varphi = 2$, $r = 0.38$, $s = 7$, Run = 46

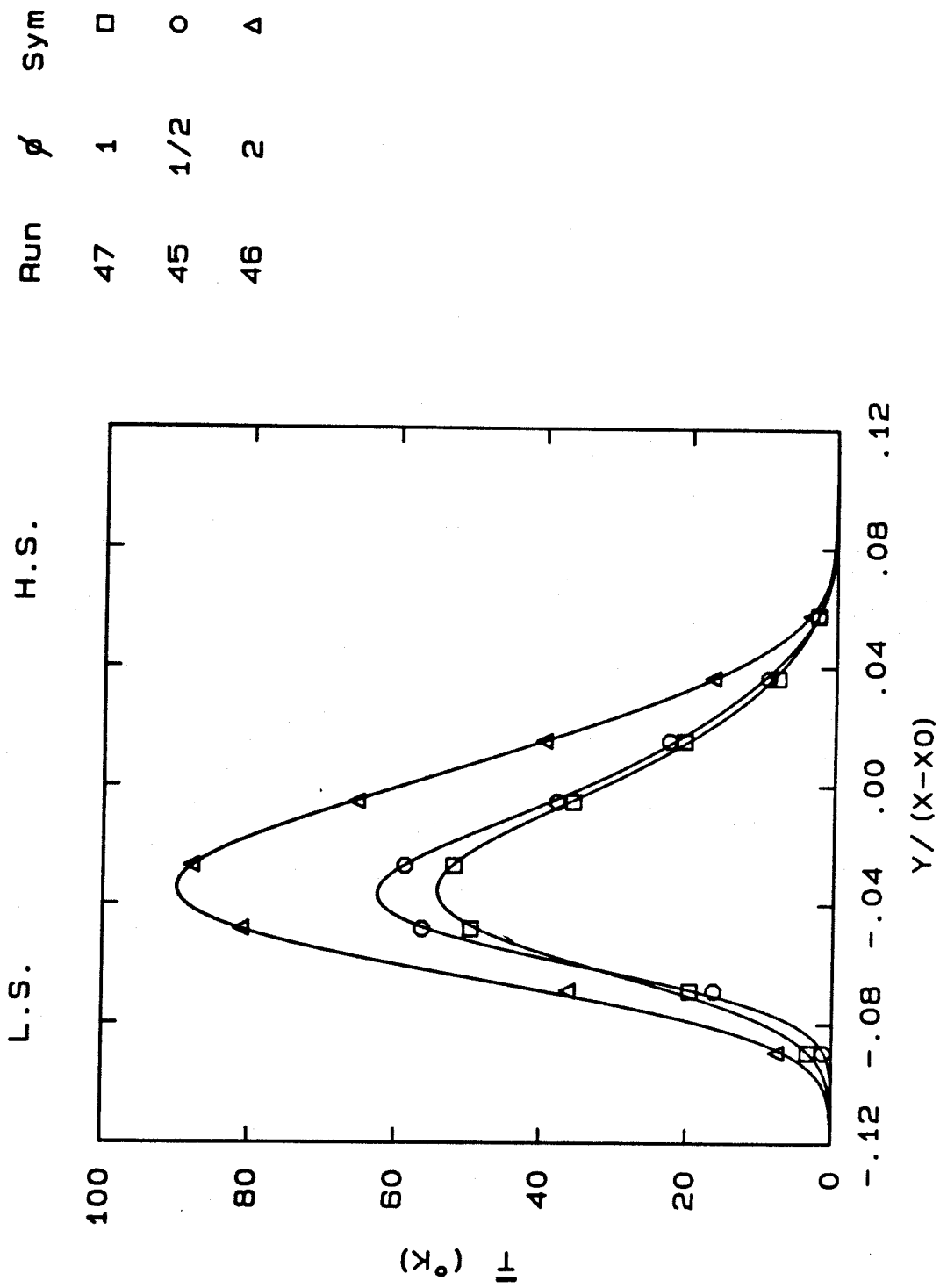

FIGURE 45 Mean Temperature Profiles, $r = 0.38$, $s = 7$, $\varphi = 1/2, 1, 2$

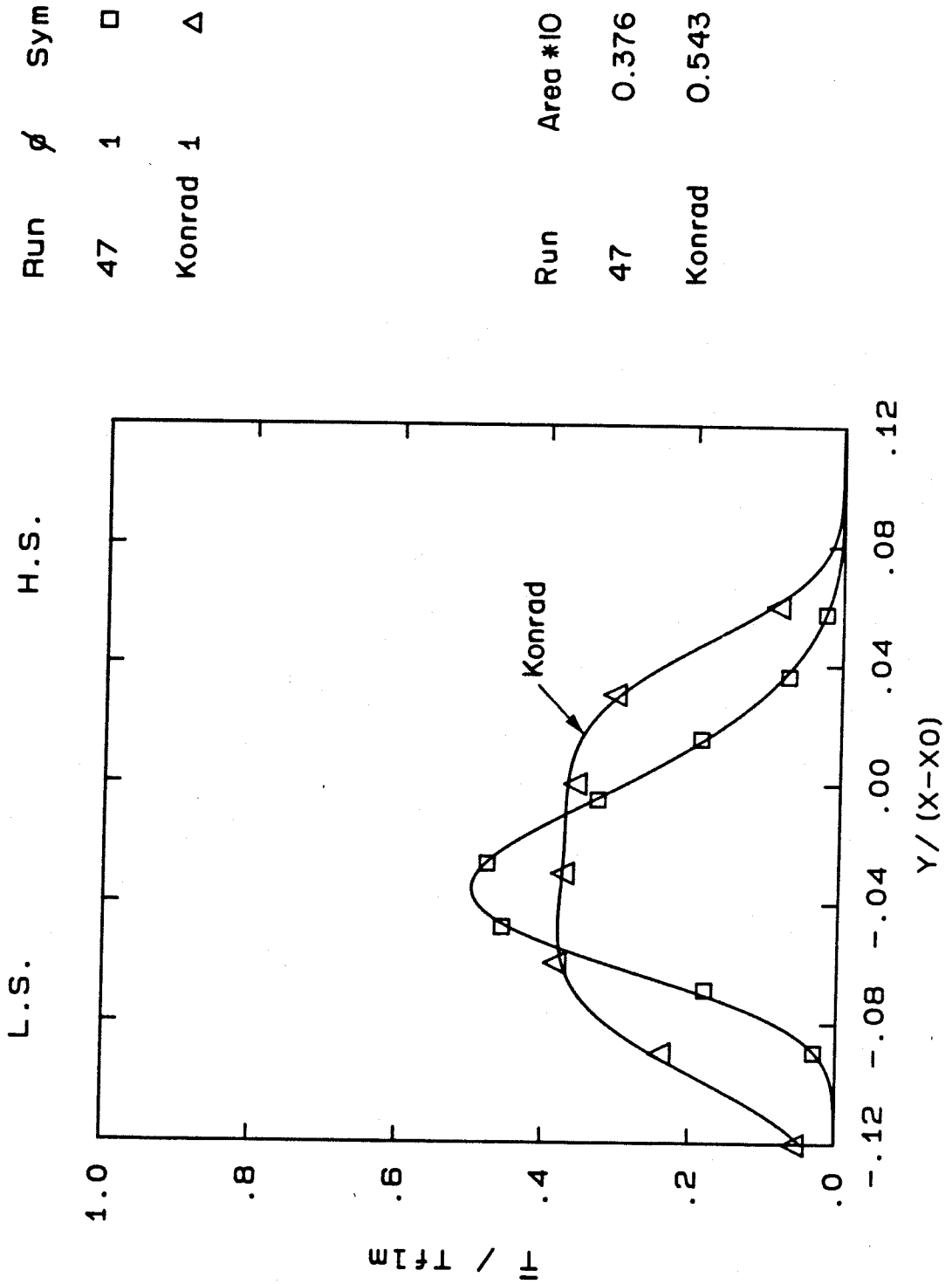

FIGURE 46 Comparison with Konrad, $r = 0.38$, $s = 7$, $\varphi = 1$